EXPLORING TRANSIENT NEURAL EVENTS IN HEALTHY POPULATIONS USING NON-INVASIVE NEUROIMAGING

by

Brendan Brady

Submitted in partial fulfillment of the requirements
for the degree of Doctor of Philosophy

at

Dalhousie University
Halifax, Nova Scotia
August 2022

Table of Contents

List of Tables

List of Figures

Abstract

Non-invasive neurophysiological recordings, like those measured by magneto/electro-encephalography (M/EEG), provide insight into the behaviour of neural networks and how these networks change with factors such as task performance, disease state, and age. Recently, there has been a trend in describing neurophysiological recordings as a series of transient bursts of neural activity rather than averaged sustained oscillations as burst characteristics may be more directly correlated with the neurological generators of brain activity. This thesis presents three projects focused on exploring sensorimotor transient bursts in healthy populations using non-invasive neuroimaging.

Project 1 investigates age-related changes in beta burst characteristics using MEG data acquired at the Cambridge Centre for Ageing and Neuroscience (n=596, ages 18-88). The objectives of project 1 are (1) to detect and characterize transient beta bursts over the ipsilateral and contralateral primary sensorimotor cortices during a unilateral motor task performance and during wakeful resting, and (2) to identify age-related changes in beta burst characteristics, in the context of earlier reports of age-related changes in beta suppression and the post-movement beta rebound. We found that the beta burst rate is the main influencer of beta rhythm power and the predominant factor related to age-related changes in the amplitude of the induced beta rhythm responses associated with a button press task.

Project 2 presents a novel transient burst detection algorithm called the periodic/aperiodic parametrization of transient oscillations (PAPTO). The objectives of project 2 are (1) to motivate and validate the PAPTO algorithm, and (2) to use PAPTO to disambiguate adult lifespan changes in the aperiodic activity power spectrum and transient event characteristics. Project 2 analyzes the same MEG data as analyzed in Project 1. We show that PAPTO is more sensitive to neocortical transient beta rhythms compared to more conventional transient event detection algorithms and captures more variance in the resting-state occurrence rate of beta events across participants.

Project 3 explores the hemodynamic changes coupled to the occurrence of transient events using simultaneous EEG- functional near-infrared spectroscopy (fNIRS) recordings from healthy participants (n=26). The objectives of project 3 are (1) to extract the burst-evoked hemodynamic response function (HRF) for transient mu, beta, and gamma events using resting state recordings, and (2) to evaluate the contribution of neurovascular changes evoked by transient events to the total measured hemodynamic response over a unilateral finger-tapping motor task. We found that transient beta events evoke a significant ($p<0.05$) decrease in oxy-hemoglobin concentration and increase in deoxy-hemoglobin concentration.

This thesis is as an important step in characterizing transient bursts in neurophysiological signals in the temporal domain, towards a better understanding of sensorimotor activity in the healthy human brain.

Acknowledgements

First and foremost, I would like to thank my supervisor, Dr. Tim Bardouille, for his continued patience, guidance, and mentorship. Tim exemplifies the true meaning of a scientist.

Thank you to my committee members, Dr. Heather Neyedli and Dr. Steven Beyea, for their valuable insights and inputs, and for their mentorship and words of encouragement.

Thank you to the students who have passed through the BioSignals Lab over the years, many of whom have been vital to completing this research.

This thesis could not have been completed without the financial support from the Natural Sciences and Engineering Research Council of Canada, the Nova Scotia Graduate Scholarship, and the Walter C. Sumner Memorial Fellowship.

Finally, thank you to my friends and my family. Your love and support helped me in ways I cannot put into words.

Chapter 1

Introduction

1.1 Sensorimotor Beta (15 - 30 Hz) Activity

The coupling/integration of sensory input (i.e., vision, audition, tactile stimulation, olfaction, and gustation) to a related voluntary motor response is achieved via sensorimotor processing. Sensorimotor processing occurs in/between several brain structures, including the primary sensorimotor cortices, basal ganglia, and the thalamus. Electrophysiological signatures in these structures, as measured via magnetoencephalography (MEG), electroencephalography (EEG), electrocorticography (ECoG), and local field potential (LFP), are naturally rhythmic/oscillatory. The association between oscillations in the 15-30 Hz frequency range (the so-called *beta band*) and sensorimotor processing is well-established (Pfurtscheller and Lopes da Silva, 1999). Beta rhythms are diminished below baseline levels prior to and during movement, known as beta event-related desynchronization (ERD). Beta ERD happens even without actual movement, as in the case of motor imagery (Miller et al., 2010). Beta rhythms are enhanced above baseline levels after movement stops, an effect known as post-movement beta rebound (PMBR). Beta rhythms have been shown to emerge from the sensorimotor cortex (Murthy and Fetz, 1992) and the basal ganglia (Brown et al., 2001), and beta ERD and PMBR have been shown in both structures (Engel and Fries, 2010).

The association of beta rhythms with sensorimotor processing is well established, yet the physiological relevance (i.e., functional role) of beta rhythms is not well understood. After the discovery of beta ERD and PMBR in relation to movement, early work suggested beta oscillations are simply representative of an ‘idling’ signal in sensorimotor processing, in that beta rhythms become evident when the system is in a state of “nothing to do” (Pfurtscheller et al., 1996). In the following 10-15 years, evidence emerged suggesting a more specific, functional, role of beta oscillations (for review, see Engel and Fries (2010)). Engel and Fries (2010) proposed what is currently the most well-accepted hypothesis for the role of beta rhythms; beta oscillations are representative of an *active* process that intends to maintain the current sensorimotor/cognitive state and inhibit the sensorimotor processing of incoming sensory information (i.e., maintenance of the "status-quo"), herein referred to as the *status-quo* hypothesis. The status-quo hypothesis suggests that beta ERD and PMBR are driven by endogenous cognitive processes, where ERD is necessary for releasing inhibition and allowing the initiation/execution of a motor plan and the PMBR represents a state of motor cortical inhibition which preserves the existing state from internal and external sources of noise (Barone and Rossiter, 2021). In the following sections, a selection of studies that contribute to the understanding of the functional role of beta oscillations are highlighted. The conceptualization presented in sections 1.1.1 through 1.1.4 is largely based off that from a review paper (Barone and Rossiter, 2021) focused on new evidence for understanding the role of sensorimotor beta oscillations.

1.1.1 Beta Rhythm Changes with Healthy Aging

A detailed review of age-related trends in beta ERD and PMBR can be found in section 2.2

Beta rhythm characteristics change over the lifespan in a reasonably stereotypical manner. Here we consider healthy aging in two regimes, first the developmental regime from children to adult, and second the adulthood regime from younger to older adulthood. Gaetz et al. (2010) examined beta ERD and PMBR in children at different stages of typical development (4-6 years, n=10, and 11-13 years, n=10) and in adults (n=10), all performing the identical motor task. They found a developmental trend of increasing beta ERD and PMBR with age and that the PMBR was particularly diminished in the younger age group. The authors suggest that this diminished PMBR may reflect reduced inhibition generated by the inhibitory neurotransmiter γ-Aminobutyric acid (GABA), which could in turn facilitate neuronal plasticity and promote motor learning in children.

Motor performance is known to decline with healthy ageing over the adult lifespan. Several reports find that ageing is also accompanied by increases in resting state beta power (Rossiter et al., 2014b; Heinrichs-Graham and Wilson, 2016), an enhancement of movement-induced beta ERD, and a reduction in PMBR (Bardouille and Bailey, 2019). Interestingly, older adults show smaller changes in PMBR compared to younger adults in motor learning paradigms (Mary et al., 2015), which the authors suggest is indicative of more plasticity in younger adults. The increase in resting beta power and enhancement of ERD with age suggest that ageing is associated with difficulty in releasing inhibition to initiate movement.

1.1.2 Beta Rhythm Changes with Pathology

The functional role of beta rhythms have been elucidated through studies in patients with neurological disorders, such as Parkinson's disease (PD) and stroke. PD is a prevalent neurological disorder often associated with bradykinesia (slowness of movement) and overall motor impairment. The primary pathology in PD is the destruction of dopaminergic neurons in the basal ganglia, which results in dopamine depletion and ultimately reduced excitatory input from the thalamus to the motor cortex (Brown, 2003). As measured via LFP recordings during neurosurgery, patients with PD typically exhibit exaggerated beta activity in the basal-ganglia (Brown et al., 2001). Levodopa, a commonly used dopaminergic medication for PD has been shown to attenuate subcortical beta rhythms (Brown et al., 2001). Treatment approaches focusing on attenuating these exaggerated subcortical beta rhythms via high-frequency brain stimulation generally work well to relieve symptoms of bradykinesia (Brown et al., 2004). In the context of the status-quo hypothesis, the strong basal-ganglia beta rhythms maintain the status-quo at the detriment of releasing inhibition to initiate voluntary movement.

Stroke is often followed by impaired motor function associated with the affected hemisphere. Rossiter et al. (2014a) found that patients who experience motor impairments following stroke exhibit diminished beta ERD during movement, with greater reductions in beta ERD correlating with greater motor impairment. Further, stroke patients exhibit excess beta power in the affected hemisphere, with the beta power correlating with poorer motor function (Thibaut et al., 2017). In the context of the status-quo hypothesis, these studies suggest that stroke may somewhat prevent inhibition release thereby making it difficult to initiate voluntary movement. Overall, studies in these patient populations provide support for the inhibitory role of beta oscillations in the human brain.

1.1.3 Pharmacological Manipulation of Beta Rhythms

Cortical beta oscillations can be modulated experimentally via drugs. Administration of diazepam, a GABA_A (specific GABA receptor) agonist, has been shown to increase the amplitude and decrease the frequency of beta oscillations at rest (Jensen et al., 2005; Hall et al., 2010). Further, Muthukumaraswamy et al. (2013) found that administering tiagabine, a drug that elevates the extracellular/synaptic concentration of GABA, prior to a movement task causes an enhanced beta ERD and reduced PMBR. In comparing their results to those from Hall et al. (2011), the authors suggest that beta ERD may be a GABA_A receptor mediated process while PMBR may be GABA_B (a different specific GABA receptor) receptor mediated. These studies provide evidence that GABA plays a major role in sensorimotor beta oscillations and movement.

1.1.4 Summary of Beta Rhythm Characteristics

In summary, beta rhythms are associated with sensorimotor processing yet a unified model as to their functional role still remains elusive. The status-quo hypothesis proposes that beta rhythms are indicative of an active process to maintain the current state of the sensorimotor system and are driven by endogenous mechanisms. Evidence from studying changes in beta rhythms with healthy ageing and in the context of PD finds that excess resting-state beta power is associated with motor impairment. Further, beta rhythm reducing drugs and brain stimulation can relieve akinesia in patients with PD. Evidence for the meaning of the PMBR has accumulated rapidly in recent years, although its exact role remains unclear. The PMBR is virtually absent in children aged 4-6 years, which may reflect reduced GABAergic cortical inhibition, which may in turn facilitate neural plasticity to promote motor learning (Gaetz et al., 2010). It is clear the beta rhythm plays a fundamental role in sensorimotor processing and that its characteristics change with pathology, learning, and aging. A better understanding is needed of the mechanisms that underlie beta rhythms, in order to know how the network that generates the signal is changing. Tying changes in electrophysiology directly to changes in brain structures could pave the way towards the development of better motor learning paradigms, better understanding of and therapies for sensorimotor pathology, and a more detailed view of the healthy aging processes

1.2 Beta Rhythms as a Series of Transient Events

The common interpretation of beta band oscillatory activity as a sustained rhythm arises only as a consequence of averaging neurophysiological recordings in the time-frequency domain (i.e., spectrograms) over multiple trials (Jones, 2016; van Ede et al., 2018). In single trial recordings, beta activity emerges as transient periods of high-power oscillations, herein referred to as *transient events*, each lasting only a few hundred milliseconds. Common descriptive characteristics of transient events are described in Table 1.1. Transient beta events can be thought of as the *building blocks* of the beta band peak observed in the aggregated power spectral density (PSD) representation of electrophysiological recordings. Importantly, representing beta activity as a sustained rhythm can obscure the connection between the signal and the underlying mechanism. For example, a higher amplitude beta band peak in the PSD can be caused by higher amplitude transients or longer duration transients (to name just two) with differing mechanistic underpinnings for each cause. Exploring the characteristics of the transient beta events that underlie beta rhythms may thus provide a more detailed interpretation of neural mechanisms and the beta rhythm's role in sensorimotor processing.

Characteristic	Description	Measurement Unit
Peak Time	Time coordinate of the local maximum (relative to the start time of the epoch).	seconds
Peak Frequency	Frequency coordinate of the local maximum.	Hertz
Normalized Peak Power	The value of the local maximum in signal power. Calculated as the measured signal power at the peak time and peak frequency normalized to either the median power or the aperiodic activity power.	multiples of median power or multiples of aperiodic activity
Burst Rate	Number of events per second. Calculated as the number of events that occur within the epoch divided by the duration of the epoch. Alternative names: Occurrence rate.	Hertz
Frequency Span	The width of the event in the frequency domain. Calculated as the full-width at half maximum of the local maximum along the frequency dimension.	Hertz
Event Duration	The duration of the event in time. Calculated as the full-width at half maximum of the local maximum along the time dimension.	milliseconds or seconds
Oscillatory Cycles	The duration of the event in number of rhythmic cycles. Calculated as the Peak Frequency multiplied by the Event Duration. Alternative names: Episodes, Periods, Cycles	number of oscillations per event

Table 1.1: Common descriptive characteristics of transient burst events

The manifestation of transient events as continuous rhythms upon averaging is depicted in Figure 1.1. Transforming a signal from the time domain to the time-frequency domain (i.e., typically timecourse to spectrogram) is common-practice as it provides a time-varying estimate of the energy of the signal across frequencies. In modern digital signal processing, signal transformation is often accomplished by wavelet decomposition analysis using complex Morlet's wavelets, which consist of a Gaussian-windowed sinusoid. The time-varying energy of the signal, $E(t, f_0)$, at a particular frequency, f_0, (i.e., one row of a spectrogram) is obtained as the square norm of the convolution of the complex wavelet, $w(t, f_0)$, and the measured signal, $s(t)$, namely

$$E(t, f_0) = |w(t, f_0) \times s(t)|^2. \tag{1.1}$$

While the measured signal $s(t)$ fluctuates about zero, the square norm of the convolution provides a positive-only spectrogram $E(t, f_0)$. Thus, $E(t, f_0)$ accumulates upon averaging over several trials (Figure 1.1 a), whereas $s(t)$ cancels (Figure 1.1 b). The accumulation of transient events in single-trial $E(t, f_0)$ imitates the appearance of a sustained rhythm in the average.

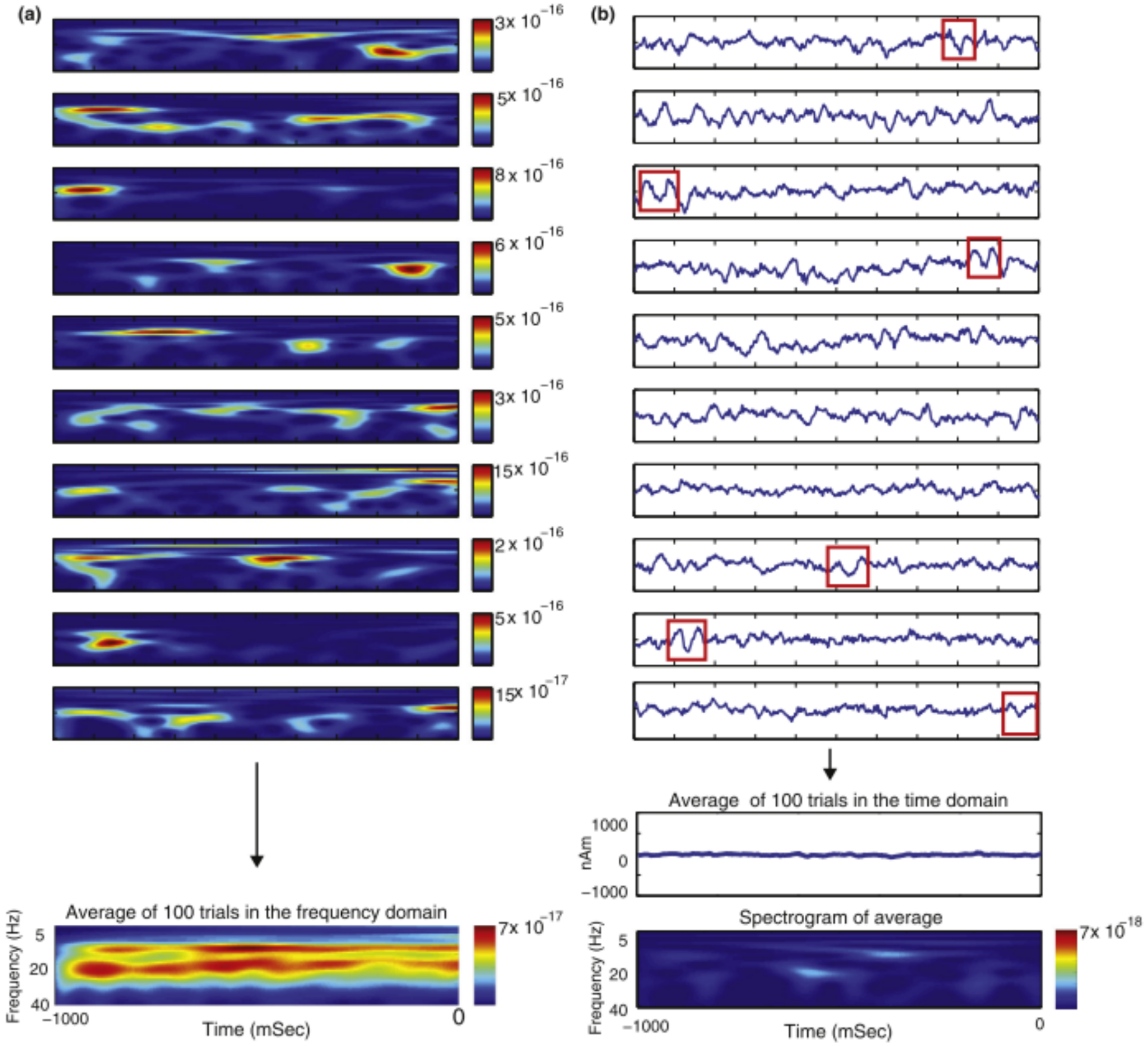

Figure 1.1: (a) Single-single trial spectrograms (1s duration, positive-only) of MEG recordings (source localized to S1) show transient bouts of high power activity (i.e., *transient events*) (top). Positive-only transient events accumulate upon averaging over trials, resulting in what appears like continuous activity in the mu and beta frequency bands (bottom). (b) Corresponding single-trial time-domain recordings (positive and negative currents) show distinct transient event waveforms centered by a large negative trough, as indicated by the red boxes (top). Averaging over 100 time-domain recordings results in cancelling of the negative and positive currents such that the spectrogram of the average timecourse shows no activity. Reproduced from (Jones, 2016)

To study the neural activity that underlies transient events, Murthy and Fetz (1992) recorded extracellular unit activity and LFPs from the motor and somatosensory cortex of two awake monkeys. As shown in Figure 1.2 (a), they found that the

LFP emerges as distinct episodes of oscillatory beta activity with variable amplitude, duration, and frequency, but lasting on average 4-5 oscillatory cycles. They also found (see Figure 1.2 b) that the field potential oscillations were synchronous with the activity of single units. This investigation by Murthy and Fetz (1992) is considered to be pioneering work in the area of transient sensorimotor activity because it showed a clear change in the behaviour of underlying single units during beta bursts.

At this stage it is important to highlight that transient events in the time domain in single-trial extracranial recordings (i.e., M/EEG) are not as apparent as those observed in the LFPs (compare Figure 1.1 b with Figure 1.2 a and b). This discrepancy is primarily a result of better signal-to-noise ratio in LFP recordings due to the proximity to the source and the inverse square law. In human M/EEG recordings, transient events are typically first identified in the time-frequency domain where they are more easily identified in contrast to the background neural activity.

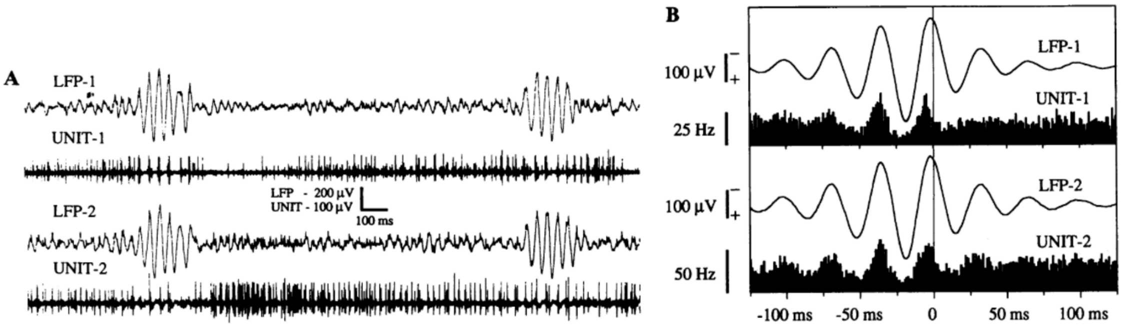

Figure 1.2: (A) LFPs and unit activity recorded at two nearby sites in the motor cortex of one monkey. LFPs were in phase with each other and units tended to discharge during the negative phase of the LFP. Note that positivity is downward in all plots. (B) Cycle-triggered averages of LFPs and unit activity for sites in A. As shown, unit discharge occured during the negative deflections of the LFP. Reproduced from (Murthy and Fetz, 1992).

There is a renaissance of transient events-based analysis of M/EEG recordings amongst the scientific community following work by Shin et al. (2017), who found a direct link between the occurrence of transient beta events and human tactile perception. Namely, they found that beta power reflects the number of transient beta events and that beta events occurring close in time to a light tactile stimulus were likely to impair perception of the stimulus. This work was a follow-up to previous work from the same group (Jones et al., 2010) which found that lower prestimulus beta power in the somatosensory cortex increased the probability of detection of light tactile stimuli. In a more recent report, the same group investigated the mechanisms of beta event generation and found that the detection probability decrease may be attributed to a period of post-event GABA inhibition (Law et al., 2022) (discussed in detail below). This series of manuscripts demonstrates that a transient events based analysis aligns with conventional trial-averaging based analysis while providing a more detailed view of the role of beta rhythm's in sensorimotor processing.

1.2.1 Generative Mechanism of Transient Beta Events

The generative mechanism of transient beta events in the somatosensory cortex has been extensively explored by Sherman et al. (2016) and Law et al. (2022) using a combination of human and animal recordings with computational models. A summary of their findings is presented below.

Transient beta events in somatosensory cortex are generated by synchronous exogenous excitatory synaptic drive to infragranular and supragranular cortical layers. The supragranular drive is stronger, lasts one beta period (~ 50 ms), and is the signal that initiates the occurrence of a beta event. This drive excites distal apical dendrites of neocortical pyramidal neurons, inducing downward dendritic currents. This distal drive is thought to originate from higher-order cortex or higher-order thalamus. The infragranular drive, originating from the lemniscal thalamus, is weaker and broader in time compared to the distal drive. This drive induces proximal current flow in the apical dendrites. The competing distal and proximal current flow are thought to generate the beta event waveform, which strongly resembles an inverted Morlet wavelet. The strong central trough of the waveform arises from the strong distal drive.

Recently, Law et al. (2022) found that the distal drive may also target inhibitory interneurons, recruiting slow-decay inhibitory GABA synaptic currents. In turn, GABA inhibits the spiking of the neocortical pyramidal neurons for up to 300 ms post-event and hence inhibits the relay of sensory information to other parts of the brain. The authors propose that this mechanism underlies beta-burst induced perception suppression observed by Shin et al. (2017). Interestingly, the authors also suggest that the distal drive generates a brief during-event window of excitation where cortical activity is facilitated and perception is enhanced. With this said, the overall consequence of a beta event is somatosensory suppression due to the longer period of GABA inhibition following the event. Further understanding of neural mechanisms relating to beta events requires a clear model of the network generating these signals.

1.2.2 Basal Ganglia-Thalamo-Cortical Sensorimotor Circuit

A reduced model of the basal ganglia-thalamo-cortical sensorimotor circuit with M1 and S1 microcircuits is shown in Figure 1.3. I developed this model using a range of sources as an attempt to unify the transient events generative mechanisms (see section 1.2.1) with the more well established networks involved in overall sensorimotor processing (Mello and Villares, 1997). The S1 microcircuit (top right) is reproduced from Sherman et al. (2016) and Law et al. (2022) and depicts the local network connections that are relevant for the generation of transient beta events (see section 1.2.1 for details). Here, we assume that the same beta event generative mechanisms can be extended to M1 (top left).

In terms of sensorimotor processing, afferent somatosensory information enters this basal ganglia-thalamo-cortical sensorimotor network via the spinal cord and brainstem (path [A]) and passes through the cerebellum prior to reaching the thalamus (bottom right), which in turn relays the information to pyramidal neurons in L4 of S1 (top right) and to M1 (not shown) (Asan et al., 2022). L4 pyramidal neurons in S1 then convey the information to supragranular neurons in L2/3 [B]. The occurrence of a beta event simultaneously generates primary dendritic current flow (which generates the beta wavelet, as shown) and activates inhibitory interneurons in supra and infragranular layers. These excited interneurons inhibit the relay of sensory information to other parts of the brain for around 300 ms post-event, thus inhibiting the perception of tactile stimuli. Pyramidal neurons in S1 L2/3 are also connected via long-range networks to pyramidal neurons in L2/3 in M1 [C]. These networks are plastic and are involved in sensorimotor integration and motor learning (reverse connections, i.e., from M1 to S1, also exist but are not shown) (Asan et al., 2022).

The loop between M1, the basal ganglia, and the thalamus is where movement is shaped and initiated. Motor control exists as a balance of activation of the *direct* (or *Go*) pathway and the *indirect* (or *NoGo*) pathway. Movement is thought to be stimulated in the thalamus via excitatory projections to the motor cortex [D]. The thalamus is typically inhibited via inhibitory projections from the globus pallidus internal (GPi) [E]. When movement is desired, excitatory projections from the cortex [F] stimulate inhibitory projections from the striatum to the GPi, thus preventing the GPi from inhibiting the thalamus. This is the direct pathway. When movement suppression is desired, excitatory projections from the cortex stimulate inhibitory projections from the striatum to the globus pallidus external (GPe), which in turn prevents the GPe from inhibiting the subthalamic nucleus (STN) [G]. The STN is then able to stimulate the GPi via excitatory projections [H], which in turn inhibits the thalamus [E] and suppresses movement. This is the indirect pathway.

The substantia nigra pars compacta (SNc) can modulate GABA release in the striatum via dopaminergic projections, which can inhibit the indirect pathway (or activate the direct pathway) and facilitate movement. As discussed in section 1.1.2, this is one mechanism in which patients with PD (a dopamine depletion disorder) have difficulty initiating movement, and why dopaminergic medications (i.e., Levodopa) help relive akinesia. Furthermore, patients with PD also exhibit exaggerated transient beta bursting emerging from the basal ganglia, which can be suppressed via DBS and dopaminergic medication.

When the *Go* pathway is activated, pyramidal tract neurons in M1 deliver the motor command to the muscles through the brainstem and spinal cord. A copy of the motor command is also delivered to the cerebellum where it is integrated with afferent sensory information, a process important for various sensorimotor tasks and motor learning (Asan et al., 2022). Note that there are many other local and long range network connections in the basal ganglia-thalamo-cortical sensorimotor circuit that are not depicted in this reduced model.

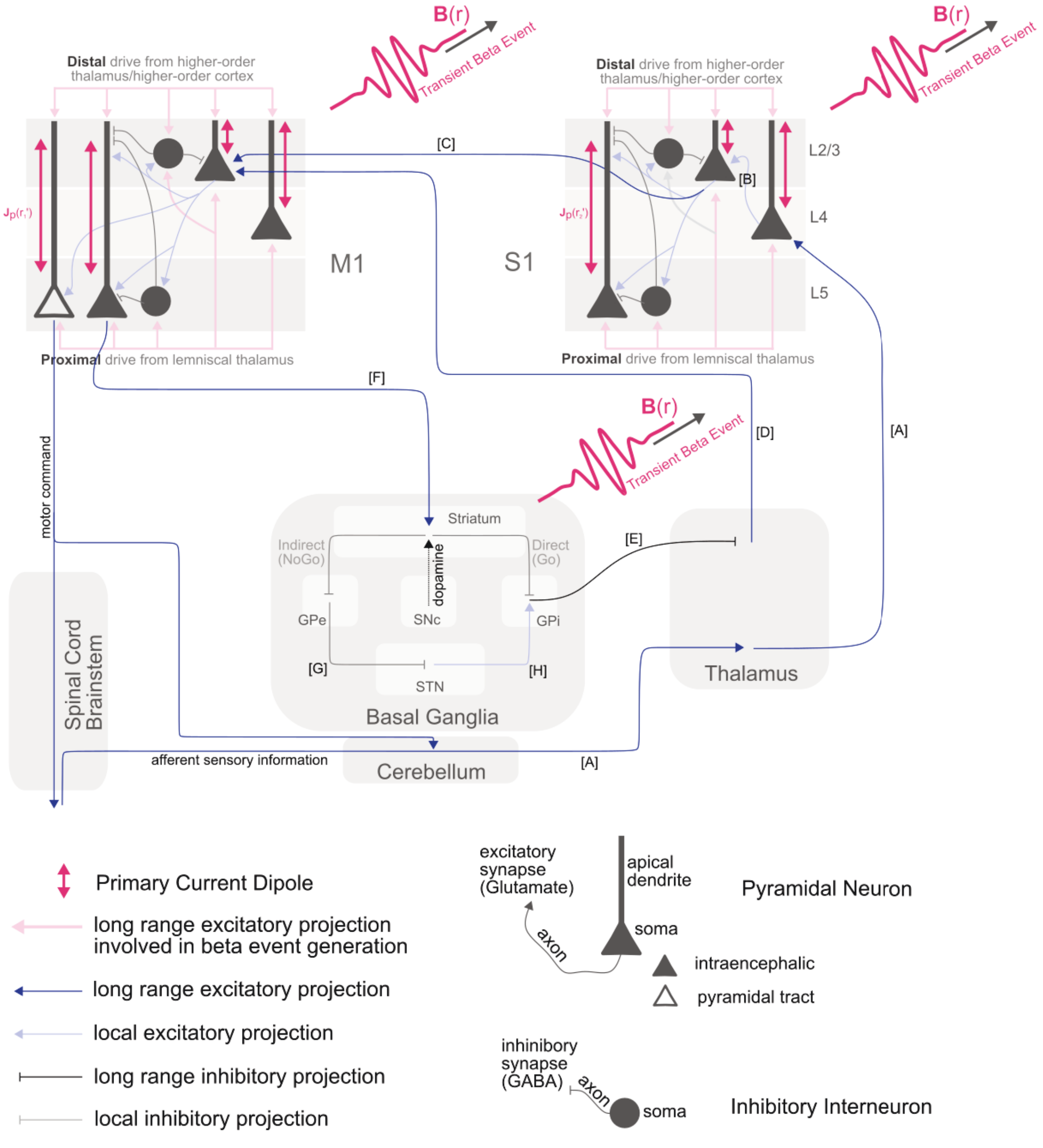

Figure 1.3: Reduced model of the basal ganglia-thalamo-cortical sensorimotor circuit with M1 and S1 microcircuits. See text for details. M1: primary motor cortex, S1: primary somatosensory cortex, $\mathbf{J}_p(\mathbf{r}')$: primary current density, $\mathbf{B}(\mathbf{r})$: magnetic field, GPe: globus pallidus external, GPi: globus pallidus internal, SNc: substantia nigra pars compacta, STN: subthalamic nucleus. GABA: γ-Aminobutyric acid inhibitory neurotransmitter, Glutamate: excitatory neurotransmitter.

1.3 Theoretical Considerations

In this thesis, I will present non-invasive functional neuroimaging studies investigating transient beta events. Below, I provide some background for the relevant imaging modalities.

1.3.1 Functional Neuroimaging via MEG/EEG

The MEG/EEG Forward Problem

The signals measured by MEG and EEG originate primarily from post-synaptic dendritic current flow in cortical pyramidal neurons. MEG and EEG are not sensitive to signals generated from intraceullar current in individual neurons (i.e., insufficient SNR) but are sensitive to signals generated by synchronous current flow in clusters of spatially aligned pyramidal neurons. The flow of information from the neural source activity to sensor-level measurements, via secondary currents in the case of EEG or via magnetic fields in the case of MEG, (i.e., how these signals project forward in space) is described in the *forward problem* of MEG/EEG. In the case of MEG, the magnetic field $\mathbf{B}(\mathbf{r})$ outside of the head generated from a primary current distribution $\mathbf{J}_p(\mathbf{r}')$ within the brain ($\mathcal{V}$) can be obtained via the Biot-Savart Law, i.e.,

$$\mathbf{B}(\mathbf{r}) = \frac{\mu_0}{4\pi} \int_{\mathcal{V}} \frac{\mathbf{J}_p(\mathbf{r}') \times \hat{\boldsymbol{\mathscr{r}}}}{|\boldsymbol{\mathscr{r}}|^2} d\tau' \tag{1.2}$$

where $\boldsymbol{\mathscr{r}} = \mathbf{r} - \mathbf{r}'$ is the separation vector from the source ($\mathbf{r}'$) to the point of interest ($\mathbf{r}$). The cross-product in equation 1.2 reflects how the magnetic field curls around the current source according to the right-hand rule. As described in depth in Hämäläinen et al. (1993), in the context of MEG, it is useful to approximate a localized primary current as a current dipole $\mathbf{Q}$. $\mathbf{Q}$ at position $\mathbf{r}_Q$ can be thought of as a concentration of $\mathbf{J}_p(\mathbf{r}')$ to a single point, namely $\mathbf{J}_p(\mathbf{r}') = \mathbf{Q}\delta(\mathbf{r} - \mathbf{r_Q})$, where $\delta(\mathbf{r})$ is the Dirac delta function at centered at position $\mathbf{r}$. In this approximation, equation 1.2 becomes

$$\mathbf{B}(\mathbf{r}) = \frac{\mu_0}{4\pi} \frac{Q \times \hat{\boldsymbol{\mathscr{r}}}_Q}{|\boldsymbol{\mathscr{r}}_Q|^2} \tag{1.3}$$

where $\boldsymbol{\mathscr{r}}_Q = \mathbf{r} - \mathbf{r}_Q$ is the separation vector from the source ($\mathbf{r}_Q$) to the point of interest ($\mathbf{r}$). Furthermore, as described in depth in Hämäläinen et al. (1993), considering the head as a spherically symmetric volume conductor, current dipoles oriented tangential to the head surface will dominate the MEG signal over current dipoles oriented radially. Thus, given the curl of the field around the current source, the MEG signal can be considered as the radial component (B_z) of equation 1.3, namely

$$B_z(\mathbf{r}) = \frac{\mu_0}{4\pi} \frac{Q \times \hat{\boldsymbol{\mathscr{r}}}_Q}{|\boldsymbol{\mathscr{r}}_Q|^2} \cdot \hat{z} \tag{1.4}$$

where $\hat{z}$ represents the direction normal to head surface. Given the alignment of pyramidal neurons in the cortex, MEG is sensitive to detecting activity in the sulci of the cortex.

Note that the current sources in the cortex can be approximated as point sources since the cell size ($\sim$ 100s μm) $<<$ distance to the MEG/EEG sensors and the distance between sensors ($\sim$ 10s mm). $\mathbf{J}_p$ induces extracellular secondary (volume) currents throughout the head volume and on the surface of the scalp. EEG electrodes measure potentials on the surface of the scalp due to these secondary currents.

The forward problem is the calculation of the EEG/MEG sensor-level signals given the current dipole sources (location, orientation, number, and strength of dipoles) and the geometry/conductivity models of the head. The forward problem can be expressed in matrix notation as

$$\mathbf{x}(t) = \mathbf{A}\mathbf{s}(t) + \mathbf{n}(t) \tag{1.5}$$

where $\mathbf{x}(t)$ is the vector of sensor-level EEG/MEG recordings (sensors × time), $\mathbf{A}$ is the linear forward operator, or the lead-field matrix (sensors × dipole sources), $\mathbf{s}(t)$ is the vector of dipole source timecourses (dipole sources × time), and $\mathbf{n}(t)$ is additive noise (sensors × time). For a single MEG or EEG sensor, i, equation 1.5 can be written as a weighted sum over all dipole sources, j, namely

$$x_i(t) = \sum_j A_{ij} s_j(t) + n_i(t). \tag{1.6}$$

It is clear in equation 1.6 that the measured timecourse at one sensor is modeled as a linear superposition of dipole timecourses (plus additive noise).

The forward problem is a *well-posed* problem in that there is one unique solution,

$\mathbf{x}(t)$, for a given source matrix, $\mathbf{s}(t)$. Computing an accurate forward solution, i.e., computing a representative lead-field matrix $\mathbf{A}$, is nevertheless complex as it depends on the individual's head geometry and tissue conductivity. Current algorithms use subject-specific anatomical magnetic resonance images to generate realistic geometries for head volume conduction. One of these algorithms, called The Boundary Element Method (BEM), is used in Chapters 2 and 3 of this thesis. The BEM considers that the boundaries between tissues most effect the propagation of volume currents and magnetic fields. The BEM models each tissue boundary as a tessellated 2D closed and homogeneous surface. Because currents are significantly attenuated and smeared by low conductivity layers, it is common to consider 3 tissue boundaries in the case of EEG: skin, outer skull, and inner skull. For MEG, because magnetic fields are less affected by biological tissues, it is common to consider only a 1-layer model (inner skull). The Finite Element Method (FEM) is a more accurate alternative head volume conduction compared to BEM as it considers 3D voxels instead of 2D surfaces, however it is significantly more computationally expensive.

The MEG/EEG Inverse Problem

The purpose of functional neuroimaging is to probe the spatio-temporal dynamics of brain activity related to perceptual and cognitive processes. Knowledge of the spatial localization of neural activity in the brain is essential to understanding these perceptual and cognitive processes. The (non-invasive) sensor-level measurements of electric potentials and magnetic fields however have contributions from activity in many brain areas (the forward problem considers dipole sources throughout the brain). The *inverse problem* in MEG/EEG is to estimate the dipole current sources given the MEG/EEG signals at the extracranial sensor locations. The inverse problem can be expressed in matrix notation as

$$\hat{\mathbf{s}}(t) = \mathbf{W}\mathbf{x}(t) \tag{1.7}$$

where $\hat{\mathbf{s}}(t)$ is estimated dipole strength vector (dipole sources × time) and $\mathbf{W}$ is the inverse operator (dipole sources × sensors). Obtaining an estimate of the dipole current sources, $\hat{\mathbf{s}}(t)$, is equivalent to finding an inverse operator $\mathbf{W}$. The inverse problem is an *ill-posed* problem in that, without constraints, there are infinite possible source activity patterns that could generate any measured sensor level data $\mathbf{x}(t)$. This is because the number of modeled dipole sources in the brain is (much) larger than the number of MEG/EEG sensors.

Source estimating algorithms are generally divided into classes based on the approach to obtain the inverse operator, $\mathbf{W}$. The 3 most common classes are dipole fitting, distributed sources models, and beamforming. Dipole fitting attempts to model a pre-specified number of dipole sources with initial guesses as to their locations, orientations, and strengths. Beyond topographies that suggest a single, focal source, results tend not to be robust to different initial conditions, thus limiting reproducibility. Distributed sources models and beamforming are data driven approaches that generate estimates of source activity across the brain. The data driven nature of these approaches mean that reproducibility is assured. Distributed sources models and beamforming were applied in Chapters 3 and 2 of this thesis, respectively, and are discussed in more detail below.

Distributed Sources Models

In Chapter 3 of this thesis, a distributed sources model was used to estimate resting-state MEG timecourses at the centre of mass of 4 separate anatomical ROIs (M1 and S1 left and right). Distributed source models use the measured data to simultaneously fit the amplitudes of a large number of dipoles (typically thousands) at fixed locations *distributed* across the tessellated cortical surface. This avoids the *a priori* assumption of only a few dipole locations necessary for basic dipole fitting and thus avoids the strong dependency on initial conditions. Distributed source models however do assume the source dipoles are distributed at specific locations across the cortex.

In the miminum norm estimates (MNE) approach, the ill-posed inverse problem is addressed by adding the constraint that the best source estimate is the one that minimizes its power while maintaining the requirement that the measured data match those predicted by the model (Hämäläinen and Ilmoniemi, 1994; Lin et al., 2006). This type of minimization problem can be addressed through Tikhonov regularization, which can be used to generate an MNE-derived inverse matrix $\mathbf{W}$ in terms of the forward solution $\mathbf{A}$, the noise-covariance matrix $\mathbf{C}$ (which can be obtained from empty room recordings), and a regularization parameter typically denoted as λ^2. For a complete derivation of the MNE-derived inverse matrix, see (Hämäläinen and Ilmoniemi, 1994; Dale and Sereno, 1993; Lin et al., 2006). The derivation of the MNE-derived inverse matrix assumes that the source matrix $\mathbf{s}(t)$ and noise matrix $\mathbf{n}(t)$ are stationary and Gaussian distributed with zero mean.

The dynamic statistical parametric mapping technique (dSPM) technique (Dale et al., 2000) normalizes the MNE-derived dipole strength (i.e., as described above) by the predicted standard error of the estimate due to additive noise. This establishes the statistical significance of the source current estimate. The noise-normalized source estimate for dipole location j is

$$\mathbf{z}_j(t) = \frac{\mathbf{w}_j \mathbf{x}(t)}{\sqrt{\mathbf{w}_j \mathbf{C} \mathbf{w}_j^T}}, \tag{1.8}$$

where $\mathbf{w}_j$ is the row of the MNE-derived inverse operator matrix corresponding to source dipole j. The normalized dipole strength, $\mathbf{z}_j(t)$, is t-distributed under the null hypothesis of no activity at the current source location j. Since the number of time samples used to calculated the noise covariance matrix C is typically large (i.e., > 100), the t-distribution approaches unit normal distribution and $\mathbf{z}_j(t)$ can be considered a z-score. Note that the y-values plotted in Figure 3.3 (a) are values of $\mathbf{z}_j(t)$.

Beamformers

The following is an exploration of the beamformer in the time domain (as opposed to the frequency domain) for ease of conceptualization.

Beamforming is similar to distributed sources modeling in that dipoles are situated on the tessellated cortical surface (or in a 3D volume), however instead of fitting all dipoles simultaneously, beamforming analyzes one dipole at a time. The inverse operator $\mathbf{W}$ in equation 1.7 is referred to as the *spatial filter*. The role of the spatial filter is to extract data from the dipole source of interest while suppressing activity from all interfering sources (i.e., other dipoles and signal noise). In combining equations 1.5 and 1.7, we can obtain the following,

$$\hat{\mathbf{s}}(t) = \mathbf{W}\mathbf{A}\mathbf{s}(t) \tag{1.9}$$

where we have ignored noise for the sake of a simple intuitive model. In the case of a perfect spatial filter, $\hat{\mathbf{s}}(t) = \mathbf{s}(t)$, equation 1.9 becomes

$$\mathbf{W}\mathbf{A} = \mathbf{I} \tag{1.10}$$

where $\mathbf{I}$ is the identity matrix. This perfect spatial filter has *unit gain* for the dipole of interest and zero gain for all other dipole sources. While this kind of perfect spatial filter is not possible (all sensors inevitably measure signal from all sources) it can be used to constrain the minimization problem. In other words, the problem is to minimize the overall signal power (i.e., variance) of the spatial filter output while preserving (i.e. constraining) unit gain for the dipole of interest. The solution to this constrained minimization problem expresses the spatial filter in terms of the linear forward operator and the sensor data covariance matrix. The ingredients of the beamformer method are thus the forward operator, which combines the volume conduction model (as discussed previously) with co-registered sensor positions, and the experimental (sensor-level) data. This method is known as Linearly Constrained Minimum Variance (LCMV) spatial filtering (Van Veen et al., 1997).

In Chapter 2 of this thesis, the Dynamic imaging of Coherent Sources (DICS) beamformer (Gross et al., 2001) was used to estimate the timecourse at the center of mass of functional ROIs corresponding to the induced responses to a button-press task. DICS is an extension of a time-domain beamformer (i.e., LCMV) to the frequency domain, where cross-spectral density matrices are used instead of the sensor data covariance matrices. DICS was particularly suitable for estimating timecourses in Chapter 2 as we are particularly interested in frequency-specific responses.

Beamformer source estimates assume that the timecourses from multiple sources are uncorrelated. In the case that there is high temporal correlations between the source of interest and a different source, the beamformer may filter out that activity from the source of interest. Note that this is typically only a problem if two correlated sources are far apart (a few cms), as sources close together (i.e., neighboring voxels) will have very similar spatial filters.

1.3.2 Functional Neuroimaging via NIRS

Functional near-infrared spectroscopy (fNIRS or NIRS) is a non-invasive optical neuroimaging technique. It stems from spectrophotometry; a technique used in analytical chemistry to determine the concentration of substances via light absorption and the Beer-Lambert Law (introduced later). fNIRS monitors changes in blood oxy- and deoxy-hemoglobin concentration ([HbO] and [HbR], respectively) as proxies for cortical activation via neurovascular/neurometabolic coupling.

fNIRS and fMRI take similar approaches to imaging brain activity (i.e., via changes in blood oxygenation) and have existed for approximately the same amount of time (Wyatt et al., 1986; Ogawa et al., 1990), yet fMRI is a significantly more popular neuroimaging technique. This is primarily due to most major hospitals already having clinical MRIs with trained technicians, and fMRI requires no additional specialized equipment. fNIRS has no widespread clinical application and is thus a stand-alone imaging modality typically used only for research. Further, fNIRS can only measure superficial activity because NIR spectrophotometry light penetrates only about 1-3 cm into the head (Patil et al., 2011). Since fNIRS is a detector-based imaging modality, source localization is fundamentally limited by the ill-posed inverse problem, as discussed previously in the context of M/EEG. fNIRS is generally considered to have a spatial resolution no-better than about 1 cm (Quaresima and Ferrari, 2019). fNIRS does present some benefits over fMRI, most notably lower up-front and maintenance costs. It requires no magnetic shielding, is portable, and allows some degree of subject movement without substantial artifacts. fNIRS is thus particularly valuable for infant studies, brain-computer interfacing (BCI), and any experiments involving movement. fNIRS can additionally quantify changes in oxy- and deox-hemoglobin concentration whereas fMRI can detect only relative changes in the BOLD signal. Finally, fNIRS has better temporal resolution ($\sim 0.1s$ (Quaresima and Ferrari, 2019)) compared to fMRI ($\sim 1s$ (Soares et al., 2016)), however this is only beneficial in specific instances as generic imaging of neural activation is ultimately limited by the times-scale of neurovascular coupling ($\sim$ seconds).

The near-infrared (NIR) range ($\sim 650 - 950$ nm) is considered the “bio-imaging window” as light in this range can penetrate relatively deep in tissue (a few centimeters), due to relatively low absorption of the skull and of water (Scholkmann et al., 2014). Oxy- and deoxy-hemoglobin however have distinct absorption profiles over this same range, which is fundamental to the ability of fNIRS to separately quantify changes in [HbO] and [HbR]. fNIRS optode montages consist of pairs of light sources (often light-emitting diodes, LEDs) and detectors (often avalanche photodiodes, APDs) typically separated by a few centimeters. The NIR photons emitted by the source will be either scattered or absorbed by the tissues in the head. The unabsorbed photons will reflect out of the head; some reaching the detector. Detected photons typically follow a banana-shaped path, reaching a max depth of about 1-2 cm (Scholkmann et al., 2014). Each neighboring source-detector pair is considered as one fNIRS channel with an effective location at the midpoint.

The most common fNIRS imaging technique (the technique used in Chapter 4 of this thesis) is continuous wave (cw) imaging. In cwNIRS, light is emitted from the source at a constant intensity and frequency (i.e., wavelength). Changes in measured intensity at the detector are assumed to arise only from fluctuations in oxy- and deoxy-hemoglobin concentration. The concentration of all other absorbing substances, and the geometry of the scattering tissues in the head, is assumed to remain constant throughout the measurement. A dual-wavelength measurement is required to separate changes in [HbO] and [HbR] (see next section for a derivation). The choice of the two wavelengths to most accurately determine changes in [HbO] in [HbR] is a complex optimization problem which has been the subject of several reports (see (Scholkmann et al., 2014) for a discussion on this topic). Generally, the two wavelengths must be chosen such that oxy- and deoxy-hemoglobin do not have equal absorption coefficients (equal absorption coefficients happens only around 800 nm in the NIR range).

The Modified Beer-Lambert Law for cwNIRS

The traditional Beer-Lambert law describes the attenuation of light intensity through an absorbing medium, namely

$$I = I_0(\lambda) e^{-\mu_a(\lambda) d}, \tag{1.11}$$

where $I_0(\lambda)$ is the light intensity (at a particular wavelength λ) incident on the medium, $I(\lambda)$ is the remaining light intensity after passing through the medium, d is the length of the medium (i.e., the source-detector distance), and $\mu_a(\lambda)$ is the absorption coefficient of the medium (a function of λ and measured in units of inverse length). Equation 1.11 can be written in terms of optical density, $OD(\lambda)$, as

$$OD(\lambda) \equiv -log\frac{I(\lambda)}{I_0(\lambda)} = \mu_a(\lambda)d. \tag{1.12}$$

The Beer-Lambert law as written in equations 1.11 and 1.12 makes two important assumptions. First, it assumes the medium is homogeneous throughout length d. Second, it assumes there is no loss of intensity due to light scattering. This second assumption limits the use of the Beer-Lambert law for fNIRS as tissues in the brain do scatter light. In fact, NIRS would not exist as a neuroimaging method if brain tissue did not scatter light, as no light would reach the detectors.

The modified Beer-Lambert law describes the change in optical density in scattering media due to changes in absorption. In scattering media, the optical density can be expressed as (Boas et al., 2001)

$$OD(\lambda) = \mu_a(\lambda)d\varphi(\lambda) + G(\lambda), \tag{1.13}$$

where $\varphi(\lambda)$ is pathlength factor and $G(\lambda)$ is a scattering factor that accounts for measurement geometry. The pathlength factor $\varphi(\lambda)$ accounts for increased distance that photons travel from the source to the detector as a result of scattering (and absorption). A change in chromophore concentration (i.e., oxy and deoxy-hemoglobin) changes the absorption coefficient but the other variables on the right-side of equation 1.13 remain the same (Strangman et al., 2003), thus

$$\Delta OD(\lambda) = -log\frac{I_f(\lambda)}{I_i(\lambda)} = \Delta\mu_a(\lambda)d\varphi(\lambda). \tag{1.14}$$

Note that in the case of no scattering, $\varphi(\lambda) = 1$ and the traditional Beer-Lambert relationship is recovered.

In the context of NIRS for neuroimaging, cortical activation induces changes in oxy- and deoxy-hemoglobin concentration. Assuming the changes in these two hemoglobin species dominate the changes in total absorption, $\Delta\mu_a(\lambda)$ can be written as

$$\Delta\mu_a(\lambda) = \varepsilon_{\mathrm{HbR}}(\lambda)\Delta[\mathrm{HbR}] + \varepsilon_{\mathrm{HbO}}(\lambda)\Delta[\mathrm{HbO}], \tag{1.15}$$

where [HbO] and [HbR] are oxy- and deoxy-hemoglobin concentrations and $\varepsilon_{\text{HbO}}(\lambda)$ and $\varepsilon_{\text{HbR}}(\lambda)$ are the respective extinction coefficients. A set of two NIRS measurements (separated in time) at a particular wavelength gives the ratio $I_f(\lambda)/I_i(\lambda)$ in equation 1.14. Furthermore, the source-detector distance, d, is determined by the optode configuration, and $\varphi(\lambda)$ is typically just set to a constant value (often $\varphi(\lambda) = 6$ based on (Delpy et al., 1988)). Thus fNIRS measurements can be mapped to changes in absorption coefficient, $\Delta\mu_a(\lambda)$, via equation 1.14. Considering a two-wavelength (λ_1 and λ_2) measurement, as discussed previously, equation 1.15 can be rearranged to directly solve for oxy- and deoxy-hemoglobin concentrations:

$$\Delta[\text{HbR}] = \frac{\varepsilon_{\text{HbO}}(\lambda_2)\Delta\mu_a(\lambda_1) - \varepsilon_{\text{HbO}}(\lambda_1)\Delta\mu_a(\lambda_2)}{\varepsilon_{\text{HbR}}(\lambda_1)\varepsilon_{\text{HbO}}(\lambda_2) - \varepsilon_{\text{HbO}}(\lambda_1)\varepsilon_{\text{HbR}}(\lambda_2)} \tag{1.16}$$

$$\Delta[\text{HbO}] = \frac{\varepsilon_{\text{HbR}}(\lambda_1)\Delta\mu_a(\lambda_2) - \varepsilon_{\text{HbR}}(\lambda_2)\Delta\mu_a(\lambda_1)}{\varepsilon_{\text{HbR}}(\lambda_1)\varepsilon_{\text{HbO}}(\lambda_2) - \varepsilon_{\text{HbO}}(\lambda_1)\varepsilon_{\text{HbR}}(\lambda_2)} \tag{1.17}$$

Note that equations 1.16 and 1.17 show that cwNIRS provides only the *change* in oxy- and deoxy-hemoglobin concentration (relative to some baseline level) as opposed to absolute concentrations. Furthermore, the assumption of the Beer-Lambert law brought up earlier (i.e., the medium is homogeneous throughout length d and therefore absorption occurs homogeneously over the full pathlength) means that these concentration changes are typically underestimates of the true changes.

1.4 This Work

In this thesis, we explore sensorimotor transient beta events in non-invasive human neurophysiological recordings in terms of how they change with movement and with healthy aging, and in terms of their coupling to neurovascular dynamics. This thesis is comprised of three manuscripts:

Manuscript 1 (Ch. 2 of this thesis) addresses the following two objectives: (1) to detect and characterize transient beta bursts over the ipsilateral and contralateral primary sensorimotor cortices during a unilateral motor task performance and during wakeful resting, and (2) to identify age-related changes in beta burst characteristics, in the context of earlier reports of age-related changes in beta suppression and the post-movement beta rebound. The results detailed in manuscript 1 show explicitly transient events-based analysis generates results that align with, instead of contradicting, traditional sustained rhythm-based analysis while providing a more detailed description of sensorimotor beta activity and specifically how it changes with motor task-engagement and with healthy aging. Manuscript 1 is published as follows:

Brady, B., Power, L., & Bardouille, T. (2020). Age-related trends in neuromagnetic transient beta burst characteristics during a sensorimotor task and rest in the Cam-CAN open-access dataset. NeuroImage, 222, 117245.
https://doi.org/10.1016/j.neuroimage.2020.117245

Manuscript 2 (Ch. 3 of this thesis) details a new algorithm for detecting transient events in non-invasive neurophysiological recordings called the Periodic/Aperiodic Parameterization of Transient Oscillations (PAPTO). Manuscript 2 follows from manuscript 1 where we notice that transient event characteristics and their age-related changes are conflated with underlying age-related changes in aperiodic neural activity. Manuscript 2 addresses the following two objectives: (1) to motivate and validate the PAPTO algorithm, and (2) to use PAPTO to disambiguate adult lifespan changes in the aperiodic activity power spectrum and transient event characteristics. The results detailed in manuscript 2 are valuable both in terms of understanding the healthy ageing process and in terms of consolidating the understanding of the resting-state beta's role in somatosensory processing. Manuscript 2 is published as follows:

Brady, B., & Bardouille, T. (2022). Periodic/Aperiodic parameterization of transient oscillations (PAPTO)-Implications for healthy ageing. NeuroImage, 251, 118974. https://doi.org/10.1016/j.neuroimage.2022.118974

Manuscript 3 (Ch. 4 of this thesis) addresses the following two objectives: (1) to extract the burst-evoked hemodynamic response function for transient mu, beta, and gamma events using resting state recordings, and (2) to evaluate the contribution of neurovascular changes evoked by transient events to the total measured hemodynamic response over a unilateral finger-tapping motor task. Manuscript 3 utilizes the transient events analysis framework to help explain mechanistic details underlying neurovascular coupling. Manuscript 3 is still in preparation for submission for publication.

Chapter 2

Age-related trends in neuromagnetic transient beta burst characteristics during a sensorimotor task and rest in the Cam-CAN open-access dataset

The text below was published in November 2020 in *NeuroImage*. *NeuroImage* is a peer-reviewed journal. The reference is provided below.

Brady, B., Power, L., & Bardouille, T. (2020). Age-related trends in neuromagnetic transient beta burst characteristics during a sensorimotor task and rest in the Cam-CAN open-access dataset. NeuroImage, 222, 117245.
https://doi.org/10.1016/j.neuroimage.2020.117245

See Appendix C for copyright permissions.

2.1 Abstract

Non-invasive neurophysiological recordings, such as those measured by magnetoencelography (MEG), provide insight into the behaviour of neural networks and how these networks change with factors such as task performance, disease state, and age. Recently, there has been a trend in describing neurophysiological recordings as a series of transient bursts of neural activity rather than averaged sustained oscillations as burst characteristics may be more directly correlated with the neurological generators of brain activity. In this work, we investigate how beta burst characteristics change with age in a large open access dataset. The objectives are (1) to detect and characterize transient beta bursts over the ipsilateral and contralateral primary sensorimotor cortices during a unilateral motor task performance and during wakeful resting, and (2) to identify age-related changes in beta burst characteristics, in the context of earlier reports of age-related changes in beta suppression and the post-movement beta rebound. MEG data, acquired at the Cambridge Centre for Ageing and Neuroscience, of roughly 600 participants with a nearly uniform distribution of ages between 18 and 88 years old was used for analysis. We found that burst rate is the predominant factor related to age-related changes in the amplitude of the induced beta rhythm responses associated with a button press task. Furthermore, we present a cross-validation of burst parameters detected at the sensor- (peak sensor and sensor ROI) and source-level (beamformer spatial filter). This work is as an important step in characterizing transient bursts in neuromagnetic signals in the temporal domain, towards a better understanding of the healthy aging human brain.

2.2 Introduction

Non-invasive neurophysiological recordings provide insight into the behaviour of neural networks, and how these networks change with factors such as task performance, disease state, and age. The human motor system serves as an effective platform to study cortical oscillation dynamics in relatively simple experimental paradigms. A sensorimotor event, such as a voluntary movement or a sensory stimulus, is associated with measurable, stereotypical modulations in the power of mu (10-15 Hz), beta (15-30 Hz), and gamma ($>$ 30 Hz) band signals (Rossiter et al., 2014b)(Engel and Fries, 2010)(Shin et al., 2017)(Pfurtscheller et al., 1996). In the mu and beta bands, oscillatory activity is understood to be generated by an inhibitory thalamocortical neural system. Thus, a reduction in signal strength represents an activated state of processing in the underlying cortical network (i.e., facilitation), whereas an increase represents stronger inhibition (Pfurtscheller and Lopes da Silva, 1999). Conversely, oscillatory activity in the gamma band is understood to be excitatory in nature, and is likely generated by more local circuitry. Changes in the dynamics of these oscillatory signals have been directly associated with neurological conditions, including stroke and Parkinson's disease (Rossiter et al., 2014a)(Brown, 2007)(Little and Brown, 2014).

The induced responses occurring during a button press task include changes in mu, beta, and gamma band activity, which are generally elucidated by calculating the average spectral power across a number of task repetitions (or "trials"). Immediately preceding and during the button press (-100 - 500 ms relative to the button press), a decrease in average spectral power in the mu and beta bands, compared to an earlier "baseline" interval, localizes bilaterally in the primary motor and somatosensory cortices with contralateral dominance (Pfurtscheller and Aranibar, 1977)(Bardouille and Bailey, 2019)(Pfurtscheller and Lopes da Silva, 1999)(Pfurtscheller et al., 1997)(Hari et al., 1997)(Crone et al., 1999). This decrease in average spectral power is often referred to as event-related desynchronization (ERD), or rhythm suppression. In the time following the button press (500 - 1250 ms relative to the button press), the average spectral power in the beta band is higher than the baseline interval, an effect known as the post-movement beta rebound (PMBR), which localizes slightly anterior and medial relative to the localized suppression (Pfurtscheller et al., 1996)(Bardouille and Bailey, 2019)(Gaetz and Cheyne, 2006). The mu rhythm shows no such rebound characteristic (Bardouille and Bailey, 2019). Furthermore, a low intensity increase in average spectral power occurs for a duration of roughly 400 ms temporally centered on the button press in the gamma band. This example of event-related synchronization (ERS) is known as the movement-related gamma burst (MRGB) and localizes to the contralateral primary motor cortex with some somatosensory representation (Bardouille and Bailey, 2019)(Pfurtscheller et al., 1994)(Cheyne et al., 2008)(Cheyne and Ferrari, 2013)(Muthukumaraswamy, 2011). Thus, changes in cortical oscillations can be characterized temporally and spatially as ERS and ERD, based solely on changes in average spectral power (Pfurtscheller and Lopes da Silva, 1999).

It is generally accepted that cortical oscillations change with healthy aging (Rossini et al., 2007). The induced oscillatory dynamics in response to a basic motor task are generally fully evident by late adolescence in healthy individuals. In particular, mu and beta ERD are strong in all age groups (Wilson et al., 2010) while children in the 11-13 age range show the greatest MRGB compared to younger children and adults (Gaetz et al., 2010). The PMBR on the other hand shows a developmental time course with limited expression in young children (4-6 years old), a significant increase in prominence around 13 years, and a further increase into adulthood (Gaetz et al., 2010)(Gaetz et al., 2020). On the other end, beta oscillations have been linked to the inhibitory neurotransmitter gamma-aminobutyric acid (GABA) which shows greater inhibitory activity within the motor cortices of older subjects (Rossiter et al., 2014b). Recently, age-related changes in the movement-related induced responses have been shown in a large dataset consisting of magnetoencephalographic (MEG) recordings of roughly 700 healthy adults with a nearly uniform distribution of participant ages between 18 and 88 years (Shafto et al., 2014)(Taylor et al., 2017). Bardouille and Bailey (2019) found that the movement-related response in the contralateral primary motor cortex shifts to lower spectral power with increasing age. Specifically, they found decreasing PMBR amplitude, PMBR frequency, and MRGB amplitude as well as increasing beta suppression amplitude with age. These age-related changes in the induced responses verify many previous reports in studies with smaller datasets (Babiloni et al., 2004)(Labyt et al., 2003)(Schmiedt-Fehr et al., 2016)(Christov and Dushanova, 2016)(Sallard et al., 2016)(Toledo et al., 2016)(Cheyne and Ferrari, 2013).

However, the reported age-related effects focus on measures of average spectral power, which fail to capture how individual oscillatory bursts are changing with age. Research linking these age-related changes in average spectral power change to the characteristics of transient bursts will provide a clearer understanding of how neural networks change with age.

Recent studies support the idea that the complexity of brain activity is not completely captured using spectral averaging techniques (Cole and Voytek, 2017)(Jones, 2016). It has been shown that raw neurophysiological recordings show transient bursts of high-power activity lasting on the order of hundreds of milliseconds and that it is only through averaging over many trials that we observe oscillatory dynamics that appear to be sustained for longer periods of time (van Ede et al., 2018)(Jones, 2016). For example, recent work has shown, across various tasks and species, that an increase in beta band average spectral power in the primary somatosensory cortex specifically is due to an increase in the occurrence rate of transient beta bursts in the raw neurophysiological recordings (Shin et al., 2017). Some alternate hypotheses for an increase in spectral power include longer duration bursts, bursts with a larger signal amplitude, or bursts with a wider frequency span. Each of these hypotheses is supported by different changes in the underlying neural circuitry. Thus, the characteristics of transient bursts contain crucial information for understanding the generators of induced responses, including identifying changes in the underlying neural systems (Murthy and Fetz, 1992). Computational modeling to generate stereotypical transient bursts is thus an emerging technique in the literature, hinting at the possibility of developing a dictionary that relates burst waveform shapes to the underlying physiology (Cole and Voytek, 2017)(Jones, 2016). For example, Sherman et al. (2016) used a combination of human MEG, computational modeling, and laminar recordings in animals to show that excitatory input to proximal and distal dendrites in pyramidal neurons in the primary sensorimotor cortex is a possible mechanistic origin for transient bursts in the beta band.

In this report, we apply a transient burst analysis framework to MEG data from the Cam-CAN open-access dataset. The objectives are (1) to detect and characterize transient beta burst events over the ipsilateral and contralateral primary sensorimotor cortices during a unilateral motor task performance and during wakeful resting in a large open-access dataset, and (2) to identify age-related changes in beta burst characteristics, in the context of earlier reports of age-related changes in beta suppression and the post-movement beta rebound. We hypothesize that age-related trends in transient beta burst characteristics will reflect those previously found in the average spectral power analysis of the same data. We investigate transient bursts through sensor-level as well as source estimation (beamformer spatial filter) techniques. To our knowledge this work is the first attempt of validation that the beamformer provides an accurate representation of the characteristics of individual transient events at the source level.

2.3 Methods

Text from Bardouille and Bailey (2019) is adapted in sections 2.1 - 2.4 for clarity and consistency.

2.3.1 Participants & Experimental Paradigm

Six hundred and fifty participants had MEG data obtained during the performance of the simple cued-button pressing task in Phase 2 of the Cam-CAN examination of healthy cognitive ageing. Participant ages ranged from 18 to 88 years of age, with an equal distribution in age per decile and equal proportions of males and females. Following exclusions (described in section 2.4), we report findings from 596 participants (91.7% of the original 650 datasets). Each participant performed the “Sensorimotor task” and a “Resting state” scan (Shafto et al., 2014). In the sensorimotor task, participants responded with a right index finger button press to unimodal or bimodal audio/visual stimuli. The order of bimodal and unimodal trials was randomized, and the inter-trial interval varied between 2 and 26 s. The button press task did not include specific imperatives related to performance (e.g., fast responses). Thus, brain-behaviour interactions focused on response time were not investigated in this report. In the resting state scan, data were acquired for 8 minutes and 40 seconds while participants rested with their eyes closed. The first 20 seconds of the resting data were discarded.

2.3.2 Data Acquisition

Data were obtained from the Cam-CAN repository (available at http://www.mrc-cbu.cam.ac.uk/datasets/camcan/; (Shafto et al., 2014)(Taylor et al., 2017)). MEG data were acquired at 1000 Hz with inline band-pass filtering between 0.03 and 330 Hz using a 306-channel Vectorview system with continuous head position monitoring (Elekta Neuromag, Helsinki, Finland). Digitization of anatomical landmarks (i.e., fiducial points; nasion and left/right preauricular point) as well as additional points on the scalp was also performed for registration of MEG and MRI coordinate systems. Electrooculogram (EOG) and electrocardiogram (ECG) were recorded concurrently. T1-weighted magnetic resonance images (MRI) were acquired using a 3T Siemens Tim Trio system with a 32-channel head coil.

2.3.3 MRI Data Analysis

Each participant's MRI was reconstructed using the FreeSurfer recon-all algorithm (Dale et al., 1999)(Fischl and Dale, 2000)(Fischl et al., 1999a)(Fischl et al., 1999b)(Fischl et al., 2001)(Fischl et al., 2002)(Fischl et al., 2004)(Desikan et al., 2006). The reconstruction process provided a digitization of the cortical surface for source estimation, a transformation to the average (i.e., fsaverage) brain for spatial normalization and group statistics, and a boundary element model of the brain to provide more accurate calculation of the forward solution (Hamalainen and Sarvas, 1989). Locations for source estimation were defined covering the entire cortical surface with 5 mm spacing. Finally, each participant's MRI data was registered to the MEG data based on the alignment of anatomical landmarks (i.e., fiducials) in MEG and MRI, and MEG head digitization with the scalp as visualized on the MRI (MNE python coreg, v.0.14) using a semi-automated process (Bardouille and Bailey, 2019).

2.3.4 MEG Pre-Processing

Data was pre-processed by the Cam-CAN group using temporal signal space separation to perform environmental noise reduction, reconstruction of missing or corrupted MEG channels, continuous head motion correction, and a transform of each dataset to a common head position (Taulu and Simola, 2006). All subsequent MEG processing was completed in the Python programming environment (v.2.7.13), using the MNE-python library (v.0.18.1) (Gramfort et al., 2014). Raw MEG data were low-pass filtered at 125 Hz and notch filtered at 50 Hz and 100 Hz to remove signals related to power lines. Data pre-processing proceeded as previously described (Bardouille and Bailey, 2019). Briefly, the task data was parsed into trials synchronized to each button press, with a duration of 3.4 s and a 1.7 s pre-stimulus interval. Trials were excluded if the button press occurred more than 1 s after the cue (indicating poor task performance) or if the button press occurred within 3 s of the previous button press (which provided insufficient baseline for subsequent analysis). Participants with less than 55 trials after these exclusions were excluded from further analysis. The rest data were cropped to a single 210 s trial including 105 s prior to and following the midpoint of the resting data. The length of this trial was chosen to be approximately equal in length to the sum of all task trials. Independent component analysis was performed on the task and rest data using the FASTICA algorithm (Hutchinson et al., 2002)(Delorme et al., 2007) to remove artifacts using a fully automated process. This process resulted in cleaned MEG task data (i.e., channels x time x trials) and cleaned rest data, which were used for time-frequency analysis and burst mapping.

2.3.5 Transient Burst Detection and Calculating Burst Characteristics

Time-frequency response (TFR) plots of spectral power were generated by convolving each trial of the cleaned MEG task data with a complex Morlet wavelet. Morlet wavelet analysis was performed between 1 and 100 Hz with 1 Hz resolution and the power was calculated as the square magnitude of the complex wavelet-convolved data. To investigate changes in average power, each TFR plot was normalized to the mean value in the pre-stimulus interval and averaged across trials and participants to generate a grand-average TFR. Topographic maps, as shown in Figure 2.1 (a), of average beta power change immediately preceding/during the button press ($-0.1 < t < 0.5$ s) and following the button press ($0.5 < t < 1.25$ s) were generated by plotting the grand-average power change within the beta frequency band and appropriate time interval to the sensor array.

Based on the topographic maps shown in Figure 2.1, we selected one channel, herein referred to as the "Peak Sensor", from each hemisphere for detecting beta bursts. Channels MEG0221 (left, contralateral) and MEG1311 (right, ipsilateral) were selected as the peak sensors because they overlay the left and right sensorimotor areas, were strongly sensitive to changes in the beta rhythm (likely occurring in the primary sensorimotor cortex), are far away from the midline (to ensure sensitivity to one hemisphere only), and are in mirrored positions on the sensor array. In an effort to mitigate spatial variability between subjects, we additionally detected transient bursts over a wider region of interest (ROI) of sensors, herein referred to as "Sensor ROI", consisting of 7 sensors in each hemisphere centered around (and including) each peak sensor. Sensor ROIs for each hemisphere are indicated by numbers 1 through 7 in Figure 2.1 (a). Sensor ROI single-trial TFRs (TFR_{ROI}) were generated from a weighted sum of the individual sensor single-trial TFRs (TFR_i), namely

$$TFR_{ROI} = \sum_{i=1}^{7} \Big(\omega_i \cdot TFR_i \Big) \tag{2.1}$$

where (ω_i) are the normalized sensor weights. Sensors were weighted based their relative contributions to average power change during the movement-related beta suppression and PMBR, i.e.

$$\omega_i = \chi \phi_i + (1 - \chi) \tau_i \tag{2.2}$$

where the contribution of beta ERD to the total power change due to both beta responses across the ROI, χ, is given as

$$\chi = \frac{\sum\limits_{i=1}^{7} |P_i^{ERD}|}{\sum\limits_{i=1}^{7} \Big(|P_i^{ERD}| + |P_i^{PMBR}| \Big)} \tag{2.3}$$

with each sensor's relative contribution to the beta ERD, ϕ_i, given as

$$\phi_i = \frac{|P_i^{ERD}|}{\sum\limits_{i=1}^{7} |P_i^{ERD}|} \tag{2.4}$$

and each sensor's relative contribution to the PMBR, τ_i, given as

$$\tau_i = \frac{|P_i^{PMBR}|}{\sum_{i=1}^{7} |P_i^{PMBR}|} \tag{2.5}$$

where $|P_i^{ERD}|$ and $|P_i^{PMBR}|$ are the power change at sensor i in the ERD and PMBR time intervals, respectively. The resulting normalized sensor weights, which are generally close to one-seventh, are shown in Figure 2.1 (b).

In an effort to address spatial variability by source estimation, we also detected and characterized transient bursts at the source level. Here, we used a beamforming approach to estimate activity on the cortical surface based on previously reported functional ROIs for each induced response (Bardouille and Bailey, 2019), herein referred to as the "Source" method. Briefly, the dynamic imaging of coherent sources beamformer was used for each participant to generate functional maps constrained to the cortical surface with unit-noise gain normalisation) of the movement-related beta suppression and PMBR (Gross et al., 2001; Sekihara and Nagarajan, 2008). Each set of functional maps were spatially normalised to the fsaverage brain, and combined to generate a functional ROI for each response. The functional ROI was transformed back to each participant's MRI coordinate frame. Following this, a time course of estimated source activity was generated at the centre of mass of the ROI (x=-32 mm, y=-19 mm, z=47 mm; FreeSurfer Talairach coordinates) using the participant's cleaned and epoched MEG data. Data analysis scripts to generate the functional ROI can be found: https://github.com/tbardouille/camcan_MovementInducedResponses. This time course was used to detect and characterise transient spectral events at two sources: one that localizes the beta suppression and one that localizes the PMBR. This method provided transient events in the hemisphere contralateral to movement only.

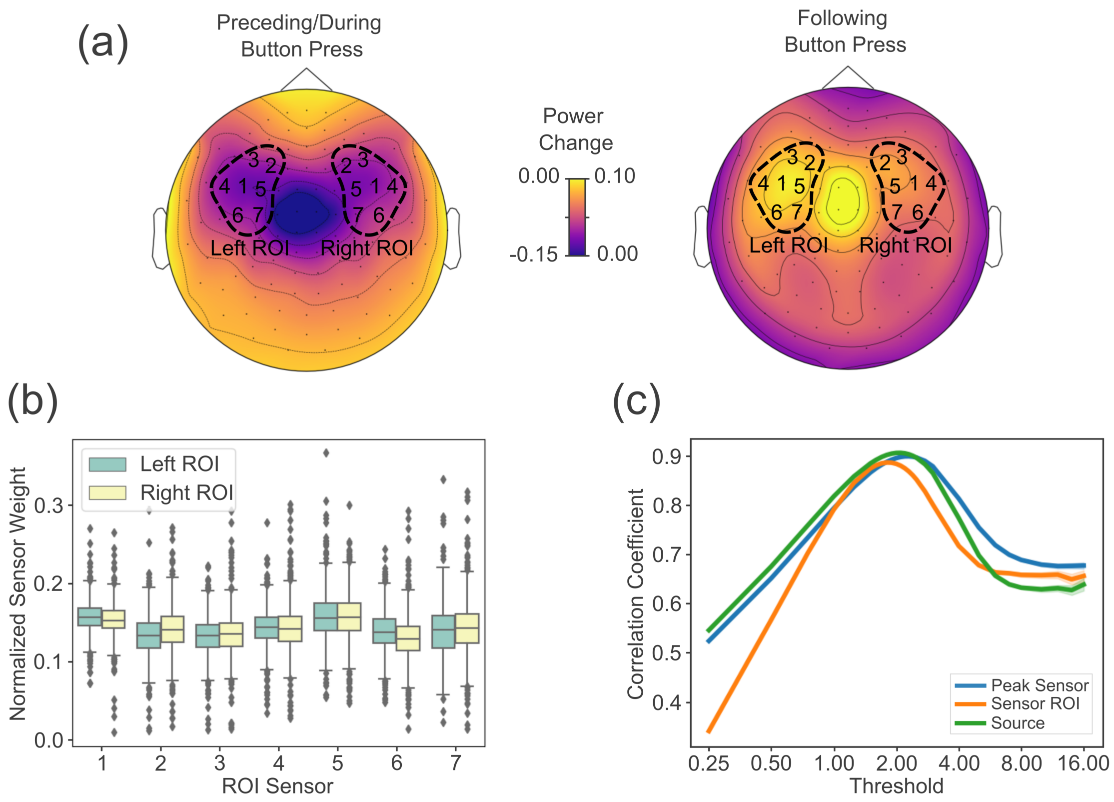

Figure 2.1: (a) Grand-average beta rhythm spectral power change (log ratio) topographies of the movement and post-movement phases relative to pre-movement. Sensor ROIs for each hemisphere are indicated by numbers 1 through 7, where Left ROI consists of [1:MEG0221, 2:MEG0321, 3:MEG0341, 4:MEG0211, 5:MEG0411, 6:MEG0231, 7:MEG0441] and Right ROI consists of [1:MEG1311, 2:MEG1231, 3:MEG1221, 4:MEG1321, 5:MEG1121, 6:MEG1341, 7:MEG1131]. (b) Normalized sensor weights calculated via equation (2). Each box plot shows the distribution of weights across all subjects. (c) Correlation coefficient as a function of threshold (note: log scale) for detecting transient events for each analysis method. Curves are averaged over all participants and trials with the 95 % confidence interval shown.

Transient spectral bursts were detected and characterised for all participants using a process described in detail by Shin et al. (2017) (https://github.com/hs13/BetaEv). As an initial step for burst detection and characterisation, local maxima in spectral power were found in the single-trial TFRs ($1 \leq f \leq 100$ Hz with a 1 Hz step). Bursts were defined as local maxima in the single-trial TFR plot with spectral power above a threshold value (described as a multiple of the median value for that frequency). The threshold value was calculated independently for each of the three analysis methods based on a process by Shin et al. (2017). In short, the correlation coefficient between the mean pre-stimulus beta spectral power and the percent pixels above the threshold power in the pre-stimulus spectrogram (both as a function of time) was calculated for various threshold values, and for every trial and participant. The threshold corresponding to the maximum correlation coefficient was chosen as the threshold for transient burst detection. Figure 2.1 (c) shows the correlation coefficient as a function of threshold averaged over all trials and participants for each of the three analysis methods. The resulting data-driven power thresholds for defining transient bursts were 2.3x the median for peak sensor, 1.8x the median for sensor ROI, and 2.1x the median for source.

For each burst, the peak power at the local maximum was normalized to the median power for that frequency bin to record the *normalized peak power* of the burst, while the time and frequency coordinates of the local maxima represent the *peak time* and *peak frequency*, respectively. The *event duration* and *frequency span* of the bursts were calculated as the full-width at half maximum (FWHM) of the local maxima along the time and frequency dimension, respectively. *Burst rate* was calculated as the number of events that occur within a given time range across all trials divided by the total time. Bursts were categorised as occurring during the pre-movement (-1.25 s to -0.25 s relative to the button press), movement (-0.25 s to 0.25 s relative to the button press), and post- movement (0.25 s to 1.25 s relative to button press) phases. The choice of these time intervals was guided by the distinct phases evident in the distribution of beta burst peak times across all data, as shown in Figure 2.2 (a) and (b). An event was considered to fall within a given phase if the peak time was within the associated time range, and burst rate was calculated separately for each phase. Burst characteristics were also calculated, as described above for the resting state MEG data by treating the 210-second rest dataset as one trial.

2.3.6 Statistical Analysis of Age-Related Effects

Regression was used to reveal statistically significant relationships between age and burst characteristics. Linear and quadratic models were investigated for each characteristic, with the most appropriate model selected by comparing chi-square values via an F-test (quadratic model was selected if F-stat $>$ 4, corresponding to a 95%

confidence level). If a linear model was deemed most appropriate, a statistically significant non-zero age-related trend was determined if $\chi^2_{min} < 3$ and p-value < 0.05. Additionally, multiple comparisons were taken into account by adjusting the false discovery rate (0.5 %) using the Benjamin-Hochberg Procedure. If a quadratic model was deemed most appropriate, statistical significance was determined if $\chi^2_{min} < 3$. Analysis was focused on the hemisphere contralateral to movement. For each participant, event duration, normalized peak power, peak frequency, and frequency span were tabulated separately for all events occurring in the rest, pre-movement, movement and post-movement phases. Burst rate was also calculated for each participant in each phase. Regression was performed for each burst characteristic on all bursts across participants during each phase, with age as the independent variable.

2.4 Results

2.4.1 Burst Characteristics

To investigate the movement related burst dynamics as a function of peak time and peak frequency, Figure 2.2 (a) shows 2D histograms of transient burst peak times and peak frequencies over all trials and participants (approximately 37,000 total trials) for all three analysis methods. 2D histograms are shown for both hemispheres for the sensor-level analysis methods and for the two source-level functional ROIs (ERD and PMBR). Each histogram has a bin width is 0.062 s in the time domain and 4 Hz in the frequency domain. There are relatively few mu and beta bursts throughout the movement phase, which is likely a major source of the decrease in average power associated with mu/beta suppression. In the post-movement phase, there is an increase in the occurrence of bursts in the beta band as compared to pre-movement, which is likely a major source of the increase in average power usually referred to as the post-movement beta rebound. Figure 2.2 (a) shows some non-periodic frequency banding in all histograms between 45 and 85 Hz, which we associate with different median burst power (i.e. unique burst threshold criteria) for each frequency.

In addition, Figure 2.2 (a) peak sensor and sensor ROI histograms both show a subtle increase in the occurrence of bursts in the gamma band during the movement phase, which matches in time and frequency with the previously reported movement-related gamma burst. The source histogram shows no such gamma burst suggesting source estimation based on the beta ERD functional ROI is not sensitive to the increase in the gamma band burst rate. Figure 2.2 (a) provides a verification that a burst analysis approach is effective in explaining previously observed so-called beta band “induced responses” in this experimental paradigm but is less sensitive to transient events in the gamma band. Thus, we focus our attention to the bursts occurring in the beta band from here on.

To focus on the beta band dynamics and elucidate the hemispheric laterality of induced responses, Figure 2.2 (b) shows the normalized distributions of beta burst peak time aggregated over the beta frequency range for each analysis method and each hemisphere. This result supports the chosen time windows for each phase of the button press response as described in section 2.5. The reduction in normalized transient burst counts from the pre-movement to the movement phase is approximately equal in both hemispheres for the sensor-level methods, suggesting the beta suppression is a symmetric bilateral response. This agrees with the spectral power change topography shown in Figure 2.1 (a), and previous reports in the literature (Jurkiewicz et al., 2006). The increase in normalized transient burst counts from the pre-movement to the post-movement phase is larger for the contralateral sensor compared with the ipsilateral sensor, suggesting the PMBR is contralateral dominant which also agrees with the spectral power change topography in Figure 2.1 (a), and previous reports of a contralateral dominant PMBR (Jurkiewicz et al., 2006). Furthermore, Figure 2.2 (b) shows the source-level analysis is less sensitive to burst rate changes in the beta band throughout the motor task as compared to the sensor-level analysis methods. Figure 2.2 (c) shows the calculated beta burst rate for each phase of the motor task as well as rest for all three analysis methods across all participants in the contralateral hemisphere. This plot indicates that both sensor-level analysis methods result in similar burst rates despite their unique burst definition thresholds. The source-level analysis gives slightly higher burst rates than the sensor-level analysis methods, and shows less task-related modulation in burst rate compared to sensor-level analyses.

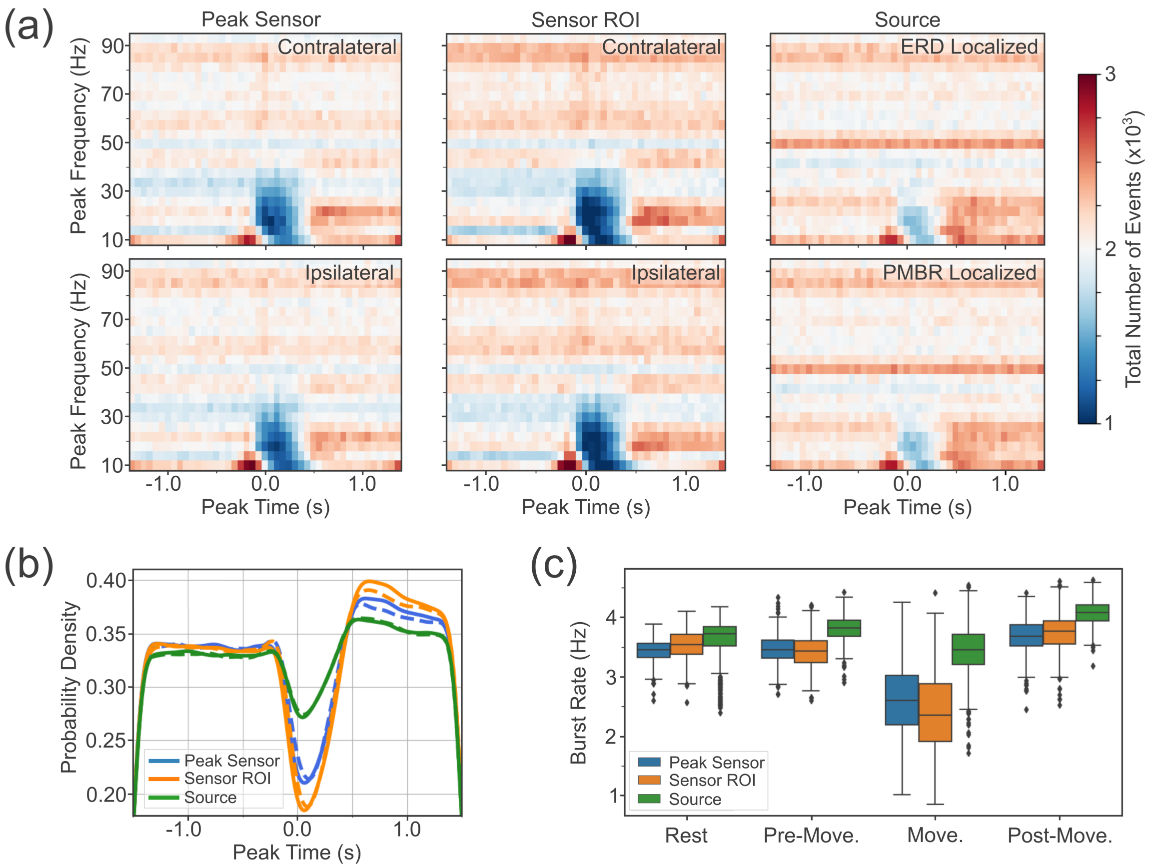

Figure 2.2: (a) Grand-average 2D histograms of contralateral transient burst peak times and peak frequencies for all three analysis methods. (b) Grand-average normalized distribution of transient beta burst peak time showing both contralateral (solid) and ispsilateral (dashed) hemispheres for the sensor-level analysis methods. The solid source-level analysis curve is localized to ERD while the dashed curve is localized to PMBR. (c) Burst rate box plots for all three analysis methods for each phase of the motor task and rest in the contralateral hemisphere

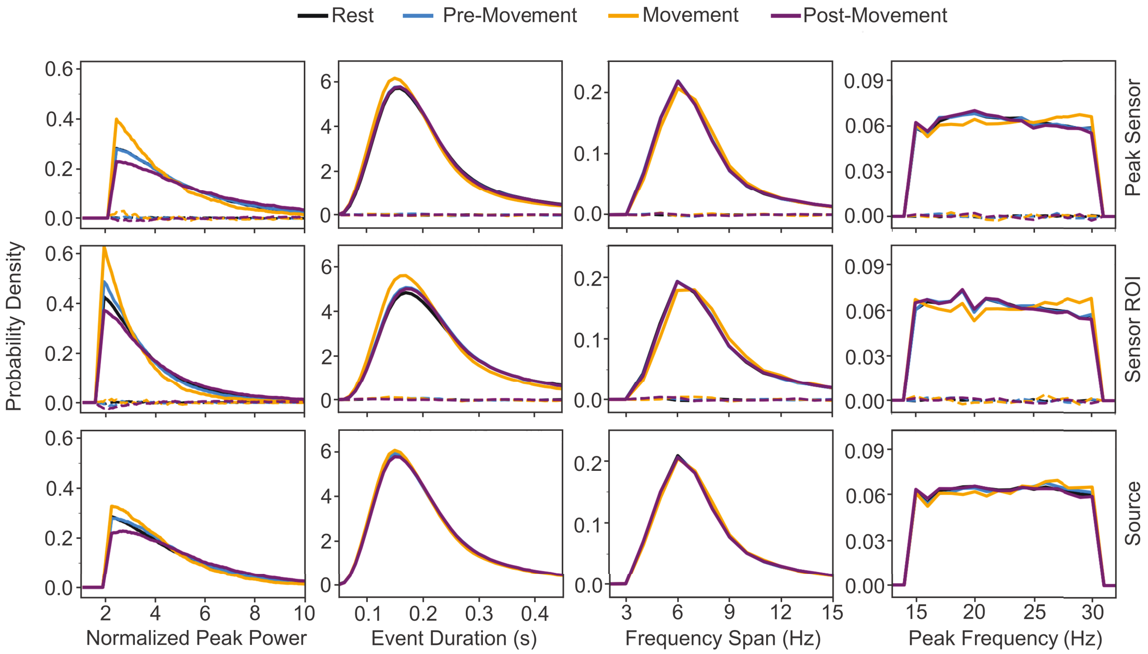

Figure 2.3: Grand-average normalized distributions of transient beta burst normalized peak power, event duration, frequency span, and peak frequency during rest and all phases of the button press response for all three analysis methods. The solid line is the probability density for the contralateral hemisphere whereas the dashed line is the probability density difference between the contralateral and ipsilateral hemispheres.

Figure 2.3 shows the normalized distributions of transient beta burst characteristics over all participants for each phase of the button press response, and for the resting scan, for all three analysis methods. Note that, throughout the paper, source-level burst characteristics are given based on the transient spectral events from the appropriate functional ROI. For example, PMBR burst characteristics are tabulated based on analysis of the PMBR functional ROI. The solid line is the probability density for the contralateral hemisphere whereas the dashed line is the probability density difference between the contralateral and ipsilateral hemispheres. The distribution of normalized power for all three analysis methods suggests that beta bursts in the post-movement phase are shifted to higher power and beta bursts in the movement phase are shifted to lower power relative to rest and pre-movement. This peak power dynamic over the motor task suggests a change in the underlying mechanism and coincides with the changes in burst rate shown in Figure 2.2 (b). The high proportion of low power events for the sensor ROI analysis method is a result of the lower burst definition threshold compared to peak sensor and source analysis methods. The distributions of burst duration, frequency span, and peak frequency are all consistent across all phases of the button press response and all three analysis methods, with a median burst duration and frequency span of 193 ± 5 ms and 6.6 ± 0.1 Hz, respectively (where the uncertainty is the standard deviation of the mean of medians across all phases and methods). Thus, modulation of burst duration, frequency span, or peak frequency are not likely associated with generating the movement-related beta suppression or rebound. Figure 2.3 shows no indication of hemispheric differences in transient burst normalized peak power, event duration, frequency span, or peak frequency.

2.4.2 Age-Related Changes in Burst Characteristics

To focus on a single network, the subsequent data analysis was limited to those spectral bursts occurring contralateral to the movement whose peak frequency fell within the beta frequency band. Figure 2.4 shows age-related changes in beta burst characteristics for each phase of the button press response and for the resting state for the peak sensor analysis method. Age-related changes in beta burst characteristics for the sensor ROI and source analysis methods can be found in the supplementary information (Appendix A). Burst characteristics are fit with either a linear trendline (green) or a quadratic (orange) based on the chi-square comparison as described in section 2.6. Those burst characteristics with a statistically significant relationship with age are highlighted with a star. Table 2.1 shows the model statistics for all plots in Figure 2.4. Tables for model statistics for the sensor ROI and source methods can be found in the supplementary information (Appendix A).

The peak sensor analysis shows the most age-related changes in burst characteristics (13), followed by the sensor ROI analysis (8), and the source level analysis (7). There are no situations in which methods indicate conflicting statistically significant age-related effects. Consistent effects across all three methods (with increasing age) are a decrease in burst-rate during rest, a decrease in peak frequency during rest and pre-movement, and a u-shaped relationship for frequency span at rest. Additionally, consistent effects across the two sensor-level methods are a decrease in peak frequency post-movement, and a u-shaped relationship for frequency span during all task-related phases. Source-level analysis alone reveals a u-shape relationship with age for normalized peak power in the movement interval. Event duration shows no statistically significant trends with age for any interval or method.

Age-related trends for each burst characteristic are consistently modelled as either linear or quadratic effects across intervals and methods. Specifically, burst rate and peak frequency both show linear trends with age, whereas normalized peak power and frequency span both show quadratic trends with age. Normalized peak power tends to higher values in middle age, while frequency span tends to higher values for younger and older participants.

With the exception of the burst rate, the same direction of significant age-related trend are observed for each characteristic across analysis methods, and across the resting state, pre-movement and post-movement intervals. Such agreement suggests that the trends observed are independent of task performance. Interestingly, the increase in pre-movement burst rate with age is opposite to the decrease in resting state burst rate with age (both statistically significant for the peak sensor analysis). This suggests an interaction between age-related changes in burst rate and brain state. The movement interval shows substantially fewer statistically significant age-related trends than the other intervals. For example, the peak sensor analysis shows statistically significant trends in all intervals except movement for burst rate, normalized peak power, and peak frequency. This likely stems from the movement interval having higher variance, compared to other intervals, due to reduced burst rate and shorter interval.

The ERD amplitude increase with age observed in previous work (Bardouille and Bailey, 2019)(Babiloni et al., 2004)(Labyt et al., 2003)(Schmiedt-Fehr et al., 2016)(Toledo et al., 2016) coincides well with the age-related trends in pre-movement burst rate and normalized peak power observed in this work. Specifically, the increasing pre-movement burst rate with age will lead to increased average spectral power in the baseline. In combination with no significant trend in movement burst rate, this equates to an ERD amplitude increase with age. The pre-movement normalized peak power shows a quadratic trend with age, wherein bursts tend towards higher power for older participants compared to younger participants (peak sensor analysis). This increasing trend in pre-movement normalized peak power will also lead to increased average spectral power. In combination with no significant trend in movement normalized peak power, this age-related trend in beta burst characteristics additionally lends itself to an ERD amplitude increase with age.

The decrease in PMBR amplitude with age observed in studies of average spectral power (Bardouille and Bailey, 2019)(Schmiedt-Fehr et al., 2016)(Sallard et al., 2016) coincides directly with the decrease in post-movement burst rate observed in transient beta bursts. Normalized peak power may additionally play a role in the decreased PMBR amplitude, as the quadratic model shows a slightly lower normalized peak power in older participants compared to younger participants. The age-related decrease in PMBR frequency observed based on average spectral power concurs with the age-related decrease in post-movement peak frequency for beta bursts observed here. Overall, the age-related trends observed in the context of studies of spectral power are clearly associated with age-related trends in multiple transient burst characteristics. This relationship between the two approaches to investigating cortical rhythms supports the notion that a transient burst events framework provides a valuable approach for extracting age-related trends in neuromagnetic data.

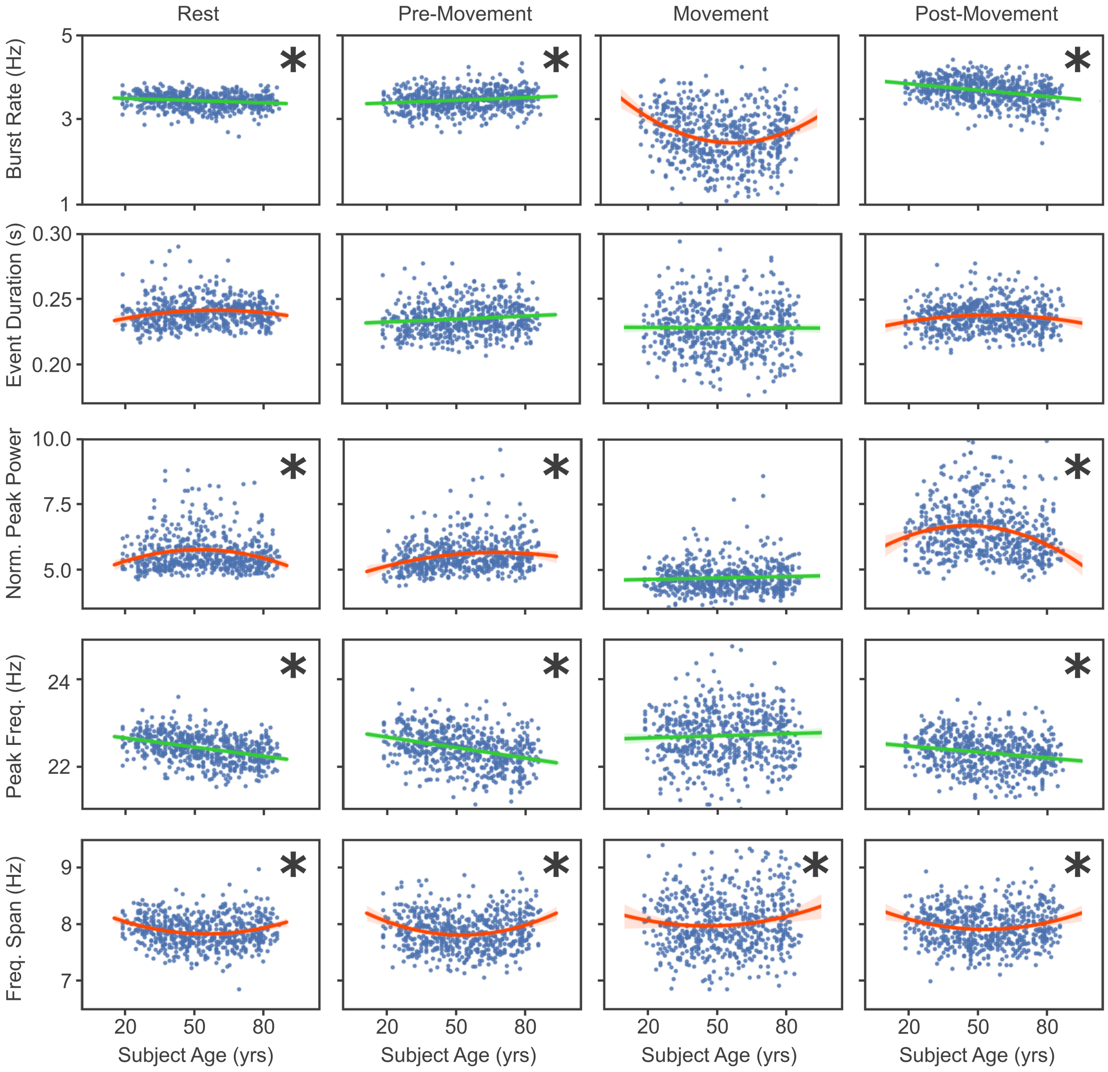

Figure 2.4: Age-related changes in transient burst characteristics for all burst characteristics for each interval of the button press response and for the resting state. Only peak sensor results are shown. Each plot is fit with the model, either linear (green) or quadratic (orange), that was deemed most appropriate via chi-square comparison. Stars indicate statistically relevant age-related trends. The shaded region around the line of best fit represents the 95% confidence interval.

Burst Rate

		Linear Fit $y(x) = a + bx$				Quadratic Fit $y(x) = a + bx + cx^2$					
Phase	F-stat	a [Hz]	b [10^{-3} Hz/y]	p-value	χ^2_{min}	a [Hz]	b [10^{-3} Hz/y]	c [10^{-5} Hz/y^2]	b p-value	c p-value	χ^2_{min}
Rest	2.69	**3.53**	**-1.75**	**1.31E-05**	**1.54**	3.66	-7.15	5.02	6.17E-01	7.04E-01	1.48
Pre-Move.	3.16	**3.35**	**2.05**	**1.38E-04**	**2.66**	3.44	-1.89	3.65	8.97E-01	7.80E-01	2.54
Move.	19.81	2.83	-4.36	1.15E-03	56.24	3.92	-50.01	42.41	5.00E-04	2.70E-03	43.55
Post Move.	2.59	**3.95**	**-4.99**	**4.71E-16**	**2.93**	3.83	0.14	-4.77	9.92E-01	7.19E-01	2.82

Event Duration

		Linear Fit $y(x) = a + bx$				Quadratic Fit $y(x) = a + bx + cx^2$					
Phase	F-stat	a [10^{-1} s]	b [10^{-5} s/y]	p-value	χ^2_{min}	a [10^{-1} s]	b [10^{-5} s/y]	c [10^{-7} s/y^2]	b p-value	c p-value	χ^2_{min}
Rest	11.99	2.38	4.31	6.50E-02	142.74	2.27	47.25	-39.89	9.76E-01	9.76E-01	121.35
Pre-Move.	-0.49	2.31	7.45	4.57E-03	287.87	2.28	18.33	-10.11	9.92E-01	9.92E-01	289.96
Move.	0.61	2.28	-0.65	8.73E-01	607.82	2.32	-17.51	15.66	9.92E-01	9.92E-01	602.43
Post Move.	11.16	2.35	2.11	3.92E-01	178.46	2.25	42.76	-37.77	9.76E-01	9.76E-01	153.31

Normalized Peak Power

		Linear Fit $y(x) = a + bx$				Quadratic Fit $y(x) = a + bx + cx^2$					
Phase	F-stat	a	b [10^{-4} y^{-1}]	p-value	χ^2_{min}	a	b [10^{-2} y^{-1}]	c [10^{-5} y^{-2}]	b p-value	c p-value	χ^2_{min}
Rest	22.86	5.68	-10.66	4.90E-01	1.59	**4.64**	**4.24**	**-40.36**	**2.90E-03**	**2.70E-03**	**1.19**
Pre-Move.	5.52	5.18	64.65	2.40E-06	1.32	**4.62**	**3.00**	**-21.86**	**3.49E-02**	**2.00E-01**	**1.22**
Move.	0.77	4.58	17.83	1.42E-01	3.80	4.64	-0.09	2.51	9.52E-01	8.49E-01	3.75
Post Move.	22.54	6.96	-95.67	1.44E-05	1.72	**5.48**	**5.26**	**-57.80**	**5.00E-04**	**1.00E-05**	**1.29**

Peak Frequency

		Linear Fit $y(x) = a + bx$				Quadratic Fit $y(x) = a + bx + cx^2$					
Phase	F-stat	a [Hz]	b [10^{-3} Hz/y]	p-value	χ^2_{min}	a [Hz]	b [10^{-3} Hz/y]	c [10^{-5} Hz/y^2]	b p-value	c p-value	χ^2_{min}
Rest	0.65	**22.80**	**-6.95**	**4.39E-22**	**0.13**	22.89	-10.76	3.54	4.47E-01	7.87E-01	0.13
Pre-Move.	-0.45	**22.85**	**-8.03**	**2.00E-17**	**0.23**	22.93	-11.70	3.41	4.12E-01	7.95E-01	0.23
Move.	0.12	22.64	1.61	2.47E-01	0.54	22.46	9.13	-6.99	4.97E-01	5.89E-01	0.54
Post Move.	1.40	**22.58**	**-4.73**	**2.81E-07**	**0.23**	22.73	-11.16	5.97	4.35E-01	6.46E-01	0.22

Frequency Span

		Linear Fit $y(x) = a + bx$				Quadratic Fit $y(x) = a + bx + cx^2$					
Phase	F-stat	a [Hz]	b [10^{-4} Hz/y]	p-value	χ^2_{min}	a [Hz]	b [10^{-3} Hz/y]	c [10^{-5} Hz/y^2]	b p-value	c p-value	χ^2_{min}
Rest	46.38	7.92	-6.43	2.78E-01	0.22	**8.34**	**-18.30**	**16.40**	**2.76E-01**	**2.76E-01**	**0.13**
Pre-Move.	27.92	7.86	3.68	6.09E-01	0.43	**8.41**	**-22.89**	**21.60**	**2.00E-01**	**2.00E-01**	**0.30**
Move.	6.41	7.91	20.42	6.26E-02	0.61	**8.26**	**-12.59**	**13.59**	**3.74E-01**	**3.17E-01**	**0.56**
Post Move.	19.41	7.97	-0.82	9.11E-01	0.38	**8.36**	**-16.56**	**15.31**	**2.76E-01**	**2.76E-01**	**0.29**

Table 2.1: Modeling parameters of peak sensor calculated burst characteristics with age. Parameters are given for the linear and quadratic models. Bolded rows indicate statistical significance.

2.5 Discussion

In this paper, we applied the transient spectral event framework proposed by Shin et al. (2017) to a large open-access dataset to characterize beta bursts during a motor task and rest and to investigate how beta burst characteristics change with age. The age-related changes in beta burst characteristics are considered in the context of previous reports of age-related changes in average spectral power in the same population. We found that transient beta burst rate (i.e., number of beta bursts occurring per unit time) shows changes throughout the phases of the button press task that strongly reflect those seen in average spectral power. The normalized peak power of the burst (representative of the burst signal amplitude) shows similar dynamics over the button press task but to a lesser extent than burst rate. Similarly, we found that age-related changes in burst rate correspond well to the age-related increase in beta suppression amplitude and decrease in post-movement beta rebound amplitude previously reported. Again, normalized peak power shows similar age-related trends. In fact, over the investigated age-span (i.e. 18 - 88 years), both burst rate and normalized peak power show an approximate 10% decrease (relative to their median values over the age-span) during the post-movement interval and a 5% increase during the pre-movement interval. Although burst rate and normalized peak power show similar fractional changes over the entire investigated age-span, burst rate shows a direct linear correspondence with age while normalized peak power shows a quadratic tendency, suggesting the age-related changes in normalized peak power have more complex underpinnings. Thus, we suggest that transient beta burst rate is the primary factor driving previously reported age-related changes in induced response amplitudes during a movement task while the peak power of the burst plays a secondary (and perhaps more complex) role. The previously reported decrease in peak frequency of the beta rebound was explained by a decrease in the peak frequency of beta bursts.

It is clear that we can re-evaluate age-related changes in average spectral power as modifications in specific characteristics of transient bursts of activity. We are not suggesting that these characteristics are more sensitive to age than changes in average spectral power. Rather, we posit that the changes in specific burst characteristics have the potential to be more directly associated with changes in the neural circuitry, as compared to the age-related changes in spectral power that represent many bursts as one signal in average. For example, the potential causes for an increase in spectral power include an increase in burst power and burst duration. Beta burst power and duration are likely mediated by different underlying mechanisms (e.g., population size, pathway conductance, thalamic signalling). As such, an analysis that differentiates the burst characteristics that underlie a change in spectral power is valuable. Further work, perhaps in the fields of computational modelling or multi-modal imaging, to determine the anatomical underpinnings of modulations in the beta burst rate and peak frequency will provide insight into how the network generating sensorimotor beta activity changes with age.

In this work, we analyze transient burst characteristics through two sensor-level techniques (peak sensor and sensor ROI) as well as through a source estimation technique (beamformer spatial filter). Source estimation techniques have been validated against expectations for providing accurate estimates of (i) spatial maps of changes in spectral power (e.g, (Jurkiewicz et al., 2006)), (ii) average time courses for regions of interest (e.g., (Cheyne et al., 2006)(Gaetz et al., 2009)), and (iii) average time-frequency response plots (e.g., (Gaetz and Cheyne, 2006)(Bardouille et al., 2010)). To our knowledge this work is the first attempt of validation that the beamformer provides an accurate representation of the characteristics of individual transient events, such as a single beta burst, at the source level. Such validation exists for MEG sensor and equivalent current dipole source estimated data (Shin et al., 2017). Our results show that the source-level analysis attempted here is less sensitive to burst characteristic dynamics throughout motor task performance and the associated age-related trends, as compared with sensor-level analysis. The reduced sensitivity we observed could stem from the spatial specificity of our approach to beamforming transient spectral events. It may be that other beamformer modifications (e.g., regularization, empty room data) and source estimation methods (e.g., dSPM, LORETA) may be better suited to accurately reconstructing transient beta bursts. However, a rigorous comparison of source estimation methods, including simulations and parameter optimisation, is beyond the scope of this thesis. Regardless, the reduced sensitivity to transient bursts at the source level points to a need for a more rigorous analysis of the spatiotemporal dynamics of transient spectral events during movement and at rest, which is beyond the scope of this work.

Despite the reduced sensitivity of the source level approach, the three analysis methods agree as to the appropriate model (i.e. linear or quadratic) to best represent significant age-related trends in this population. Namely, all analysis methods agree that a linear model best represents age-related trends in burst rate and peak frequency (both decrease with age), a quadratic model best represents age-related trends in normalized peak power (n-shaped) and frequency span (u-shaped), and that event duration shows no age-related changes. Different burst characteristics showing diverse age-related trajectories suggests that the characteristics of a given transient beta burst are generated by various underlying neural circuits, and that these neural circuits have unique age-related changes.

One interesting finding is that burst rate showed differing relationships to age for different intervals of MEG data. For example, burst rate decreased with age during rest but increased with age during the pre-movement interval (for peak sensor). It is tempting to think of the pre-movement interval (or pre-stimulus intervals, in general) as equivalent to a long rest interval. However, our results suggest that being engaged in a task can lead to changes in beta burst characteristics from the resting state, and that these changes have a different age-dependency. Specifically, our results indicate that younger participants show a drop in burst rate when transitioning from a rest state to being engaged in a motor task but not moving, while older participants show a jump in burst rate (with the crossover occurring at approximately 50 years old). One could speculate that some fundamental suppression in the signalling of the network underlying beta bursts is occurring when switching from resting to a task state, more so in younger than older participants.

One novel aspect of this work is the discovery of significant high-order (i.e. quadratic) age-related trends in MEG data permissible due to the high number of participants (N = 596) with a nearly uniform age distribution between 18 and 88. Previous reports of age-related effects in smaller populations were limited in investigating only up to first-order effects or to separating participants into ”young” and ”old” groups (Schmiedt-Fehr et al., 2016)(Sallard et al., 2016)(Toledo et al., 2016)(Gaetz et al., 2010)(Gaetz et al., 2020). Modeling age-related trends with a quadratic function suggests the existence of developmental periods of critical differences in the 18-88 age range occurring around the quadratic vertex. With that said, our statistical analysis has forced either a quadratic, linear, or null age-related change for each transient beta burst characteristic. It is possible (perhaps likely) that the natural ageing trajectories of transient beta burst characteristics follow a more complex path. In fact, recent work shows more advanced regression techniques can lead to accurate MEG-based age prediction for the same Cam-CAN dataset (Sabbagh et al., 2019). To further progress efforts towards a better understanding of the healthy ageing human brain, more advanced regression techniques may need to be considered to more accurately reflect how the network generating sensorimotor beta activity changes with age.

The age-related change in the frequency span of beta bursts, which was consistently observed in all intervals for both sensor level analyses, is a novel trend that we did not predict. To our knowledge, this age-related effect has not been previously reported. The quadratic nature of this effect means that it was unlikely to be observed in small sample studies that dichotomize data into young and old groups. A reduction in the frequency span of transient bursts would lead to a reduction in average spectral power. However, the consistency of the age-related trend across intervals may result in this effect being masked in measures of ERD and ERS. At this stage, it is unclear how the age-related modulation of frequency span relates to previously reported age-related changes in the beta rhythm.

Brain-behaviour interactions were not investigated in this work because participants received no imperative instructions with respect to task performance. It would be interesting to investigate beta burst characteristics during task and at rest in datasets where such an imperative exists. Additionally, an investigation of age-related changes in transient bursts in the gamma band would be valuable, although beyond the scope of this thesis. One important limitation of this work is that the TSE framework makes the underlying assumption that transient events are best characterized via transform to frequency space using a Morlet wavelet. Recent work (Jones, 2016) suggests that the electrophysiological correlates of many transient events are not sinusoidal. Thus, the TSE framework can lead to a misrepresentation of burst characteristics. Techniques are required to study transient events in the time domain, rather than using spectral analysis methods that make assumptions about wave shapes. Another weakness is that TSE analysis is performed independently for each channel, such that the mixing of signals between sensors is not accounted for in the analysis. Thus, a given transient event is detected and characterized independently by multiple sensors, which is not ideal for managing the dataset as a whole. Convolutional sparse coding (La Tour et al., 2018) is a promising data-driven technique that decomposes multi-channel MEG data into multiple repeating spatiotemporal patterns, which may have some utility in the detection and characterization of transient events in the time domain across the entire sensor array. Further work is required to characterize transient bursts in neuromagnetic signals in the temporal domain, towards a better understanding of the human brain.

2.6 Acknowledgements

Data collection and sharing for this project was provided by the Cambridge Centre for Ageing and Neuroscience (CamCAN). CamCAN funding was provided by the UK Biotechnology and Biological Sciences Research Council (grant number BB/H008217/1), together with support from the UK Medical Research Council and University of Cambridge, UK.

Chapter 3

Periodic/Aperiodic parameterization of transient oscillations (PAPTO)-Implications for healthy ageing

3.1 Preamble

In Chapter 2 of this thesis, transient events were detected using the same signal power thresholding method applied in Shin et al. (2017), where the threshold was calculated as a multiple of the median power of the timecourse at the peak frequency of the event. The median power spectrum was calculated individually for each participant while the same multiple was used for all participants. While this burst detection approach has led to meaningful neurophysiological insights in Shin et al. (2017) and in Chapter 2 of this thesis, it is important to highlight that normalizing the power threshold by the median power to detect burst events causes the information contained within the median signal power for each participant to be lost (i.e., the information is divided out). Upon completing Chapter 2 of this thesis, I decided to check if the median power itself changed with age out of concern that this loss of information may impact the identified age-related changes in burst characteristics. Figure 3.1 shows the average median power spectrum across the younger (ages 18-53, n=274) and older (ages 53-88, n=286) Cam-CAN participants. The amplitude of the beta frequency peak in the median power spectrum shows an age-related increase. This age-related change and its potential associated neurophysiological insights are lost by amplitude thresholding events based on the median power.

Following the discovery of the age-related increase in the beta frequency peak in the median power spectrum, I searched through the literature to find alternative normalization approaches to the median power spectrum for detecting burst events. I subsequently found the *fooof* (fitting oscillations and one over f) algorithm for parameterizing neural power spectra into aperiodic and periodic components (https://fooof-tools.github.io/fooof/), which has since been published as Donoghue et al. (2020). As shown in Chapter 3, replacing the median power normalization factor with the aperiodic power spectrum for power thresholding transient burst events avoids the loss of information from dividing out the median power while simultaneously disambiguating the transient burst events from the aperiodic activity.

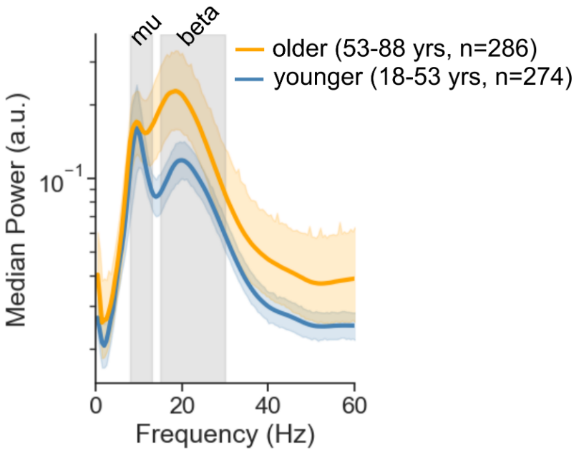

Figure 3.1: Median power spectra show significant age-related changes, particularly around the beta rhythm peak. Median power spectra of all Cam-CAN participants analyzed in this work divided into younger and older age groups. Shaded areas represent 95% C.I. across participants. Information about age-related changes in beta rhythms (shown here) may originate from the transient events themselves but is lost when defining transient events relative to the median power. Note that the median power spectra shown here are scaled by the frequency to eliminate the general 1/f falloff of the curve (for visualization purposes).

In Chapter 3 we use a dynamic statistical parametric mapping (dSPM) technique, a modified minimum norm inverse solution (see section 1.3.1), to localize resting-state time courses to anatomical regions of interest. This differs from the dynamic imaging of coherent sources (DICS) beamformer spatial filter used in Chapter 2. The motivation for this switch arises from recent work from Power and Bardouille (2021) which shows that the dSPM technique gives a more focal localization compared to the DICS beamformer method for beta burst localization.

The text below is published (February, 2022) in *NeuroImage*. *NeuroImage* is a peer-reviewed journal. The reference is provided below.

Brady, B., & Bardouille, T. (2022). Periodic/Aperiodic parameterization of transient oscillations (PAPTO)-Implications for healthy ageing. NeuroImage, 251, 118974. https://doi.org/10.1016/j.neuroimage.2022.118974

See Appendix C for copyright permissions.

3.2 Abstract

Two techniques for analyzing human extracranial neurophysiological signals, namely the periodic/aperiodic parameterization of neural power spectra and the transient events framework of oscillatory activity, have recently emerged in the scientific literature. In this work, we integrate these two analysis perspectives to analyze extracranial neurophysiological signals as a series of transient rhythmic events disambiguated from the background aperiodic activity. We call this novel technique the periodic/aperiodic parametrization of transient oscillations (PAPTO). We demonstrate PAPTO by investigating resting-state sensorimotor magnetoencephalography recordings from the Cambridge Centre for Ageing and Neuroscience cross-sectional study on healthy ageing (n=600, ages 18-88). We show that PAPTO is more sensitive to neocortical transient beta rhythms compared to more conventional transient event detection algorithms and captures more variance in the resting-state occurrence rate of beta events across participants. The improved sensitivity of PAPTO reveals that the beta occurrence rate almost doubles over the adult lifespan which we discuss in terms of thalamocortical beta generation in the somatosensory cortex and the age-related decline of sensory perception.

3.3 Introduction

Healthy ageing is accompanied by a deterioration of sensorimotor performance. The human sensorimotor cortex is responsible for sensory perception and in the planning, control, and execution of voluntary movement (Bardouille et al., 2010; Jones et al., 2010; Parkkonen et al., 2015; Siegel et al., 2008), Sensorimotor function is associated with beta frequency (15-30 Hz) neuroelectrophysiological rhythms that are generated in an inhibitory thalamocortical network. Namely, an increase in beta rhythm strength represents an inhibited state of processing in the network whereas a reduction in beta rhythm strength represents a more activated state of processing (Pfurtscheller and Lopes da Silva, 1999). The performance of a motor task induces a suppression in the sensorimotor beta rhythm amplitude throughout the duration of the task, known as event-related desynchronization (ERD), which is followed by a short (750 ms) rebound in beta rhythm amplitude above baseline levels after completion of the task, known as event-related synchronization (ERS) (Crone et al., 1999; Hari et al., 1997; Pfurtscheller and Aranibar, 1977; Pfurtscheller and Lopes da Silva, 1999; Pfurtscheller et al., 1997). The amplitude and frequency of the beta ERD and ERS change with healthy ageing over the adult lifespan (Babiloni et al., 2004; Bardouille and Bailey, 2019; Christov and Dushanova, 2016; Labyt et al., 2003; Schmiedt-Fehr et al., 2016; Toledo et al., 2016) indicating age-related changes in the neurological processes underlying the thalamocortical neural system.

Sensorimotor cortical rhythms have conventionally been analyzed using spectral averaging techniques in which rhythms appear continuous and sustained in time. Recent work however shows that sensorimotor activity manifests as a series of short-lasting transient events of high-power, frequency-specific oscillatory activity in raw recordings (Jones, 2016; van Ede et al., 2018). These so-called transient events can be defined as episodes of oscillatory activity with peak power above a cutoff value of 6X the median of that recording (Shin et al., 2017) or via a Hidden Markov Modeling (HMM) based technique (Quinn et al., 2019). Local field potential recordings in monkeys reveal that sensorimotor transient beta oscillations (15-30 Hz) emerge from coherent population spiking of cortical pyramidal neurons (Murthy and Fetz, 1992) and work in computational modeling proposes that the positive and negative field deflections within an oscillatory episode arise from competing proximal and distal thalamocortical drives (Sherman et al., 2016). The timing and occurrence rate of these events (i.e., event rate) play an important role in sensory perception as well as the planning and execution of voluntary movement (Brady et al., 2020; Heideman et al., 2020; Little et al., 2019; Seedat et al., 2020; Shin et al., 2017). Primarily, beta events occurring close in time to a sensory stimulus impair the perception of the stimulus (Shin et al., 2017) while events occurring close to a visual cue delay movement initiation (Little et al., 2019). Furthermore, the beta event rate modulations over a motor task mimic the spectral power dynamics associated with beta ERD and ERS (Brady et al., 2020; Little et al., 2019; Seedat et al., 2020). Beta event rate also plays a role in brain disease; namely individuals with Parkinson's disease show robust differences in beta event rate during movement preparation compared to healthy controls (Heideman et al., 2020) while patients with schizophrenia exhibit a lower post-movement beta event rate compared to healthy controls (Gascoyne et al., 2021). At rest, evidence suggests the temporal coincidence of events plays a fundamental role in driving the known electrophysiological beta connectome (Seedat et al., 2020).

Recent work by our group (Brady et al., 2020) analyzes age-related trends in sensorimotor transient beta events characteristics during a motor task (i.e., unilateral button press) and at rest using MEG data from the Cambridge Centre for Ageing and Neuroscience (Cam-CAN) cross-sectional study of healthy ageing (n=596, ages 18-88) (Shafto et al., 2014; Taylor et al., 2017). We found that the peak power of the events showed an n-shaped quadratic ageing trajectory, the peak frequency of the events showed a linear decrease with age, and the frequency span of events showed a u-shaped quadratic ageing trajectory. These trends were found both at rest and during the various phases of the button press. The beta event rate on the other hand showed a slight linear decrease with age at rest but a linear increase with age during the pre-movement interval, suggesting that thalamocortical activity is underpinned by a strong interaction between age and task engagement. As the beta event characteristics show a variety of ageing trajectory functional forms, the results of our recent work (Brady et al., 2020) hint at the unique functional significance of beta event characteristics beyond just the event rate.

The aperiodic behaviour of neuroelectrophysiological signals has not been as widely studied as the rhythmic behaviour. This is primarily due to difficulties in measuring aperiodic signals and thus connecting them to neurological generators (He et al., 2010). The aperiodic activity generally manifests as a $f^{-\chi}$ distribution in the neural power spectral density (PSD), where the power drops off exponentially as a function of frequency, f. The aperiodic exponent, χ, reflects the steepness of the falloff and is typically around a value of one. The steepness of the frequency fall-off has been shown to decrease (i.e., the PSD flattens) with waking compared to sleep (Freeman and Zhai, 2009) and decrease with engagement in a visuomotor task (Podvalny et al., 2015). Furthermore, resting-state ageing studies have shown adults have flatter neural spectra compared to children (He et al., 2019) and older adults have flatter spectra compared to younger adults in the visual cortex, which may facilitate age-related impairments in visual working memory (Voytek et al., 2015). The PSD shape has additionally been found to be a bio-marker for brain disease, including schizophrenia (Racz et al., 2021), Attention deficit hyperactivity disorder (Ostlund et al., 2021; Robertson et al., 2019), as well as Gilles de la Tourette syndrome (Münchau et al., 2021). In addition to the aperiodic exponent χ, the neural PSD is determined by a power offset parameter, b, which reflects the aperiodic baseline power levels. As evidence of its functional significance continues to accumulate in the scientific literature, previous reports labeling the aperiodic activity as a type of "neural noise" are potentially unjustified. In fact, recent work in computational modeling shows that the aperiodic exponent (i.e., the steepness of the frequency fall-off) is associated with the ratio of excitatory (ex. α-amino-3-hydroxy-5-methyl-4-isoxazolepropionic acid, AMPA) to inhibitory (ex. GABA) synaptic currents, where a flatter PSD indicates a higher excitatory to inhibitory ratio (Gao et al., 2017). The aperiodic offset has been shown to correlate with the rate of single-neuron spiking (Manning et al., 2009).

Evidence for the functional significance of rhythmic and aperiodic neuroelectrophysiological activity is now bountiful in the scientific literature. It is thus imperative to separate rhythmic and aperiodic data in signal analysis pipelines to avoid conflating effects and the misinterpretation of the underlying neurophysiological mechanisms. Such a scientific challenge has motivated the recent development of the 'fooof' (fitting oscillations & one over f) algorithm which is designed to parameterize neural PSDs into their rhythmic and aperiodic components (Donoghue et al., 2020). Isolating aperiodic and periodic brain activity using the fooof technique is an effective approach of assessing their functional roles. For instance, (Ouyang et al., 2020) found that dissociating alpha oscillations from 1/f activity revealed a strong relationship between 1/f activity and between-person variability in cognitive speed – an association that is mistaken to originate from alpha oscillations when applying conventional spectral analysis techniques. Isolating aperiodic and periodic brain activity has also shown that simultaneous changes in both components can underpin changes in functional and behavioural processes. For example, (Thuwal et al., 2021) found that both periodic and aperiodic features correlate with visual short-term memory (VSTM) task measures - the aperiodic features being associated with more global changes in information processing and the periodic features reflecting more local changes in selective aspects of the VSTM task. Changes in both the aperiodic and periodic features over the adult lifespan were found to align well with an age-related decline in VSTM task performance. An extension of the fooof parameterization approach to analyze sensorimotor signals may be extremely valuable to elucidate neurophysiological underpinnings of the ageing sensorimotor network. This is challenging however as the fooof algorithm is designed to operate on time-averaged signals while sensorimotor rhythmic activity presents as a series of short-lasting transient events. An integrated approach to parameterize neurophysiological recordings into their transient event and aperiodic components is thus necessary to comprehensively investigate the ageing sensorimotor network.

In this work, we demonstrate the periodic/aperiodic parameterization of transient oscillations (PAPTO). PAPTO is a transient event detection algorithm that intrinsically disambiguates transient event events from the background aperiodic activity. PAPTO works on the basis that the amplitude power threshold for detecting events is calculated as a multiple of the modeled aperiodic activity power spectrum. The objectives of this work are (1) to motivate and validate the PAPTO algorithm, and (2) to use PAPTO to disambiguate adult lifespan changes in the aperiodic activity power spectrum and transient event characteristics. We assess changes across the adult lifespan using resting-state MEG data from the Cam-CAN cross-sectional study of healthy ageing (n=600, ages 18-88). Primarily, we show that PAPTO is more sensitive to neocortical transient beta rhythms compared to beta events detected via a conventional median power amplitude threshold technique. We additionally find that PAPTO captures more variance in the resting-state beta event occurrence rate across participants. The improved sensitivity of PAPTO reveals that the beta occurrence rate almost doubles over the adult lifespan which we discuss in terms of thalamocortical beta generation in the somatosensory cortex and the age-related decline of sensory perception. The valuable new insights gained in our investigation of the ageing human sensorimotor network suggests that PAPTO should be extended to other neurophysiological signals, such as transient events across the entire neuroelectrophysiological frequency spectrum and how they change with age, disease, and task performance.

3.4 Methods

Text from Brady et al. (2020) and Bardouille and Bailey (2019) is adapted in the following sub-sections for clarity and consistency.

3.4.1 Participants & Experimental Paradigm

Six hundred and forty-seven participants had eyes-closed resting-state MEG data recorded for 8 minutes and 40 seconds (first 20 seconds discarded) in Phase 2 of the Cam-CAN examination of healthy cognitive ageing. Participant ages ranged from 18 to 88 years of age, with an equal distribution in age per decile and equal proportions of males and females. Most participants were right hand dominant. Following exclusions (described under sections “MEG pre-processing” and “MRI data analysis & anatomical ROI timecourse estimation”), we report findings from 600 participants (93% of the original 647 datasets).

3.4.2 Data Acquisition

Data were obtained from the Cam-CAN repository (available at http://www.mrc-cbu.cam.ac.uk/datasets/camcan/) (Shafto et al., 2014; Taylor et al., 2017). MEG data were acquired at 1000 Hz with inline band-pass filtering between 0.03 and 330 Hz using a 306-channel Vectorview system with continuous head position monitoring

(Elekta Neuromag, Helsinki, Finland). Digitization of anatomical landmarks (i.e., fiducial points; nasion and left/right preauricular point) as well as additional points on the scalp was also performed for registration of MEG and MRI coordinate systems. Electrooculogram (EOG) and electrocardiogram (ECG) were recorded concurrently. T1-weighted magnetic resonance images were acquired using a 3T Siemens Tim Trio system with a 32-channel head coil

3.4.3 MEG Pre-Processing

Data were pre-processed by the Cam-CAN group using temporal signal space separation to perform environmental noise reduction, reconstruction of missing or corrupted MEG channels, continuous head motion correction, and a transform of each dataset to a common head position (Taulu and Simola, 2006). All subsequent MEG processing was completed in the Python programming environment (v.3.7.3), using the MNE-python library (v.0.20.7) (Gramfort et al., 2014). Raw MEG data were low-pass filtered at 125 Hz and notch filtered at 50 Hz and 100 Hz to remove signals related to power lines. Python code for all subsequent analysis is available at https://github.com/tbardouille/papto_camcan.

Independent component analysis was performed on the task and rest data using the FASTICA algorithm (Delorme et al., 2007; Hutchinson et al., 2002) to remove artifacts using a fully automated process. Briefly, the MEG data were decomposed into independent components (Delorme et al., 2007). Epochs with signals that exceeded 5 pT (magnetometers) or 400 pT/cm2 (gradiometers) were not included when calculating the deconstruction. Following this, components were excluded if the amplitude and phase of the component was similar to that of the EOG or ECG (Dammers et al., 2008). Finally, the MEG sensor data was reconstructed from the remaining components. This process resulted in cleaned MEG data (i.e., channels x time), which were used for anatomical ROI timecourse estimation. To access relatively quiescent MEG data, the rest data were cropped to a single 210 s trial including 105 s prior to and following the midpoint of the resting data.

As described in section 2.4 MRI data analysis & anatomical ROI timecourse estimation, we validated the anatomical ROI timecourse estimation by analyzing beta power over the unilateral button press task (Shafto et al., 2014). The task data was parsed into trials synchronized to each button press, with a duration of 3.4 s and a 1.7 s pre-stimulus interval. Trials were excluded if the button press occurred more than 1 s after the cue (indicating poor task performance) or if the button press occurred within 3 s of the previous button press (which provided insufficient baseline for subsequent analysis). Participants with less than 55 trials after these exclusions were excluded from task analysis (but still included for resting state analysis).

3.4.4 MRI Data Analysis & Anatomical ROI Timecourse Estimation

Each participant's structural MRI was reconstructed using the FreeSurfer recon-all algorithm (Dale et al., 1999; Desikan et al., 2006; Fischl and Dale, 2000; Fischl et al., 2001, 2002, 2004, 1999a,b). The reconstruction process provided a digitization of the cortical surface for source estimation and a boundary element model of the brain to provide more accurate calculation of the forward solution (Hamalainen and Sarvas, 1989). Locations for source estimation were defined covering the entire cortical surface with 5 mm spacing. Finally, each participant's MRI data was registered to the MEG data based on the alignment of anatomical landmarks (i.e., fiducials) in MEG and MRI, and MEG head digitization with the scalp as visualized on the MRI (MNE python coreg, v.0.14) using a semi-automated process (Bardouille and Bailey, 2019). Participants missing MRI data were excluded from further analysis.

Timecourses were estimated at the cortical surface at the centre of mass of 4 sensorimotor gyri (left and right hemispheres, M1 and S1), see 3.2, for each participant using dynamical statistical parametric mapping (dSPM). The statistical parametric maps provide the current density estimates at each cortical location relative to the noise standard deviation at that location (i.e., Z-scores). Individual subject cortices were automatically parcellated using the 'aparc.a2009s' scheme (Destrieux et al., 2010). A total of 2,400 single-trial timecourses (4 ROIs x 600 participants) were generated for analysis in this work. Forward solutions were generated at all source location on each participant's cortical surface using boundary element method and each participant's MRI (see MRI data analysis). Noise covariance matrices were generated for each participant using empty room recordings. A vector source estimate (source current estimate in 3 dimensions) was done at each ROI centre of mass for each participant. We then extracted the component of the current density normal to the cortical surface for analysis. We validated the timecourse estimation by analyzing beta power over a motor task and observed the expected beta suppression and rebound along with the expected laterality of these effects (Figure B.1).

3.4.5 Modeling Aperiodic Neural Power Spectra

Aperiodic activity was modeled via the open source "fitting oscillations & one over f" (fooof) (Donoghue et al., 2020) algorithm (available at https://fooof-tools.github.io/fooof/index.html) for each of the 2,400 anatomical ROI estimated single-trial timecourses. The neural power spectral densities (PSDs) as inputs to the fooof algorithm were generated using Welch's method (4 s segments, 90% overlap) between 0.25 and 80 Hz with 0.25 Hz steps. Neural PSDs were linearly interpolated around 50 Hz to remove notch filter (for powerline noise) effects. The fooof modeling was done across the entire 0.25-80 Hz spectrum with peak width limited between 2 and 10 Hz, minimum peak height of 0.05, a peak threshold of 1.5, and with a maximum of 4 peaks. For efficient processing of the large Cam-CAN dataset, a "fixed" aperiodic mode (knee parameter set to zero for all participants) was used for all model fits. The aperiodic components, namely the aperiodic exponent, χ, and the aperiodic offset, b, for each timecourse, as well as the goodness of fit parameters, namely the absolute error and R^2, were assessed in this work. Variances in the modeled aperiodic parameters for each ROI for each participant were obtained via bootstrapping over 250 randomly selected 12s epochs from each recording. Figure A.2 shows a detailed summary of goodness of fit metrics for the fooof models and the bootstrapping. We observed high quality fits across the Cam-CAN cohort with no differences associated with ROI or age. The mean absolute error was highest for low frequencies (< 3 Hz) due to the $1/f$ nature of the neural power spectra.

3.4.6 Mathematical Basis of PAPTO

From Donoghue et al. (2020), the semi-log PSD as a function of frequency, f, of a single trial timecourse can be modeled as the sum of the aperiodic activity, $L(f)$, and rhythmic activity, $\sum_{n=0}^{N} G_n(f)$, namely:

$$\log PSD(f) = L\,(f) + \sum_{n=0}^{N} G_n(f) \tag{3.1}$$

which represents the power/unit frequency in log10 scale. The aperiodic activity, $L(f)$, is expressed as:

$$L\,(f) = b - \;log_{10}(k + f^{\chi}) \tag{3.2}$$

where b and χ are the aperiodic offset and aperiodic exponent, respectively, and k is a knee parameter. The rhythmic activity, $\sum_{n=0}^{N} G_n(f)$, is a summation of Gaussian peaks present in the PSD. Each Gaussian peak represents one neural rhythm at a particular frequency present in the recording. See Donoghue et al. (2020) for more details on the parameters in equations 3.1 and 3.2.

In this work, we consider that the rhythmic activity is a direct result of the presence of transient events in the timecourse. In other words, we consider that each Gaussian peak in the PSD arises from the accumulation of several transient events all occurring around the same frequency. Since we detect transient events as localized peaks in TFRs with linear power scaling (see section 3.3.7 Detecting transient events), we must consider equation 3.1 in linear space, which simplifies to

$$PSD\,(f) = \frac{10^b}{f^{\chi}} \prod_{n=0}^{N} 10^{G_n} \tag{3.3}$$

upon substituting in equation 3.2 and setting $k = 0$ (i.e., “fixed” aperiodic mode). Equation 3.3 indicates that the power spectrum of a neural recording is the product of the aperiodic activity, $10^b/f^{\chi}$, and rhythmic (transient events) activity, $\prod_{n=0}^{N} 10^{G_n}$. In this work, we propose that the aperiodic activity in linear space, namely:

$$\eta\,(f) = \frac{10^b}{f^{\chi}} \tag{3.4}$$

be used as a baseline power to identify (i.e., amplitude threshold) the occurrence of transient events in single-trial recordings. Utilizing $n\,(f)$ as a baseline power intrinsically disambiguates transient events from the aperiodic activity while effectively standardizing transient event power across participants.

3.4.7 Detecting Transient Events

The PAPTO technique (https://github.com/tbardouille/papto) is a modified amplitude thresholding approach of detecting transient events. We developed PAPTO as an adaptation of the event detection technique established by Shin et al. (2017) https://github.com/hs13/BetaEvents, herein referred to as the "Shin method". Note that several of the scripts for PAPTO are direct adaptations from the Shin method.

In PAPTO, transient events are defined as short-lasting local maxima of signal power in single-trial recordings in time-frequency representation (TFR). TFRs, denoted as $E(t, f)$, are calculated via Morlet wavelet convolution as described previously (Tallon-Baudry et al., 1997). The Morlet wavelet's, $w(t, f_0)$, used in PAPTO are of the form

$$w(t, f_0) = A \exp\left(-t^2/2\sigma_t^2\right) \exp\left(2i\pi f_0 t\right) \tag{3.5}$$

where f_0 denotes the central frequency and $A = \left(2/\sigma_t\sqrt{\pi}\right)^{1/2}$. Here, $\sigma_t = m/2\pi f_0$ represents the standard deviation of the Morlet wavelet envelope in the time domain, scaled by the width parameter, m, which we set to 10 (i.e., number of Morlet wavelet cycles). For each of the 2,400 single trial recordings, $E(t, f)$ is normalized by the fooof modeled aperiodic activity power spectrum, $\eta(f)$, (i.e., from equation 3.4) at each time-frequency bin to generate a new TFR, $E_\eta(t, f)$. Transient events are then defined as local maxima in each $E_\eta(t, f)$ with peak power that exceeds a threshold value defined as a multiple of $\eta(f)$. PAPTO differs from the Shin method in that the Shin method defines the amplitude power threshold as a multiple of the median power spectrum, $\widetilde{E}(f)$, of $E(t, f)$. Herein, transient events detected via PAPTO will be referred to as "PAPTO events" and transient events detected via the Shin method will be referred to as "med-norm events".

The amplitude threshold for defining both PAPTO and med-norm events was calculated based on the correspondence of thresholded data to the TFR as described by Shin et al. (2017). TFRs were first cropped to the beta band and epoched into 2s segments. The percentage of TFR pixels above the power cutoff value for various cutoff values (defined as multiples of $\eta(f)$ for PAPTO and multiples of $\widetilde{E}(f)$ for med-norm) was calculated for each epoch. The Pearson correlation coefficient between the average beta power and percent pixels across time (i.e., across epochs) was then calculated for each cutoff value. This resulted in one correlation coefficient for each threshold for each timecourse. Correlations at each threshold were then averaged over all participants for each anatomical ROI. The power cutoff corresponding to the peak of the correlation coefficient was then used as the amplitude threshold value, as shown in Figure B.3. Following this procedure, we found that an amplitude threshold of $8 \times n(f)$ for PAPTO events and $5 \times \widetilde{E}(f)$ for med-norm events. Note that the same procedure was done in the mu band and found the same thresholds (see Figure B.3).

3.4.8 Characterizing and Classifying Transient Events

All transient events were then characterized in the time-frequency domain. The time and frequency coordinates of the local maxima in the single-trial TFRs represent the peak time and peak frequency of the events, respectively. Note that beta events refer to any event with peak frequency between 15 and 30 Hz. The event duration and frequency span were calculated as the full-width at half maximum (FWHM) of the local maxima along the time and frequency dimension, respectively. The cycles per event were calculated as the peak frequency multiplied by the event duration for a given event. The occurence rate was calculated as the number of events that occur within 210 s timecourse by 210 s. All example event characteristics values given in-text are determined from left hemisphere S1 localized data, unless otherwise stated.

All PAPTO and med-norm events were classified as either 1 unique to PAPTO, 2 unique to med-norm, or 3 detected by both methods. If the peak time and peak frequency of a med-norm event fell within the event duration and frequency span of a PAPTO event, both events were considered group 3. PAPTO events that were not classified as group 3 were classified as group 1. Likewise, med-norm events that were not classified as group 3 were classified as group 2.

Transient beta event waveforms were generated following an event-triggered time-course averaging process described in detail by Sherman et al. (2016). Briefly, the peak time for each transient beta event detected in a single-trial TFR was used to trigger epoching (2000 ms width centred on the peak time) in the associated anatomical ROI timecourse. The resulting time-domain epoch for each event was then bandpass filtered to the peak frequency of the event +/- 1 Hz and then centered in time to the nearest negative field deflection to the peak time. One average epoch, or beta event waveform, was generated for each participant/ROI by averaging all event-triggered epochs over the 210 s recoding, based on the corrected peak time but without the +/- 1 Hz band-pass filter. The resulting participant/ROI average waveforms were characterized by their peak times (relative to the central negative deflection centered at t = 0 s) and peak amplitudes. Variance in waveform characteristics were generated via a bootstrapping technique involving 25 iterations of generating and characterising waveforms using a randomly selected subset of $\frac{1}{2}$ of the total events in each participant/ROI timecourse.

3.4.9 Statistical Analysis of Age-Related Effects

Regression was used to reveal statistically significant relationships between age and aperiodic activity parameters as well as between age and beta event characteristics. Regression analysis was performed on the average characteristic/parameter per participant/ROI with participant age as the independent variable. Within subject variance of parameters (calculated as indicated above) was accounted for in the regression models by subject-specific weighting factors (higher variance leads to lower weighting). Both linear and quadratic models were investigated for each characteristic/parameter. The most appropriate model, i.e., linear or quadratic, was selected by comparing chi-square values via an F-test (quadratic model was selected if F-stat > 6.6, corresponding to a 99% confidence level). Statistically significant non-zero age-related trends were determined if the model fit had a Bonferroni adjusted (for multiple comparisons) p-value < 0.05.

3.5 Results

3.5.1 Aperiodic Activity in S1 and M1 and Associated Age-Related Changes

We utilized the fooof algorithm (Donoghue et al., 2020) to parameterize each neural PSD (one for each of the 2400 timecourses) into its periodic and aperiodic components. Figure 3.2 b shows fooof fitted PSDs generated from each anatomical ROI for one example Cam-CAN participant. Each PSD shows periodic activity in the mu and beta bands sitting amongst the $1/f$-like aperiodic activity spectrum, $\eta(f)$. The fooof algorithm generated accurate models for all PSDs in Cam-CAN cohort (grand average median r-squared: 0.96, 25th - 75th percentile: [0.94, 0.98]). See Figure B.2 for a comprehensive analysis of the goodness of fit of the fooof models. The aperiodic activity spectrum, $\eta(f)$, for a single-trial recording is completely described via the aperiodic exponent, χ, and the aperiodic offset, b (see Methods section equation 3.4). Our analysis (Figure 3.2 c, left) reveals a significantly higher aperiodic exponent in S1 compared to M1 and in the right hemisphere compared to the left (paired t-test across participants, $p < 0.05$, Bonferroni corrected for multiple comparisons). We additionally found (Figure 3.2 c, right) that S1 has a significantly lower offset compared to M1 (paired t-test across participants, $p < 0.05$, Bonferroni corrected for multiple comparisons), but no hemispheric differences were found. These regional differences are nicely visualized in the grand-average aperiodic activity spectra for each anatomical ROI (Figure 3.2 d). Analyzing the fitted aperiodic activity parameters as a function of participant age reveals age-related changes in the aperiodic activity spectrum. We found that the aperiodic exponent in S1 shows a significant u-shaped quadratic ageing trajectory ($p < 0.05$, Bonferroni corrected for multiple comparisons) with the flattest aperiodic activity spectral density occurring at 60 years for both hemispheres (Figure 3.2 e, left). No significant age-related changes were found for the aperiodic exponent in M1. Conversely, the aperiodic offset shows a significant age-related increase in M1 (both hemispheres) but no significant changes in S1 (Figure 3.2 e, right). See Table 3.1 for model fit parameters.

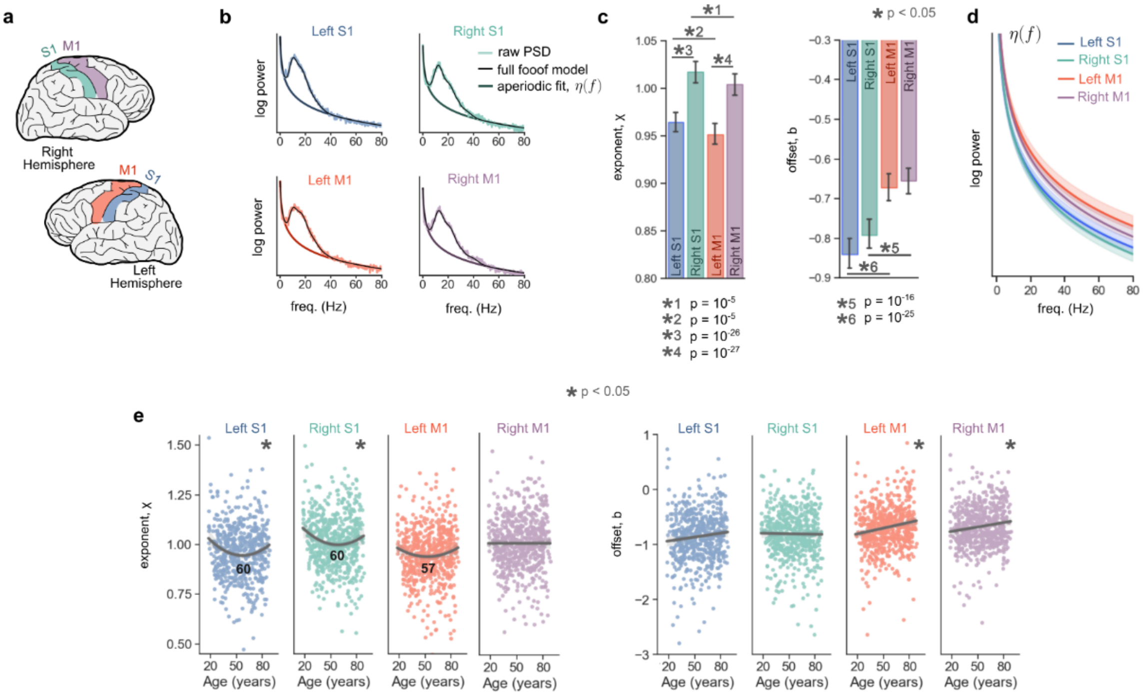

Figure 3.2: Aperiodic activity analysis of the Cam-CAN dataset reveals variations across ROIs and healthy ageing trajectories. Application of the fooof algorithm to the Cam-CAN dataset resting-state scans. (a) timecourses localized to four sensorimotor ROIs (S1 and M1, left and right hemispheres) for each participant in the Cam-CAN dataset. (b) example fooof modeling of PSDs localized to each anatomical ROI for one example participant. Example participant chosen based on maximum correlation to grand-average PSD (for left S1). (c) bar plots showing the average aperiodic activity parameters for each ROI across the Cam-CAN cohort reveal several significant differences between the four sensorimotor ROIs (paired t-tests across participants). (d), visual depiction of the average aperiodic activity spectrum for each ROI. Shaded areas represent 95 % C.I. across participants. (e) scatterplots showing age-related changes in aperiodic activity parameters for each sensorimotor ROI. Stars indicate statistical significance. All p-values Bonferroni corrected for multiple comparisons.

						polynomial fit			
region	hemi.	parameter	F-stat	Model	p-value	quadratic term [10^{-5} y^{-2}]	linear term [10^{-3} y^{-1}]	intercept	extremum age [y]
S1	left	exponent	8.5	quadratic	**0.005**	4.48	-5.33	1.10	60
	right		13.8	quadratic	**0.010**	5.51	-6.57	1.18	60
M1	left		8.6	quadratic	0.531	4.39	-4.99	1.07	57
	right		5.3	linear	0.990	-	-0.29	1.01	-
S1	left	offset	2.1	linear	0.186	-	1.18	-0.95	-
	right		1.6	linear	6.150	-	-1.16	-0.78	-
M1	left		3.5	linear	**0.001**	-	1.91	-0.82	-
	right		1.6	linear	**0.023**	-	2.40	-0.83	-

Table 3.1: Modeling age-related changes of resting-state sensorimotor aperiodic activity parameters. Ageing model fit parameters for fitted aperiodic activity spectra. Model selection (linear vs quadratic) based on an F-test for each characteristic (see section 3.4.9 for more details). Bolded values indicate statistically significant ($p < 0.05$) non-zero age related changes. All p-values Bonferroni corrected for multiple comparisons.

3.5.2 Motivating and Validating PAPTO

Here we show that basing the transient event amplitude threshold on the median power spectrum, $\widetilde{E}(f)$, (i.e., med-norm events) leads to a significant loss of information which can be avoided via PAPTO. Figure 3.3 a shows the raw (mean) PSD, $\widetilde{E}(f)$, and the fooof modeled aperiodic activity, $\eta(f)$, for 6 representative example participants from the Cam-CAN cohort. All data shown here is generated from time-courses localized to the left hemisphere S1. All example raw PSDs shown here, apart from ex. subj03, demonstrate distinct periodic neural activity in the mu and beta frequency ranges. The spectral features present in the raw PSDs are also present in $\widetilde{E}(f)$ with only slightly reduced amplitude for each participant. Amplitude thresholding transient events using $\widetilde{E}(f)$ is thus expected to result in a loss of information about the periodic signal. PAPTO is designed to avoid this loss of information by amplitude thresholding transient event detection using $\eta(f)$. The advantage of PAPTO is depicted in Figure 3.3 b, which shows 20 s spectrogram snippets (taken from the middle of the rest recording) for each example participant shown in Figure 3.3 a. The spectrograms are each shown [1] in raw form, [2] normalized by $\eta(f)$ (i.e., used to identify PAPTO events), and [3] normalized by $\widetilde{E}(f)$ (i.e., used to identify med-norm events). The PSDs generated (from the entire 210 s rest recording) from [1]-[3] are shown on the right. By amplitude thresholding events as a multiple of $\widetilde{E}(f)$, the med-norm technique results in a substantial loss of oscillatory signal components (compare $\mathrm{PSD}_{[3]}$ and $\mathrm{PSD}_{[1]}$). On the other hand, by amplitude thresholding transient events as a multiple of $\eta(f)$, PAPTO preserves the periodic components of the raw signal while still removing the aperiodic components (compare $\mathrm{PSD}_{[3]}$ and $\mathrm{PSD}_{[2]}$).

We then detected both PAPTO transient events and med-norm transient events from the resting state data using an amplitude-thresholding approach. We applied a technique reported by Shin et al. (2017) to determine the amplitude threshold for med-norm transient events as a multiple of $\widetilde{E}(f)$. We extended the Shin et al. (2017) technique to PAPTO transient events to determine the amplitude threshold as a multiple of $\eta(f)$. See section 3.4.7 for details on the threshold selection process. We found an amplitude threshold of $5 \times \widetilde{E}(f)$ for the med-norm events and $8 \times \eta(f)$ for PAPTO events was suitable across all participants for all four anatomical ROIs and for both mu and beta events (see Figure B.3). For the remainder of this work, we present a parallel analysis of PAPTO and med-norm resting state transient events while calling attention to their differences and highlighting the advantages of the PAPTO technique.

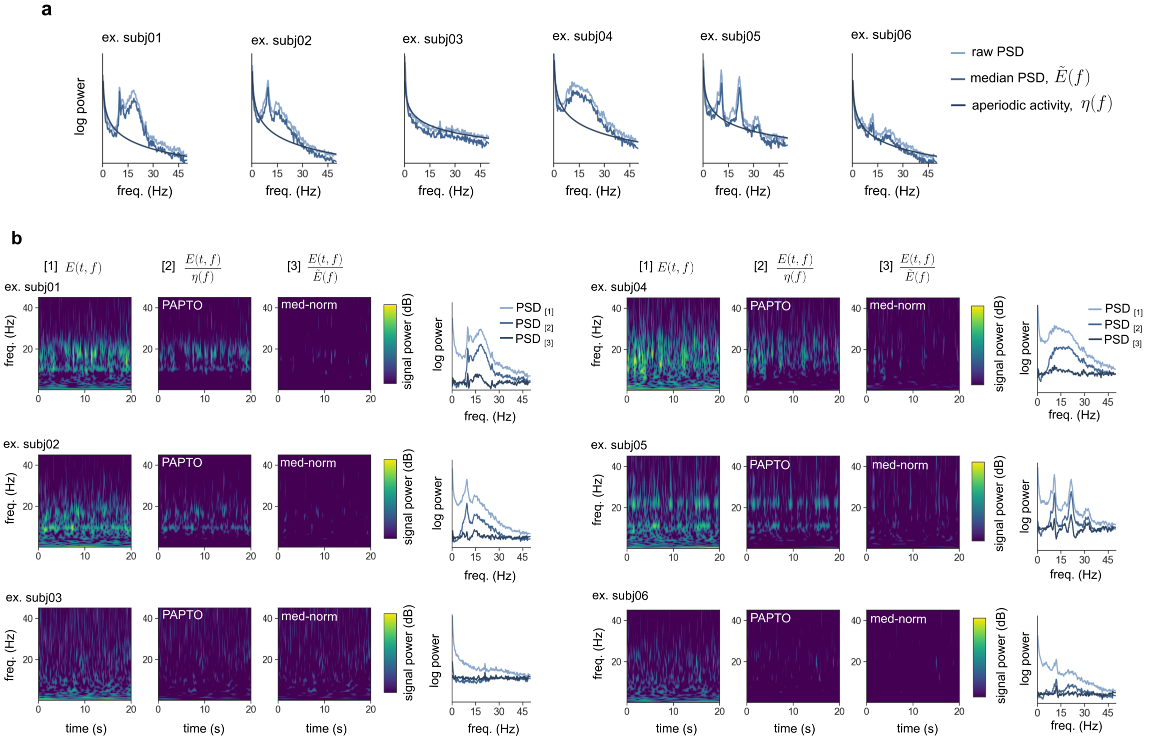

Figure 3.3: fooof modeled aperiodic activity as an alternative to the median for amplitude thresholding transient events. Thresholding transient event detection via the median power leads to a significant loss of information. (a) raw (mean) PSD, median PSD, and modeled aperiodic activity over the entire 210 s resting state recording for 6 representative example participants taken from the Cam-CAN dataset (plots shown at the same y-scale). (b) time-frequency representation (20 s widows) of the resting-state recordings for each example participant. Each TFR is shown in [1] raw form, [2] normalized by the fooof modeled aperiodic activity, and [3] normalized by the median power. Power shown (in dB) is calculated as 10*log10 of the raw power. PSDs corresponding to each TFR are shown on the right. All curves are y-shifted so they align at 80 Hz. Note all data shown here is localized to the left hemisphere S1.

We first examine the temporal waveforms of both med-norm and PAPTO events to show that PAPTO is more sensitive to stereotypical beta transient events. Figure 3.4 a (top panels) shows the grand-average peak-time triggered waveforms (see section 3.4.8) for all events detected in Left S1 across the Cam-CAN cohort. Both PAPTO and med-norm event waveforms show a stereotypical waveform lasting about 4-5 oscillatory cycles centered by a large amplitude negative field deflection and symmetric about t = 0 ms. These waveform temporal profiles are consistent with those found by Sherman et al. (2016), where the positive and negative modulations are described as a consequence of competing proximal and distal current flow, respectively, along the apical dendrites of neocortical pyramidal neurons. The small 95% C.I. intervals indicate low inter-subject variability in waveform profile. The average occurrence rate of these events across participants, as indicated above the waveform (± denotes 95% C.I.), shows that PAPTO detects about 25-30% more events than the med-norm method (differences in occurrence rate between the methods are further explored in Figure 3.5). To elucidate the differences between PAPTO and med-norm transient events waveforms, we then categorized each detected event as either being unique to med-norm, unique to PAPTO, or detected by both med-norm and PAPTO (see section 3.4.8). Figure 3.4 a (bottom panels) shows the temporal waveforms of the events in each category. Primarily, as expected, events detected by both methods show stereotypical waveforms with large amplitudes. These high-power events are supra threshold for both techniques and make up most of all events detected for each technique (68% of all PAPTO events and 88% of all med-norm events). These waveforms thus dominate the average waveform for each technique causing no major differences between the average PAPTO and average med-norm waveforms (top panels). The unique to PAPTO events (32% of all PAPTO events) are low-amplitude events with stereotypical waveforms. These events, which occur at a rate of 0.50 ± 0.04 Hz, are picked up by PAPTO but missed by the med-norm method. The unique to med-norm events (12% of all med-norm events) show an atypical waveform compared to prototypical transient beta events. These atypical temporal signatures, which occur at a rate of 0.15 ± 0.02 Hz, are excluded by the PAPTO technique. PAPTO designates these atypical peaks in signal power as sub-threshold transient modulations in aperiodic activity. PAPTO is therefore more sensitive to stereotypical beta transient events and less sensitive to atypical beta transients compared to the conventional med-norm technique.

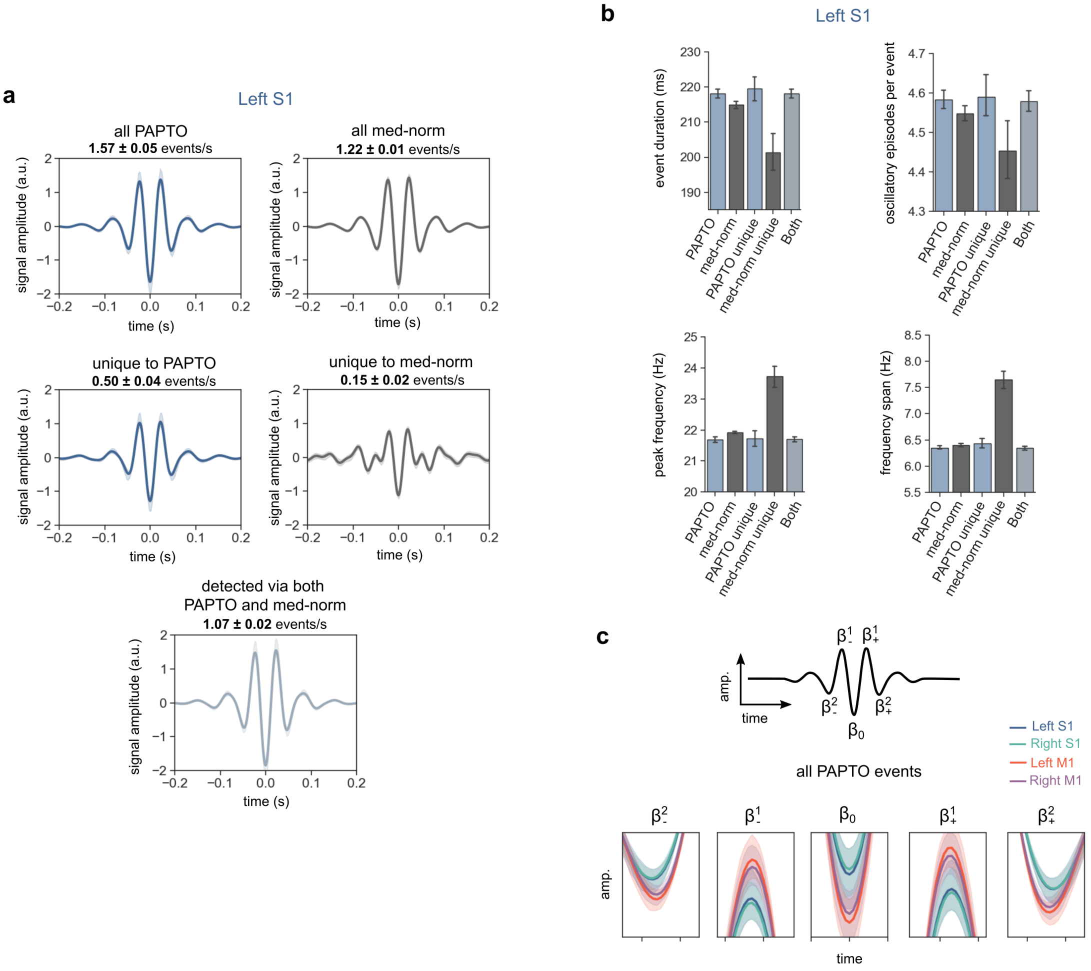

Figure 3.4: PAPTO is sensitive to neocortical beta oscillations. (a) transient event waveforms average over all participants (shaded areas represent 95% C.I.) for all PAPTO events (top left) and med-norm events (top right). All events were then divided into three categories, namely unique to PAPTO (middle left), unique to med-norm (middle right), and detected by both methods (bottom). The average occurrence rate of each category of beta event is shown. Uncertainties represent 95% C.I. (b) average spectral characteristics for each category of beta event. Error bars represent 95% C.I. across participants. Note that all data shown in (a) and (b) were localized to left hemisphere S1. Other anatomical ROIs show similar patterns. (c) average beta event waveform across all participants for each anatomical ROI shows that M1 events are higher amplitude than S1 (95% C.I.)

Figure 3.4 b explores the time-frequency domain characteristics of the transient beta events and further highlights the atypical nature of med-norm only events. Primarily, PAPTO beta events detected in left hemisphere S1 have an average duration of 218 ± 2 ms (mean ± 95% C.I.), an average of 4.58 ± 0.02 oscillatory episodes per event, an average event peak frequency of 21.7 ± 0.1 Hz, and an average frequency span of 6.35 ± 0.05 Hz. Average characteristics over all PAPTO events, all med-norm events, PAPTO-only events, and all events detected by both methods are all similar with only marginal differences. The events unique to the med-norm technique however show a substantially lower event duration and oscillatory episodes per event along with substantially higher peak frequency and frequency span. These atypical characteristics further emphasize that these events should not be considered in parallel with the more stereotypical transient events. The characteristic differences between the 5 event categories shown in Figure 3.4 a and 3.4 b are similar for all anatomical ROIs and thus results from the other anatomical ROIs are not shown. The key difference between anatomical ROIs, as shown in Figure 3.4 c, is the amplitude of the beta waveform, namely events detected in M1 have higher waveform amplitude for both PAPTO (shown) and med-norm (not shown) events.

Recent findings relating sensorimotor beta event occurrence rate dynamics with motor task performance (Brady et al., 2020; Heideman et al., 2020; Little et al., 2019; Seedat et al., 2020; Shin et al., 2017) suggest that beta event occurrence rate plays a fundamental role in sensorimotor processing. Here, we show that PAPTO events better capture the inter-subject variability in cortical beta rhythmic activity compared to med-norm events. Figure 3.5 a shows the beta event occurrence rate across all Cam-CAN participants for each region of interest for med-norm beta events (left) and PAPTO beta events (right). There is a narrow distribution of med-norm beta event occurrence rates across participants, centered around 1.22 Hz with no significant differences between ROIs. PAPTO beta events show a much higher variance in occurrence rates across participants and generally higher occurrence rates (average around 1.52 – 1.64 Hz) than med-norm events. PAPTO additionally reveals significant differences in the average occurrence rates between ROIs, namely the left hemisphere showing higher rates than the right hemisphere and S1 showing higher rates than M1. The increased inter-subject variance for PAPTO is further investigated in Figure3.5 b, where occurrence rate is plotted against average beta power for med-norm events and PAPTO events for each sensorimotor ROI (note varying x-scale). The increased variance seen in Figure 3.5 a correlates (compare Pearson correlation coefficients, r)

with inter-subject variance in average spectral power. Given the functional significance of beta event occurrence rate, the significantly improved sensitivity of PAPTO to inter-subject variances in neuroelectrophysiological rhythmic activity is a powerful discovery which highlights the benefits of re-defining transient events via PAPTO.

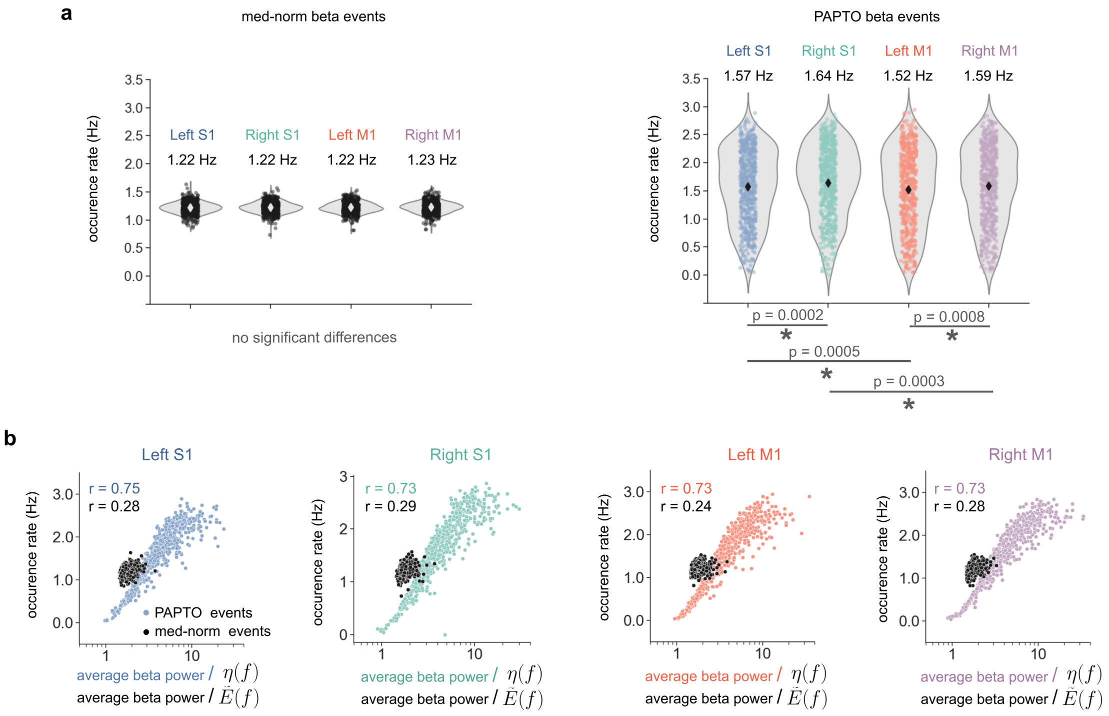

Figure 3.5: PAPTO transient beta occurrence rate is correlated with average beta power. (a) beta event occurrence rate for med-norm (left) and PAPTO (right) beta events for each sensorimotor ROI. Each point corresponds to the average occurrence rate for one participant and the black diamond represents the average (also indicated above) across participants. PAPTO finds significant event rate differences between sensorimotor regions (p-values shown are Bonferroni corrected for multiple comparisons). (b) correlations between occurrence rate and average beta power for med-norm and PAPTO events for each sensorimotor ROI. Each point corresponds to one participant. Pearson correlation coefficients indicated by ‘r’.

An analysis of transient events in the frequency domain reveals that the frequency distribution of PAPTO events closely aligns with the generally accepted spectral power distribution across canonical frequency bands. Single-participant transient events spectra (events binned according to their central frequencies) in Figure 3.6 a (top row) are used to demonstrate where transient events were detected in the frequency domain. The same 6 example participants in Figure 3.3 are shown here.

PAPTO detects a high density of events in the mu and beta frequency bands which manifest as high event counts around 10 Hz and 20 Hz in each event spectrum. Note that the relatively little periodic activity of ex. subj03 and subj06 (see Figure 3.3) compared to the other example subjects is reflected in the low PAPTO event count for these two subjects in Figure 3.6 a. Med-norm events predictably show a more spread-out distribution of events in the frequency domain. The median PSDs shown in Figure 3.3 a indicated the med-norm event detection technique will bias event detection away from the mu and beta bands due to an elevated detection threshold stemming from the high signal power in these bands. To assess the degree to which an individual's transient event spectrum represents their sensorimotor activity, we calculated the Pearson correlation coefficient (r) between each individual's mean PSD (Figure 3.6 a, bottom row) and their transient event spectra. We found that the PAPTO spectrum more closely resembles the mean power spectrum, as compared to the med-norm spectrum for each example participant. We then assessed the correlations for all participants in the Cam-CAN dataset (Figure 3.6 b) and found a significantly higher correlation for the PAPTO events compared to the med-norm events across sensorimotor ROIs. These results suggests that PAPTO provides a more accurate depiction of the transient activity in the frequency domain.

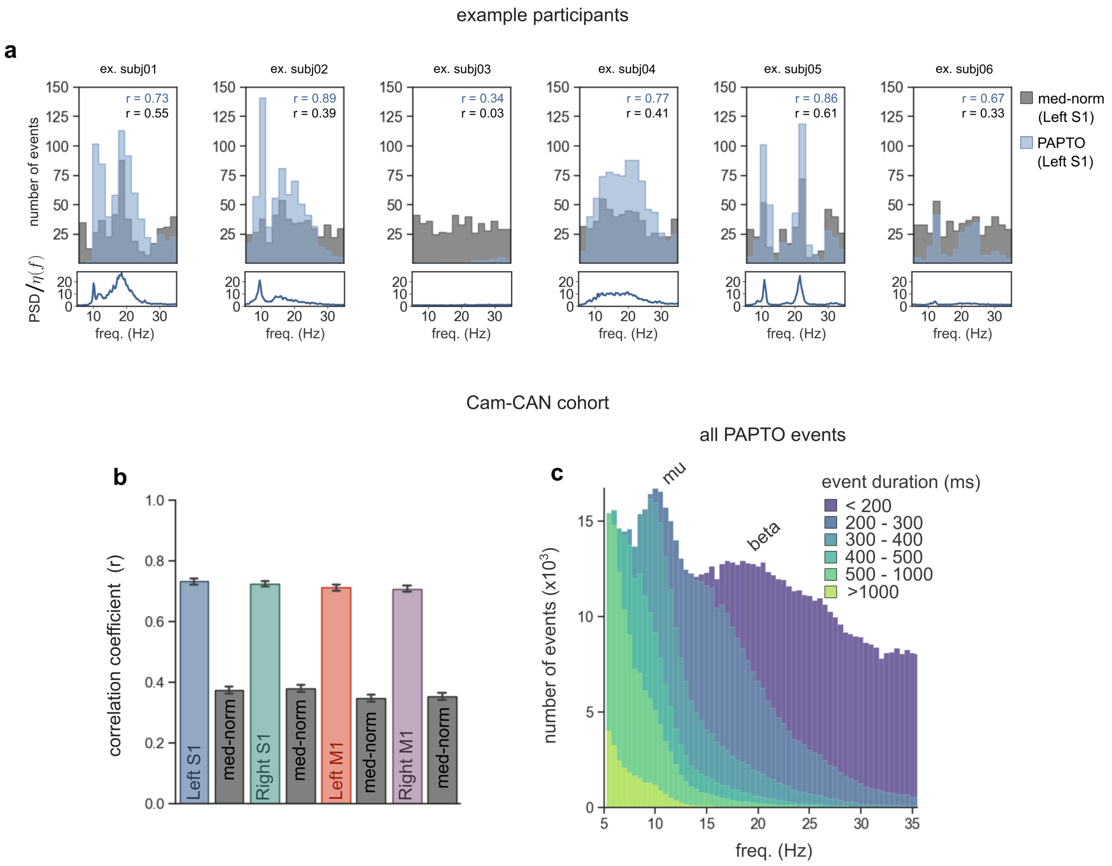

Figure 3.6: PAPTO highlights transient events in canonical frequency bands. (a) transient event spectra (top) showing both med-norm events (grey) and PAPTO events (blue) for the six example participants shown in Figure 3.3. bin width = 2 Hz. Mean power spectra (bottom) shown for visual comparison. Correlation coefficient between mean power spectra and transient events spectra for both event types are indicated. (b) bar plots showing correlation coefficient between mean power spectra and transient event spectra for both med-norm events and PAPTO events across all participants. Each anatomical ROI shows a significantly higher correlation for PAPTO events. (c) overall PAPTO event spectrogram (across all 600 Cam-CAN participants, bin width = 0.5 Hz) shown as a cumulative histogram indicating event duration by color.

Figure 3.6 c shows the PAPTO event spectrum (5-35 Hz) for all events detected in left hemisphere S1 compiled over the Cam-CAN cohort. This event spectrum is shown as a cumulative histogram where the color of each bar represents the event duration. This histogram shows distinct mu and beta bands with a higher likelihood of events (i.e., events per frequency bin) in mu compared to beta. In terms of event duration, there is a sharp transition to longer duration events as event peak frequency decreases. Namely, beta (15-30 Hz) events show an average duration of 218 ± 2 ms while mu events (8-15 Hz) have a substantially longer average duration of 452 ± 6 ms. When looking at the number of oscillatory cycles sustained per event however, mu events only slightly out-last beta events, that is 4.91 ± 0.05 cycles per event for mu events and 4.58 ± 0.02 cycles per event for beta events. The longer duration and more cycles of mu events compared to beta events may underlie the previously observed stronger lagged coherence of beta rhythms compared to mu rhythms (Fransen et al., 2015).

3.5.3 Resting-State Sensorimotor Beta Events Show Significant Changes with Healthy Human Ageing

Basing the amplitude threshold on $\widetilde{E}(f)$ poses a particular challenge when investigating age-related changes in transient event characteristics due the median power spectrum itself changing with age (Figure 3.1). The age-related change in median power is a blend of the age-related changes in the aperiodic activity spectrum (Figure 3.2 e) with changes in the transient events themselves. PAPTO disambiguates the periodic and aperiodic ageing effects without losing information about age-related changes in transient event characteristics. We thus hypothesize that PAPTO events show novel age-related trends not observed in in med-norm events. Figure 3.7 and Table 3.2 highlight age-related changes in left hemisphere S1 transient beta event characteristics. Age-related changes in event characteristics for the other anatomical ROIs can be found in Figures S5-7 and Tables S1-3.

The PAPTO beta event occurrence rate shows a significant increase with age, from about 1.0 Hz to about 1.75 Hz across the age-range (18-88) of the Cam-CAN cohort (Figure 6a). This trend is consistent across sensorimotor ROIs (Figures S5-S7). This result is in support of our hypothesis as only marginal age-related changes are found in med-norm events across sensorimotor ROIs. Our ageing analysis suggest this age-related change is best modeled with a quadratic function with a peak around 70 years old, indicating that the occurrence rate increases most rapidly in early adulthood before settling out towards middle to older ages. Considering the functional significance of the beta event occurrence rate in the sensorimotor cortices, this substantial age-related increase in occurrence rate is an important outcome realized only via the sensitivity of PAPTO technique.

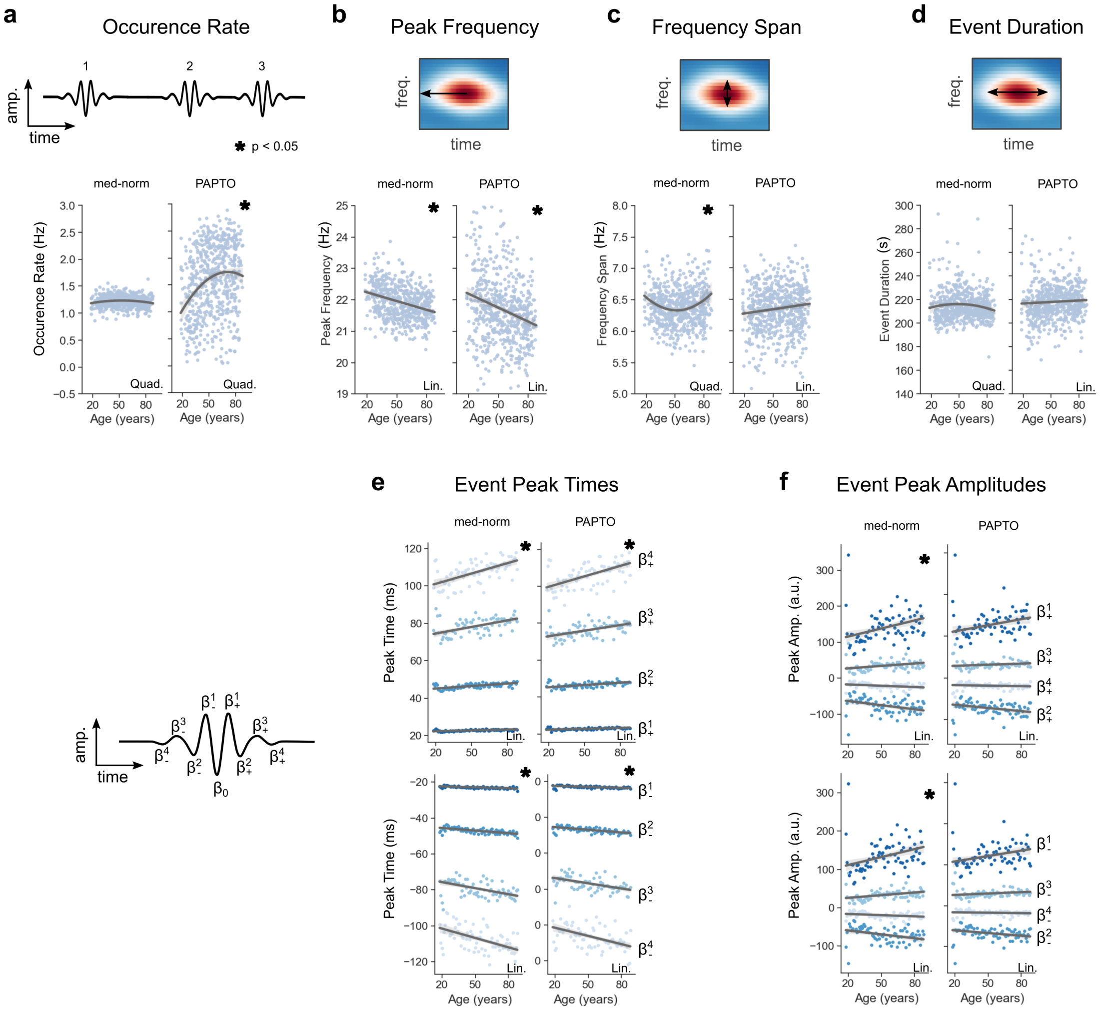

Figure 3.7: Left hemisphere S1: Resting-state sensorimotor transient beta events show significant age-related changes. Each individual parameter of transient beta events evaluated for age-related changes. (a)-(f) scatterplots showing participant-average beta event parameters (occurrence rate, peak frequency, frequency span, event duration, event peak times, and event peak amplitudes, respectively) as a function of participant age (one point represents one participant) with linear or quadratic fitted ageing models. Stars indicate statistically significant ($p<0.05$, Bonferroni corrected for multiple comparisons) non-zero age related changes. See Supplemental Figures for other anatomical ROIs.

	Method	F-stat	Model	p-value	Polynomial fit Quadratic term	Linear term	Intercept	Extremum age [yr]
parameter [unit]					[unit/y^2]	[unit/y]	[unit]	
burst rate [Hz]	PAPTO	10.56	Quadratic	**1.11E-11**	–2.67E-04	3.81E-02	3.81E-01	71
	med-norm	8.94	Quadratic	7.00E-02	–4.02E-05	4.25E-03	1.12E+00	53
peak frequency [Hz]	PAPTO	0.01	Linear	**3.20E-08**	–	–1.62E-02	2.26E+01	–
	med-norm	5.77	Linear	**1.14E-14**	–	–9.39E-03	2.24E+01	–
frequency span [Hz]	PAPTO	0.33	Linear	4.88E-01	–	6.21E-04	6.22E+00	–
	med-norm	18.07	Quadratic	**2.30E-03**	1.67E-04	–1.85E-02	6.79E+00	55
event duration [ms]	PAPTO	3.17	Linear	6.06E+00	–	1.40E-01	2.06E+02	–
	med-norm	16.74	Quadratic	1.40E+00	–5.49E-03	6.03E-01	1.97E+02	55
peak times [ms]								
	PAPTO	–0.07	Linear	**3.96E-07**	–	2.01E-02	2.17E+01	–
	med-norm	1.56	Linear	**7.97E-10**	–	1.71E-02	2.19E+01	–
	PAPTO	0.18	Linear	**7.31E-07**	–	6.02E-02	4.24E+01	–
	med-norm	0.73	Linear	**2.65E-11**	–	6.11E-02	4.29E+01	–
	PAPTO	–4.55	Linear	**3.85E-05**	–	1.56E-01	6.34E+01	–
	med-norm	–6.63	Linear	**2.52E-07**	–	1.86E-01	6.41E+01	–
	PAPTO	–9.09	Linear	**4.04E-08**	–	2.21E-01	8.70E+01	–
	med-norm	–8.41	Linear	**2.97E-08**	–	2.30E-01	8.74E+01	–
peak amplitudes [a.u.]								
	PAPTO	0.85	Linear	1.86E-01	–	8.74E-01	2.46E+01	–
	med-norm	2.29	Linear	**1.80E-02**	–	1.07E+00	1.99E+01	–
	PAPTO	2.95	Linear	3.36E-01	–	–6.82E-01	–3.00E+00	–
	med-norm	6.86	Quadratic	**2.45E-02**	1.12E-02	–1.93E+00	2.64E+01	86
	PAPTO	–0.02	Linear	2.43E+00	–	2.38E-01	5.71E+00	–
	med-norm	1.74	Linear	**3.94E-02**	–	3.40E-01	1.44E+00	–
	PAPTO	0.27	Linear	6.18E+00	–	–1.57E-01	–1.08E+00	–
	med-norm	3.96	Linear	2.45E-01	–	–2.23E-01	1.12E+00	–

Table 3.2: Left hemisphere S1: Modeling age-related changes of resting-state sensorimotor transient beta events. Ageing model fit parameters for each event characteristics. Model selection (linear vs quadratic) based on an F-test for each characteristic. Bolded rows indicate statistically significant ($p<0.05$, Bonferroni corrected for multiple comparisons) non-zero age related changes. See Supplemental Figures for other anatomical ROIs.

We found a significant linear decrease in the peak frequency of PAPTO events from about 22.1 Hz to 21.2 Hz across the age-range (18-88) of the Cam-CAN cohort (Figure 3.7 b). Such an age-related decrease suggests that older participants exhibit more low-beta events and less high-beta events compared to younger participants. We found a similar linear age-related decrease in the peak frequency of med-norm events. This age-related change is consistent across anatomical ROIs. We found no statistically significant age-related changes in the frequency span of events apart from marginal quadratic changes with age for med-norm events in left hemisphere S1 (Figure 3.7 c) and for PAPTO events in right hemisphere M1 (Figure B.7 c). Similarly, the duration of events shows no significant age-related changes throughout the adult lifespan except for marginal decrease for PAPTO events in right hemisphere S1 (Figure B.4 d). Note that the age-related changes of the med-burst beta event characteristics found here are similar to the age-related changes found in our previous work (Brady et al., 2020), but not identical. We attribute the differences to the stricter amplitude threshold we applied here, and the different signal localization techniques used.

In terms of the intra-event oscillations, we found that the beta waveform linearly spreads out in time by a factor of about 1.1 across the adult lifespan, independent of detection method and across all sensorimotor ROIs (Figure 3.7 e). This age-related change aligns with the age-related decrease in central frequency of the events see in Figure 3.7 b. Furthermore, we found an age-related increase in PAPTO event amplitude by a factor of about 1.6 across the adult lifespan in M1 (both hemispheres) but not in S1 (Figure 3.7 f & Figure B.4 f). A similar pattern is observed in med-norm event amplitude but with additional marginal age-related increases in left S1. Incorporating all the age-related changes shown in Figure 3.7 a-g, we have generated a visual depiction (roughly to scale) of how transient beta events in all four sensorimotor ROIs evolve with healthy human ageing (Figure 3.8), as detected by PAPTO.

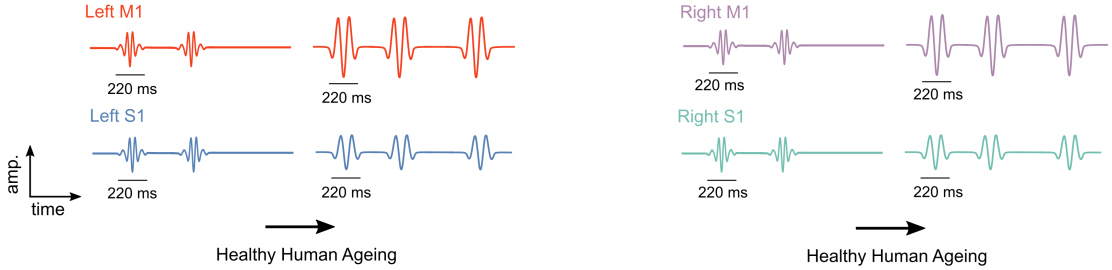

Figure 3.8: A visual depiction of age-related changes in sensorimotor extracranial neurophysiological signals. Each timecourse shown is a compilation of age-related changes for each beta event characteristic. Changes are shown approximately to scale.

3.6 Discussion

3.6.1 Insights Into the Ageing Somatosensory Thalamocortical Network

The age-related increase in transient beta event occurrence rate may help explain age-related decline in sensory perception. Previous work (Law et al., 2021) has found that beta events in S1 briefly facilitate sensory relay (i.e., a during-event effect) before a longer period of GABA inhibition lasting about 300 ms post-event. This post-event inhibition of sensory relay is the proposed mechanism for the decrease in human tactile perception following a beta event (Shin et al., 2017). The age-related increase in transient event occurrence rate found in this work, namely from 1.00 Hz in early adulthood to 1.75 Hz in later adulthood, can thus explain age-related decline in sensory perception (Brodoehl et al., 2013; Godde et al., 2018; Kalisch et al., 2009; Pleger et al., 2016; Wickremaratchi and Llewelyn, 2006). Considering the 300 ms inhibitory period post-stimulus reported by Law et al. (2021), an event occurrence rate of 1.75 Hz suggests the somatosensory thalamocortical network of older adults spends more than 50% of time in an inhibited state (compared to about 30% in younger adults). Although age-related changes at various stages of the sensorimotor processing pathway have been associated with the age-related decrease in tactile perception, including altered skin conformance (Bowden and McNulty, 2013) and an enhancement of cortical excitability (Lenz et al., 2012), our findings help to explain the role of the thalamocortical network in the healthy ageing process.

The age-related changes in somatosensory beta event characteristics observed in this work imply age-related changes in the upstream mechanisms involved in beta event generation. The occurrence of a somatosensory beta event is thought to be dictated by the presence of a strong distal drive (i.e., β_0) generated by bursts of excitatory inputs to supragranular layers (i.e., tuft excitation) originating from the thalamus (Law et al., 2021). Our finding of an age-related increase in event rate suggests these distal targeting thalamic bursts either occur more frequently and/or a higher proportion have sufficient amplitude to generate strong tuft excitation. Given that we did not observe an age-related change in event amplitude, we suggest that these distal targeting thalamic bursts occur more frequently with age. Furthermore, our observation that the waveform oscillatory frequency decreases with age suggests that there may be a decrease in the temporal coherence in this upstream thalamic bursting. Furthermore, the age-related changes in beta event characteristics observed in this work may also be driven by other factors not discussed, such as cortico-cortical interactions and changes in the functional coupling between subnetworks outside the sensorimotor system.

We additionally observed an age-related change in the somatosensory aperiodic activity, namely an approximate 10% decrease in the aperiodic exponent from early adulthood until 60 years old followed by a reversal back towards its original value in later years. In terms of the neurophysiological correlates, this ageing trend suggests that the ratio of underlying excitatory (i.e., AMPA) currents to inhibitory (i.e., GABA) synaptic currents peaks around 60 years (Gao et al., 2017). Furthermore, recall that the beta generative model (Sherman et al., 2016; Law et al., 2021) suggests that beta generation induces both excitatory AMPA (fast decay) and inhibitory GABA (slow decay) synaptic currents. We thus expect that characteristics of transient beta events and the aperiodic exponent are interlinked. The various ageing models revealed in this work however suggest this interconnection is highly complex and making collective inferences is out of the scope of this report. Computational modeling (Neymotin et al., 2020) is a promising avenue to further elucidate the underlying relationships between these parameters.

The age-related changes observed in the neurophysiological signals localized to M1 are like those observed in S1 with a few notable exceptions. Primarily, the transient beta event waveforms in M1 show the same age-related trends as those localized to S1 with the addition of a linear increase in amplitude by a factor of approximately 1.6X across the adult lifespan. This amplitude increase, which is indicative of narrow band power increase, suggests that motor events may recruit larger neocortical neural populations with increasing age. As less is known about the transient beta generators in M1 compared to S1, we cannot infer what this change implies in the context of the underlying thalamocortical network. In terms of the aperiodic activity, the aperiodic offset in M1 shows an age-related linear increase which is indicative of a broadband power increase. As broadband power correlates with single neuron firing rates (Manning et al., 2009), the age-related increase in broadband power observed here may be a consequence of an age-related increase in single neuron firing rates.

Although the ageing trends observed here may be true for the cross-sectional Cam-CAN cohort, care must be taken to not over generalize these findings. In particular, we observed several 2nd order (i.e., quadratic) ageing trends which all show a vertex mostly in the older half of the cam-CAN cohort. While these vertices may suggest the existence of developmental periods of critical differences within adulthood, they instead may be a manifestation of non-participation selection bias. Previous work found a strong association between age and participation in Cam-CAN study, with participation likeliness increasing from 18 to around 58-67 before rapidly dropping for participants older than 67 (Green et al., 2018). In other words, the significant age-related trends identified in this work follow a very similar mathematical trend to the non-participation bias in the Cam-CAN study. Such a bias could result in the misinterpretation of fundamentally linear ageing trends as being quadratic.

3.6.2 Additional Beta Waveform Features

Sherman et al. (2016) found that the temporal profile associated with beta events detected in the hand area of SI resembles an inverted Ricker wavelet produced by competing non-rhythmic distal and proximal current flow along the apical dendrites of neocortical pyramidal neurons. The big-data derived temporal profile of beta events shown in Figure 3.6 includes many of the distinct features found in the beta event waveform by Sherman et al. (2016), however we find additional oscillatory activity. In agreement with Sherman et al. (2016), we find the beta event waveform is dominated by a sharp high amplitude central trough (β_0) with two positive peaks about 25 ms before and after (β_-^1 and β_+^1, respectively). In disagreement with Sherman et al. (2016), we find the beta events includes several significant oscillations around zero at earlier and later times (i.e., β_-^3, β_-^4, . . .) causing the beta waveform to more closely resemble an inverted Morlet wavelet as opposed to an inverted Ricker wavelet. We confirmed that this beta event waveform difference is not a result of increased signal-to-noise ratio (SNR) from larger sample size; namely we generated the temporal profile of beta events using the 50 highest power event from a subset of 10 randomly selected participants to better match the human dataset analyzed by Sherman et al. (2016) and found an inverted Morlet wavelet beta event profile. Our results suggest that beta events may arise from proximal and distal neocortical inputs from the thalamus that are more rhythmic than previously thought. Next steps involve using the Human Neocortical Neurosolver software tool (Neymotin et al., 2020) to attempt to further investigate the neurophysiological origins of these additional beta event oscillations.

3.6.3 Extending our Analysis Approach to Other Neuroelectrophysiological Signals and Event Detection Techniques

Disambiguating transient events from the aperiodic activity is important for transient events that change with age, disease, tasks, cortical regions, or any other domain.

Primarily, these transient events are not limited to a particular frequency band, but rather could be detected at any frequency across the entire neuroelectrophysiological signal power spectrum. Due to the $1/f$-like nature of the aperiodic activity power spectral density, it is particularly important to disambiguate low frequency transient events, including mu, theta, and delta events, from the aperiodic activity. Although we have focused on demonstrating the significant implications of disambiguating beta events from aperiodic activity, we expect that lower frequency events exhibit more substantial changes after disambiguating from aperiodic activity. Further work with a focus on lower frequency events is required to elucidate the degree of these changes and their potential implications.

As an example, paroxysmal slow wave events (PSWEs) are relatively long-lasting (typically > 5 s) low frequency (typically < 6 Hz) transient events that indicate abnormally slow network activity. Recent evidence suggests PSWEs play a functional role in both Alzheimer's Disease and epilepsy (Milikovsky et al., 2019). The detection of PSWEs conventionally involves calculating the median power frequency directly from single-trial neural power spectra. As discussed in this work, the shape of neural power spectra is largely dependent on the aperiodic activity power spectrum. Thus, future work involving the detection and characterization of PSWEs should take care to normalize the neural power spectra by $\eta(f)$ to avoid conflating PSWE properties with properties of the aperiodic activity.

In this work, we disambiguated the beta events from the aperiodic activity by defining the event amplitude detection threshold in terms of a multiple of the aperiodic activity power as an alternative to the conventionally used median power. Other event detection techniques have been reported in the literature which may also benefit from our analysis approach. For example, other authors (Tinkhauser et al., 2017) set the event detection threshold as the 75th percentile of event amplitudes. To extend our analysis approach in this case, we recommend the power of the event power be normalized by $\eta(f)$ to avoid detection frequency bias. Furthermore, in recent years, there has been a trend towards detecting transient events using Hidden Markov Models (HMM) to avoid the arbitrary threshold selection intrinsic to the amplitude-thresholding techniques. In time-delay embedded HMM, each transient event is identified as a period of neural activity with a distinct power spectrum, where each distinct spectrum is considered an "HMM state" (Quinn et al., 2019). To disambiguate the transient events from the aperiodic activity in this case, one could separate the neural power spectra into their rhythmic and aperiodic components followed by inferring HMM states of two types, namely rhythmic HMM states and aperiodic HMM states. This approach would avoid conflating changes within the two types of activity and could provide the benefit of simultaneously identifying how the two signals independently change in time and between participants. Although we have suggested possible avenues to apply aperiodic/transient rhythmic parameterization with different transient event identification techniques, there may be other effective avenues not discussed. Further studies are required to identify the potential implications disambiguating transient rhythmic events from the aperiodic activity for other event detection techniques.

3.6.4 Comparing PAPTO to Other Event Detection Algorithms

PAPTO joins a rapidly growing list of algorithms designed to identify short-lived transient episodes of oscillatory activity in single trial neuroelectrophysiological recordings (Cole and Voytek, 2019; Feingold et al., 2015; Sherman et al., 2016; Shin et al., 2017; Tinkhauser et al., 2017; Watrous et al., 2018; Whitten et al., 2011). In particular, PAPTO is conceptually similar to eBOSC (extended Better Oscillation Detection) (Kosciessa et al., 2020) in that both techniques provide event-wise assessment of transient oscillations baselined by the $1/f$ aperiodic activity, yet they differ in terms of aperiodic activity modelling (i.e., fooof compared to 'robust regression'), detection threshold (multiple of $\eta(f)$ compared to the 95th percentile of $\chi^2(2)$ distribution of the $1/f$ power), and approach to identify and characterize events. Systematically comparing PAPTO with eBOSC and other burst detection techniques is challenging due to the vast parameter space of each technique and the lack of objective metric to assess algorithm performance. In this work, we were able to effectively compare PAPTO with the Shin method as we limited the parameter space to one dimension (i.e., threshold baseline, $\eta(f)$ vs. $\widetilde{E}(f)$) thereby allowing us to directly assess the impact of disambiguating the oscillatory events from the aperiodic activity.

3.7 Conclusions

The PAPTO algorithm is a novel approach to analyzing neuroelectrophysiological data as a disambiguated combination of transient rhythmic events and aperiodic activity. PAPTO starts with extracting the aperiodic power spectrum from neuroelectrophysiological data using the recently published 'fooof' algorithm (Donoghue et al., 2020). The aperiodic power spectrum is then used power baseline for detecting transient events via an amplitude-thresholding technique developed by Shin et al. (2017). The effectiveness of PAPTO is demonstrated using resting-state sensorimotor MEG data from the Cam-CAN cross-sectional study of healthy ageing over the adult lifespan (n=600, ages 18-88) (Shafto et al., 2014; Taylor et al., 2017). Our findings reveal that PAPTO is more sensitive to neocortical transient beta rhythms compared to more conventional transient event detection algorithms and that the PAPTO captures more variance in the resting state beta event occurrence rate across participants. The improved sensitivity of PAPTO reveals that the beta occurrence rate almost doubles over the adult lifespan.

3.8 Acknowledgements

Data collection and sharing for this project was provided by the Cambridge Centre for Ageing and Neuroscience (Cam-CAN). Cam-CAN funding was provided by the UK Biotechnology and Biological Sciences Research Council (grant number BB/H008217/1), together with support from the UK Medical Research Council and University of Cambridge, UK. Research presented in this paper was funded by the Natural Sciences and Engineering Research Council of Canada Discovery Grant program. Scholarship support was provided by the Nova Scotia Department of Health and Wellness, the province of Nova Scotia, and Dalhousie University. The authors would also like to thank Lindsey Power for fruitful discussions.

3.9 Follow-up to Preamble (section 3.1)

The following section is not published (February, 2022) in NeuroImage

In Chapter 3, we found that amplitude thresholding events based on the modeled aperiodic activity compared to the median power enhances the sensitivity of burst detection to inter-subject variance in burst rate (see Figure 3.5). In relating this finding back to Section 3.1, this finding can be re-framed such that inter-subject variance in burst rate is *lost* when dividing out the median power. PAPTO thus effectively recovers this lost information and *recasts* the age-related increase in the amplitude of the beta peak in the median power spectrum in Figure 3.1 to an age-related increase in the beta burst rate. The results presented in Chapter 3 do not completely nullify the age-related changes observed in Chapter 2, but they do suggest the age-related trends in Chapter 2 should be considered with the caveat that some of the variance between participants is lost due to median power normalization.

The question then arises if/how the main findings stemming from Chapter 2 (i.e., changes in beta burst rate underlie changes in spectral beta power during the motor task and with age) would change if PAPTO, rather than the median normalization technique, was used to identify transient events. While this research question was not explicitly investigated, I would expect the main findings from Chapter 2 to remain the same:

- Primarily, I would expect that PAPTO-detected burst rate would show the same changes over the motor task phases as was found in Chapter 2 (i.e., lower burst rate during movement and higher burst rate post-movement, compared to baseline) but potentially with greater relative changes between the movement phases. As shown in Figure 3.3, the median power spectrum shows similar rhythmic features as the mean power spectrum, and we know from Bardouille and Bailey (2019) that the mean spectral power changes over the motor task. Thus, I would expect the beta peak in the median power spectrum to also change during the motor task (in the same manner to the beta power). The improved ability of PAPTO to recognize differences in spectral beta power through the quantification of the burst rate would then translate to more substantial changes in the burst rate throughout the motor task.

- Given the substantial difference in the age-related change in beta burst rate between PAPTO and med-norm events shown in Figure 3.7, I would expect that the age-related changes in beta burst rate in each phase of the button press task (as shown in Figure 2.4) would also substantially change. At the same time, I would also expect to still see the same relative differences in age-related changes between the phases, which is the underlying signal for the age related changes in beta ERD and PMBR (as discussed in section 2.4.2).

Though I have made a series of predictions based on applying PAPTO to the Cam-CAN button press data, it is important to note that very short epochs (< 2 s), like those designated to the phases of the button press task, pose a potential obstacle for PAPTO as modeling of the aperiodic activity is highly dependent on the low-frequency components of the neural power spectrum.

Chapter 4

Transient-burst Evoked Hemodynamic Response

4.1 Abstract

The transient events description of beta-frequency electrophysiological activity in the human sensorimotor cortex is well-established in the neuroimaging literature. While extensive work has focused on exploring these distinct temporal events in extracranial recordings, there has yet to be a study on their coupling to other neuro-biological processes, such as hemodynamic brain activity. In this work, we use simultaneous EEG-fNIRS in 26 healthy participants to investigate the hemodynamic changes coupled to the occurrence of transient events. The two objectives are (1) to extract the burst-evoked hemodynamic response function (HRF) for transient mu, beta, and gamma events using resting state recordings, and (2) to evaluate the contribution of neurovascular changes evoked by transient events to the total measured hemodynamic response over a unilateral finger-tapping motor task. In terms of objective (1), we found that transient beta events evoke a significant (at the 0.05 level) decrease in oxy-hemoglobin concentration and increase in deoxy-hemoglobin concentration, both peaking about 10 s after the burst event. No significant changes were found for mu or gamma events at the 0.05 level, although we found mu-evoked decrease in oxy-hemoglobin at the 0.1 significance level. We discuss this beta-specific hemodynamic response in the context of computational models in the literature, and suggest that the negative polarity of the response may arise from a period of GABA inhibition following the beta event. In terms of objective (2), we found evidence that beta events contribute to the "initial dip" phase of the total hemodynamic response measured over the motor task. We hesitate to generalize this result however as we find it may simply be an artifact of inadequate baseline interval between task blocks. This work is an important step to elucidate the neuro-biological mechanisms surrounding the occurrence of sensorimotor transient events, towards a better understanding of the neuro-hemodynamic coupling in the healthy human brain.

4.2 Introduction

Sustained sensorimotor cortical rhythms are manifestations of brief high-power events that accumulate upon averaging over time and/or trials (Jones, 2016; van Ede et al., 2018). These so called *transient events* or *transient bursts* are evident and detectable in single-trial magneto-/electro-encephalography (M/EEG) recordings in humans. Extensive work has focused on the development of transient event detection algorithms (Feingold et al., 2015; Lundqvist et al., 2016; Shin et al., 2017; Brady and Bardouille, 2022; Fabus et al., 2021; Salman et al., 2018; Jas et al., 2017; Quinn et al., 2019; Kosciessa et al., 2020; Briley et al., 2021; La Tour et al., 2018), investigating their thalamocortical generative mechanisms (Sherman et al., 2016; Law et al., 2022), exploring their relation to behaviour and information processing (Shin et al., 2017; Little et al., 2019; Brady et al., 2020; Seedat et al., 2020; Lundqvist et al., 2016, 2018), and in identifying their changes with disease (Heideman et al., 2020; Gascoyne et al., 2021) and healthy ageing (Brady et al., 2020; Brady and Bardouille, 2022; Power and Bardouille, 2021). Yet, little attention has been given to their relation to other ”downstream” neuro-biological processes, such as their coupling to hemodynamic effects. This coupling is the focus of this work.

Sensorimotor beta-frequency (15-30 Hz) rhythms are among the most well-established *bursty* rhythms. Sensorimotor beta is generated in an inhibitory thalamocortical network, where an increase in rhythm strength indicates an inhibited state of processing and rhythm suppression indicates an activated state (Pfurtscheller and Lopes da Silva, 1999). Correspondingly, transient beta-frequency bursts evidently play an inhibitory role in sensorimotor processing. Namely, Shin et al. (2017) found that the pre-stimulus beta event occurrence rate is a reliable predictor of sensory perception in humans and mice, with higher occurrence rates in the 100-300 ms pre-stimulus time correlating with sensory suppression. These findings compliment previous work from the same group that shows lower pre-stimulus beta power in the primary somatosensory cortex predicts an increase in the probability of detection of tactile stimuli (Jones et al., 2010). Similarly, Little et al. (2019) found that beta events occurring close in time to a visual cue in a cued-movement paradigm delay movement initiation. The generative mechanisms of transient beta events have been investigated by Sherman et al. (2016), who showed that beta events may originate from synchronous bursts of excitatory synaptic drive which originate in the thalamus and simultaneously target both the proximal and distal dendrites of neocortical pyramidal neurons. Law et al. (2022) recently expanded on the work from Sherman et al. (2016) and reported that the distal-targeting excitatory drive briefly facilitates sensory relay (i.e., a during-event effect) before a longer period of GABA inhibition lasting about 300 ms post-event. This post-event GABA-induced inhibition explains the decrease in human tactile perception following a beta event (Shin et al., 2017). Less is known about transient events in the mu (8-12 Hz) frequency range compared to beta events, however evidence shows that transient mu and beta rhythms have some degree of temporal co-occurrence, implying that they share components of neural mechanism (Jones et al., 2010; Seedat et al., 2020). Transient gamma events have been detected in the human motor cortex during movement (Muthukumaraswamy, 2010), where they reflect sensory reafference and have a facilitative role in movement initiation (for a comprehensive review of transient gamma oscillations in the motor cortex, see (Cheyne and Ferrari, 2013)). Transient gamma activity has also been studied outside of the sensorimotor cortices, particularly in the prefrontal cortex in the context of working memory (Lundqvist et al., 2016, 2018).

Our previous work (Brady et al., 2020) shows that event-related synchronization (ERS) and desynchronization (ERD) of sensorimotor rhythms during voluntary movement are predicated by changes in the probability of occurrence of transient events. We observed this phenomenon by analysing unilateral button press motor task data from the open-access Cam-CAN dataset (Shafto et al., 2014; Taylor et al., 2017) in both a transient events framework (Brady et al., 2020) and using a more traditional spectral power analysis framework (Bardouille and Bailey, 2019). Namely, we found fewer mu and beta events during the movement phase of the motor task which correlates with mu and beta ERD, respectively. We also found a higher number of beta events compared to baseline pre-stimulus levels were detected in the post-movement time window, corresponding to the post-movement beta rebound (PMBR), or beta ERS. We additionally observed a higher probability of detecting gamma-frequency events during movement, corresponding to the movement related gamma synchronization (MRGS). Similar results have also been reported by other groups (Little et al., 2019; Seedat et al., 2020).

Neural activity can be indirectly assessed by monitoring the "downstream" hemodynamic signals. The onset of neural activation (i.e., by a stimulus, voluntary movement, etc.) induces an increase in cerebral metabolic rate of oxygen ($CMRO_2$) and a compensatory stronger increase in cerebral blood flow (CBF) (Fox and Raichle, 1986). The combination of these two effects leads to a decrease in local deoxy-hemoglobin concentration. Deoxy-hemoglobin is paramagnetic and thus a decrease in its concentration gives rise to an increase in the MR signal, resulting in the robust positive fMRI blood oxygen level dependent (BOLD) response (Ogawa et al., 1990). A post-stimulus undershoot in the MR signal is also commonly observed as part of the BOLD response and can last up to 30 s after stimulation has ended (Mullinger et al., 2013). The origin of this undershoot is still debated (van Zijl et al., 2012), however recent work found that this post-stimulus effect may arise from an altered CBF/$CMRO_2$ coupling ratio (compared to during stimulation) induced by post-stimulus cortical inhibition (Mullinger et al., 2017). While not as robust as the post-stimulus undershoot, there are several reports of an "initial dip" in the BOLD signal (Hu and Yacoub, 2012), lasting about 1-2s before the increase in CBF. This initial dip has been attributed to early deoxygenation from the initial increase in $CMRO_2$.

The electrophysiological correlates of the BOLD signal have been extensively explored however complete and comprehensive models remain elusive. Using simultaneous intracortical electrophysiology and fMRI BOLD imaging in primates, Logothetis et al. (2001) found that the BOLD response to visual stimuli is more closely related to local field potentials (LFPs) rather than multi-unit recordings. Since the LFP reflects post-synaptic/dendritic activity, this finding suggests that the BOLD mechanism reflects the input and intracortical processing of a given area rather than its spiking output. Notably, the correlation observed by Logothetis et al. (2001) was specifically found for power modulations in gamma frequency LFPs. High gamma LFP-BOLD correlations have also been confirmed in mice (Mateo et al., 2017), cats (Niessing et al., 2005) and in humans via intracranial electrocorticography in patients with epilepsy (Mukamel et al., 2005; Lachaux et al., 2007). These studies suggest a close spatio-temporal correlation between hemodynamic responses and neuronal synchronization, at least in the gamma frequency band. In terms of lower frequency oscillatory activity, early work in EEG-informed fMRI in healthy adults found that the BOLD signal is negatively correlated with spontaneous (i.e., resting state) alpha activity in extensive areas of the occipital, frontal, and parietal lobes (R. Goldman, J. Stern, J. Engel, 2002; Laufs et al., 2003; Moosmann et al., 2003; Gonçalves et al., 2006). In sensorimotor areas, motor-task induced changes in mu and beta power inversely correlate with the BOLD signal (Ritter et al., 2009; Formaggio et al., 2008; Lachert et al., 2017; Yuan et al., 2010; Stevenson et al., 2011). Strongest correlations occur in S1 for mu ERD and M1 for beta ERD (Ritter et al., 2009). At rest, negative correlations have been found between the BOLD signal and spontaneous fluctuations in the amplitude of sensorimotor mu and beta rhythms (Yin et al., 2016; Tsuchimoto et al., 2017).

Changes in blood oxygenation can also be monitored via optical imaging techniques, such as functional near-infrared spectroscopy (fNIRS). While limited in spatial resolution relative to fMRI (cm vs mm), fNIRS offers the advantage of quantifying time-resolved concentrations of oxy- and deoxy-hemoglobin. fNIRS-measured oxy-hemoglobin generally shows strong positive correlations with the BOLD signal while deoxy-hemoglobin generally shows anticorrelations (Cui et al., 2011). Analogous to the BOLD initial dip (see above), oxy- and deoxy-hemoglobin show an initial dip and initial rise (Jasdzewski et al., 2003), respectively. Likewise, oxy- and deoxy-hemoglobin show a post-stimulus undershoot and overshoot, respectively (Schroeter et al., 2006).

While there has been extensive work exploring detection algorithms, generative mechanisms, and functional significance of transient burst events, there are no investigations into the downstream metabolic/hemodynamic changes associated with these brief bouts of brain activity. In this work, we simultaneously record EEG and fNIRS signals in 26 healthy participants to investigate the hemodynamic correlates of sensorimotor transient mu, beta, and gamma events. The first objective is to identify the hemodynamic response function associated with resting-state transient mu, beta, and gamma events. We hypothesize that mu, beta, and gamma events each evoke a non-zero/measurable hemodynamic response. Based on positive correlation between the gamma LFP and the fMRI BOLD signal introduced above, we suspect transient gamma events evoke an increase in oxy-hemoglobin concentration. Based on the negative correlations between the BOLD signal and spontaneous fluctuations in the amplitude of sensorimotor mu and beta rhythms introduced above, we suspect transient mu and beta events evoked a decrease in oxy-hemoglobin concentration. The second objective of this work is to evaluate the contribution of neurovascular changes evoked by transient events to the total measured hemodynamic response over a unilateral finger-tapping motor task. Given that motor tasks induce systematic changes in the burst rate of mu, beta, and gamma events, as introduced above, we hypothesize that the contribution of the transient events to the total measured hemodynamic response is non-zero. In elucidating the hemodynamic correlates of transient burst events, this work provides novel insights into the neuro-biological mechanisms surrounding the occurrence of transient events and helps to explicitly identify one contributing factor to spontaneous and task related changes in blood oxygenation. This work is an important step towards relating electrophysiology to vascular responses in the healthy human brain.

4.3 Methods

4.3.1 Participants

We collected simultaneous EEG-fNIRS data from thirty-two healthy volunteers. Four datasets were dropped due to poor fNIRS scalp coupling, one was dropped due to insufficient cap fitting, and one was dropped due to data loss. The remaining participants (n = 26) had an average age of 31 ± 3.6 (mean ± standard error of the mean). Twenty-four of the participants were right-handed. All participants provided written consent and ethics approval for the study was obtained through the Dalhousie Research Ethics Board (HSHREB No. 2017-4197).

4.3.2 Data Acquisition

Simultaneous EEG-fNIRS data were collected from each participant during a 10-minute wakeful resting period and during a motor task block design paradigm (described below). EEG data were collected using a 22-electrode Synamps RT system (Compumedics Neuroscan, Charlotte, NC) at a sampling rate of 1000 Hz. Impedance for all electrodes was confirmed to be <15 kohm at the start of data collection. Electrooculogram (EOG) was obtained using self-adhering electrodes placed above and below the left eye (vEOG), and just lateral to the left and right eye (hEOG). Electrocardiogram (ECG) was obtained using self-adhering electrodes placed on the upper left and upper right arms. fNIRS data were collected using a 30-channel (8 sources, 15 detectors) NIRx NIRScout Extended fNIRS system at a sampling rate of 7.8125 Hz. Sufficient skin-optode contact was ensured for each source-detector pair using a combined quality metric calculated within the NIRx acquisition software (Manual, 2014). Most pairings (>90% per participant) were in the *excellent* quality range for the start of data collection, indicating a gain (i.e., amplification of received light at the detector) of less than 10^6, a signal level (i.e., average voltage output by the detector during a short test scan) between 0.09 and 1.40 V, and signal noise percentage (timecourse standard deviation / mean * 100) of less than 2.5%. The other pairings (<10% per participant) were maintained within an ”acceptable” range (gain $< 10^7$, signal level 0.03-2.50 V, and signal noise 2.5-7.5%) The EEG electrodes and fNIRS channels were arranged in a checkerboard pattern over each sensorimotor hemisphere (see Figure 4.1 for sensor layout).

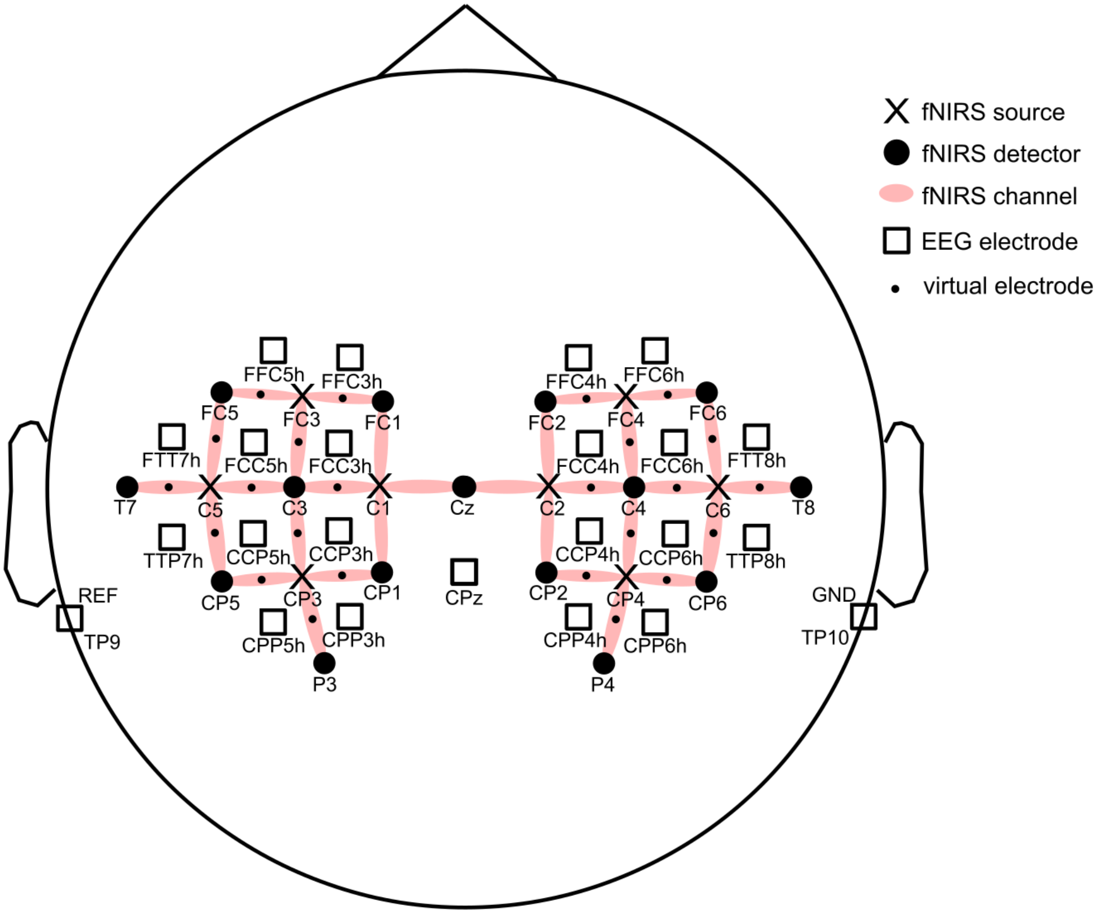

Figure 4.1: Sensor layout indicating positions of EEG electrodes, fNIRS sources, fNIRS detectors, and virtual electrodes. Virtual electrodes are described in section 4.3.4. Location labels are based on the EEG international 10-20 system.

The motor task block design paradigm consisted of 15 task blocks with duration jittered between 8-10 s (jittered to minimize anticipatory effects). The motor task used was a unilateral sequential finger tapping task on the left hand consisting of touching the thumb pad to successive finger pads with the order: index, middle, index, ring, index, pinky, index, ring, index, middle (repeat). The participant was instructed to continuously perform the finger tapping task for the duration of each task block. The end of each task block was accompanied by an 8-10 s *pause* period, where the participant was instructed to remain still. Audio cues guided participants through the experiment and simultaneous triggers were sent to both the EEG and fNIRS recording hardware (via LabJack USB DAQ device) to mark the start and end of the different phases of data collection. Participants were instructed to keep eyes closed during both the 10-minute rest scan and the motor task block design paradigm.

4.3.3 Data Pre-Processing

The raw EEG signal for each participant was band pass filtered between 0.25 Hz and 110 Hz and notch filtered at 60 Hz to reduce power line noise. Independent component analysis (ICA) was carried out to identify 20 ICs in each recording using the FASTICA algorithm (Hyvärinen, 1999). ICs that matched the hEOG, vEOG, and ECG recordings (above) were excluded from signal reconstruction. Matches were determined if the Z-score (across ICs) of the correlation coefficient between the IC and the artifact recording exceeded 1.96 (95% C.I.). The first and last 10 s segments of the 10-minute resting-state recording were dropped from analysis.

The raw fNIRS signal was band pass filtered between 0.01 Hz and 3 Hz before being used to compute the hemodynamic states (i.e. oxy- and deoxy-Hb concentrations, [HbO] and [HbR]). Optical density and hemodynamic states were computed within the MNE environment (via the MNE-NIRS library) using the Beer-Lambert Law. Bad channels were identified if the scalp coupling index was below 0.5 (Pollonini et al., 2014). The heartbeat was removed from the data by bandpass filtering the [HbO] and [HbR] signals between 0.04 Hz and 0.7 Hz. The first and last 10 s segments of the 10-minute resting-state recording were dropped from analysis.

4.3.4 Virtual Electrodes, Event Detection, & Unique Events

Transient events were detected at 12 virtual electrodes in each hemisphere for each participant. The 12 virtual electrode locations correspond to locations where the midpoint between two neighboring EEG electrodes overlaps with an effective fNIRS channel (i.e., midpoints between a source and a detector pair). See Figure 4.1 for locations of virtual electrodes relative to EEG electrodes and fNIRS optodes. Each virtual electrode position has one associated transient events list and one associated fNIRS signal. A TFR for transient event identification was obtained at each virtual electrode location by averaging TFRs from each of the two neighboring EEG electrodes. The TFR at each neighboring EEG electrode was calculated as the squared magnitude of the complex wavelet-convolved data as described in section 3.4.7.

Transient events in the mu (8-15 Hz), beta (15-30 Hz), and gamma (30-90 Hz) bands were detected at each virtual electrode using the PAPTO method as described in Chapter 3. Due to signal spreading, the same transient event could be detected at multiple virtual electrodes. However, our goal was to identify the transient events uniquely for each virtual electrode (i.e., assign each event detected over the sensorimotor array in each hemisphere to one and only one virtual electrode). Identifying unique events avoids repeat analysis of the same transient event detected over multiple EEG electrodes by assigning events to the electrode at which the magnitude is maximal. An event was designated as a *unique event* at a virtual electrode only if there was no other transient event detected at any virtual electrode in the same hemisphere with higher peak power and occurring within the peak time ± half the event duration and within the peak frequency ± half the frequency span of the event in question.

The amplitude threshold for defining transient events was then assessed uniquely for each frequency band following the process described in section 3.4.7. As depicted in Figure 4.2, we found an amplitude threshold of $13 \times n(f)$ for mu events, $7 \times n(f)$ for beta events, and $6 \times n(f)$ for gamma events. The remainder of the analysis is conducted on unique supra-threshold transient events, hereinafter referred to as *transient bursts* or *transient events*, unless otherwise indicated.

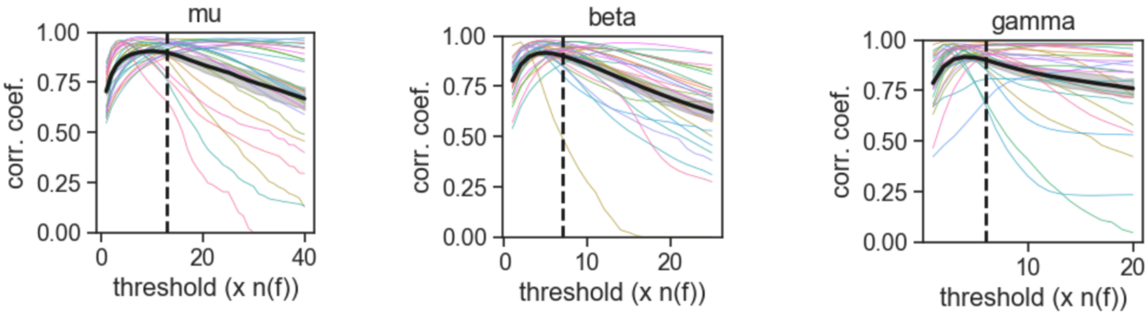

Figure 4.2: Defining amplitude thresholds for mu, beta, and gamma events. Correlation coefficient between average resting state band power and percent of spectrogram pixels with power above cutoff value, as a function of cutoff value. One colored curve per participant. The solid black curves shows the average across all participants. Shaded region depicts the standard error of the mean. As a conservative (i.e., strict) estimate of the threshold value, we selected the amplitude threshold as the largest integer value that is still within 1 standard error of the mean from the peak value. Found threshold are $13 \times n(f)$ for mu events, $7 \times n(f)$ for beta events, and $6 \times n(f)$ for gamma events (as depicted by the vertical dashed lines).

4.3.5 Characterizing Resting-State Transient Events

Transient events were characterized in the time-frequency domain to obtain the *peak time, peak frequency, event duration*, and *oscillatory cycles per event* for each event as described in section 3.4.8. The *peak power* of each event is reported as a multiple of the aperiodic activity, $\eta(f)$, as in equation 3.4. Transient event *peak frequency* spectra as well as histograms for *peak power*, *event duration*, and *oscillatory cycles per event* were generated for each participant using events detected across all 24 virtual EEG electrodes. The *peak power*, *event duration*, and *oscillatory cycles per event* were then averaged across all events and virtual electrodes to obtain one averaged burst characteristic per participant. The *burst rate* for each participant was calculated as the average burst rate over the left and right hemispheres. The burst rate in each hemisphere was calculated as the total number of transient events identified across all 12 hemisphere-specific virtual EEG electrodes divided by 580 s.

4.3.6 The Burst-Evoked Hemodynamic Responses (Real vs. Sham)

The grand-average burst-evoked hemodynamic response functions (HRFs) were assessed for mu, beta, and gamma transient events (i.e., the first objective: *To identify the hemodynamic response function associated with transient mu, beta, and gamma events*) using a conventional averaging technique applied to the resting-state data. At each virtual channel location, the transient event peak times were used to epoch the fNIRS data into 35 s segments (from – 10 s to + 25 s relative to the event peak time). The epochs were baselined to the -2 to 0 s interval. The baselined epochs were then averaged over all events at each virtual electrode location and then across all virtual electrodes to obtain one averaged burst-evoked hemodynamic response per frequency band for each participant. The grand-average burst-evoked HRF for each frequency band (HRF_μ, HRF_β, HRF_γ) was then obtained by averaging the participant-level burst-evoked hemodynamic responses. The standard error of the mean (SEM) on the grand-average burst-evoked HRFs were calculated from the variance across the participant-level responses.

The statistical significance of the burst-evoked HRFs were addressed by comparing the real grand-average HRFs (one for each frequency band, generated as described above) against a series of 100 sham grand-average HRFs for each frequency band. The sham grand-average HRFs were generated in an identical manner to the real grand-average HRFs with the exception that the transient event peak times were randomly shuffled prior to epoching the fNIRS data. Peak time shuffling was accomplished by first generating a list of real inter-burst intervals (i.e., the times between sequential events) and then randomly shuffling that list and using it to generate a set of new (sham) peak times. This process ensured that each set of sham peak times had the same distribution of inter-burst intervals as the real set of peak times.

One p-value was calculated to directly assess the first hypothesis (*Individual transient mu, beta, and gamma events evoke a non-zero hemodynamic response*) separately for transient events in each frequency band. We first identified a time window in the real grand-average burst evoked HRF where it was furthest from baseline levels. Time windows selected were 10-12 s for HRF_μ, 8-12 s for HRF_β, and 8-11 s for HRF_γ (see Figure 4.3). We then calculated the average deviation from baseline within these time windows in terms of number of SEMs. We did the same process for each of the 100 grand-average sham HRFs (using the same time windows identified in the real grand-average HRFs) to obtain a sham distribution of number of SEMs away from baseline. The p-value was calculated as the portion of sham curves with more SEMs away from baseline compared to the real curve (ex. if only 3 out of the 100 sham curves were more SEMs away from baseline compared to the real curve in the same time window, $p \approx 0.03$).

We also assessed the temporal coincidence of transient events across frequency bands to assess co-dependence of the HRFs. A transient event in one frequency band (event A) was determined to be coincident with a transient event in a different frequency band (event B) if the peak time of event A fell within within ± 0.5 s of the peak time of event B and both A and B were detected at the same virtual electrode. For each virtual electrode for each participant, the percentage of coincident events were found for each pair of frequency bands. This produced one 3×3 (mu/beta/gamma × mu/beta/gamma) matrix of percentages per electrode per participant. The percentages were then averaged over virtual electrodes and participants.

4.3.7 Transient Event and Neurovascular Dynamics During Motor Task

The cleaned EEG data and fNIRS measured [HbO] and [HbR] were epoched between -2 and +16 s relative to the start of each motor task block. The participant was actively engaged in the motor task from 0 to 8 s. Between 8 and 10 s is the 'jitter window' as the participant may have still been engaged in the motor task or may have entered to the 'pause' phase of the paradigm. The participant was definitely in the 'pause' of the paradigm from 10 to 16 s. PAPTO was applied to the epoched EEG data to identify mu, beta, and gamma transient events throughout the motor task paradigm. The aperiodic activity model parameters obtained from applying PAPTO to the 10-minute resting-state data were input to the PAPTO algorithm. This was done because the short duration of each task epoch relative to the duration of the 10-minute resting-state recording results in a noisy neural power spectrum and thus a high variance in aperiodic fit parameters across trials for each participant. This assumes that the aperiodic parameters were unchanged between task and rest. For each 1 second interval in the epoch, the burst rate change was determined as the average number of transient events per unit time in that interval subtract the average burst rate within the baseline (-2 to 0 s).

To determine if the transient event hemodynamic response had a non-zero contribution to the task-evoked hemodynamic response, we predicted [HbO] and [HbR] signals without the contribution of hemodynamic changes evoked by the occurrence of transient beta events. Mu and gamma events were not included in this analysis stage as we found no significant mu or gamma event evoked hemodynamic response (see Figure 4.4). These "transient event-less" [HbO] and [HbR] signals (i.e., $[\text{HbO}]_{-E}$ and $[\text{HbR}]_{-E}$) were generated by subtracting out the real HRF_{β} from the (un-epoched) fNIRS measured timecourses following every occurrence of a transient beta event. The $[\text{HbO}]_{-E}$ and $[\text{HbR}]_{-E}$ timecourses were generated at each virtual sensor location for each participant and then epoched as described above.

We tested our hypothesis that the neurovascular changes evoked by transient events have a non-zero contribution to the measured hemodynamic response over a unilateral motor task block design experiment by assessing the difference between the [HbO] and [HbR] epoched signals and the $[\text{HbO}]_{-E}$ and $[\text{HbR}]_{-E}$ epoched signals. P-values were obtained via paired t-tests across participants using timeseries data averaged over the 0 - 8 s task block for oxy-hemoglobin and over the 10 - 15 s pause block for deoxy-hemoglobin (data-driven time windows with the largest difference between [HbO] and $[\text{HbO}]_{-E}$ and between [HbO] and $[\text{HbR}]_{-E}$, respectively).

4.4 Results

4.4.1 Resting-State Transient Event Characteristics

Figure 4.3 (a) shows the transient event peak frequency histograms averaged across all virtual electrodes for each participant. The distinct peaks in the mu and beta bands indicate the presence of mu and beta transient events, with more events detected near the middle of the bands. The gamma band shows a comparatively flat distribution, indicating that gamma transient events are as likely to occur at any frequency. The steps in the plot at 15 Hz and 30 Hz are due to the different amplitude thresholds for the different frequency bands (see section 4.3.4).

Fig 4.3 (b) shows the average resting state burst rate for transient mu, beta, and gamma events for each participant (calculated as described in section 4.3.5). The values depicted in Figure 4.3 (b) are the average of the two ROIs (i.e., two hemispheres) for each participant. The average burst rates across participants for each event type are shown in Tbl. 4.1. The mean beta burst rate across participants, 1.67 ± 0.12 Hz (mean ± SEM), is within one SEM of the Cam-CAN cohort average beta burst rates found in M1 and S1 (left and right) as reported in Chapter 3 (see Figure 3.5), indicating that our effort to mitigate signal spreading via considering only *unique events* in each hemisphere yields bursting activity reflective of the level of activity at the cortical source. The beta burst rates found here and in Chapter 3, both using the PAPTO method, are higher than the 1 Hz beta burst rate found by Shin et al. (2017) using the median normalization technique. As discussed in detail in Chapter 3, this difference can be attributed to the different power normalization factors (i.e., median power vs modeled aperiodic activity power spectrum). In terms of mu and gamma events, our data suggest that the gamma band is the most “bursty” of the three bands investigated with a burst rate of 2.24 ± 0.12 Hz, while mu band shows the lowest burst rate at 0.87 ± 0.06 Hz. As far as we know, this is the first report to quantify resting-state burst rate of transient events specific to the mu and gamma frequency ranges. Interestingly, Seedat et al. (2020) used Hidden Markov Modeling (HMM) to identify transient events as spectral patterns (referred to as 'states') in the 1-48 Hz range and found a burst rate of about 1 Hz. In contrast to our approach of separating activity by frequency band, HMM aggregates activity across frequency bands into a single state/event. Hence, we observe a higher burst rate (consider that the total burst rate in the 1-48 Hz range observed here would be $>$ 4 Hz) because we treat each frequency band independently.

The topographies in Fig 4.3 (b) show where the bursts are detected across the virtual electrode array. Values shown are the normalized (to the mean across sensors) burst rates at each virtual sensor location, averaged across all participants. The mu burst rate scalp topography shows that mu events are predominantly detected at the two posterior electrodes in the electrode array. This activity is likely occipital alpha. The mu frequency bursting activity detected at the two most central-anterior recording sites is more likely sensorimotor in origin. The beta burst topography is similar to the mu burst topography, however beta shows a more even distribution of burst rate across the same 4 identified electrodes, indicating that beta has a stronger sensorimotor component. The mu and beta burst rate scalp topographies shown here are similar to the alpha and beta resting-state power topographies shown by Fransen et al. (2015). Interestingly, Fransen et al. (2015) found that using lagged coherence (a metric that quantifies rhythmicity) to define oscillations as opposed to spectral power separates the central sensorimotor activity from the strong posterior activity even within the same frequency band. The gamma burst rate topography shows no discernible structure, indicating that gamma activity is generated more evenly across the cortical regions below the electrode array.

Figure 4.3 (c) shows event peak power histograms (calculated as multiples of the modeled aperiodic activity) for each type of event for each participant (averaged across virtual electrodes). The corresponding average values across participants are shown in Table 4.1. As compared to beta and gamma bands, the number of detected mu events drops off more slowly with increasing peak power, giving them a substantially higher average peak power.

Figure 4.3 (d) shows event duration histograms for each type of event for each participant (averaged across virtual electrodes). As shown in Table 4.1, the average duration of mu events across participants is 455 ± 12 ms and beta is 215 ± 2 ms. These values are very close to the duration of PAPTO-detected mu and beta events found in the Cam-CAN cohort in Chapter 3 (425 ± 6 ms and 218 ± 2 ms, respectively). Gamma event duration (77 ± 2) was found to be much shorter than mu and beta events. The decrease in event duration with increasing peak frequency is generally expected due to the inverse relation between time and frequency. In the context of transient neurophysiological events, it may be more informative/functionally relevant to quantify the number of cycles per event, as shown in Figure 4.3 (e) and in Table 4.1. Primarily, mu and beta events show comparable number of cycles (4.85 ± 0.08 and 4.45 ± 0.04, respectively) to those found in Chapter 2 (4.91 ± 0.05 and 4.58 ± 0.02, respectively). The longer duration and more cycles of mu events compared to beta events is unsurprising considering a previous report of stronger lagged coherence of mu rhythms compared to beta rhythms (Fransen et al., 2015).The number of cycles per gamma event (4.37 ± 0.03) is similar to beta events observed here. Our finding of around 4-5 beta cycles per event is consistent with the number of cycles per event observed in LFP recordings in the sensorimotor cortex of monkeys by Murthy and Fetz (1992) (Murthy and Fetz, 1992), who show that these oscillations correspond to bouts of synchronous unit activity in the underlying neural population.

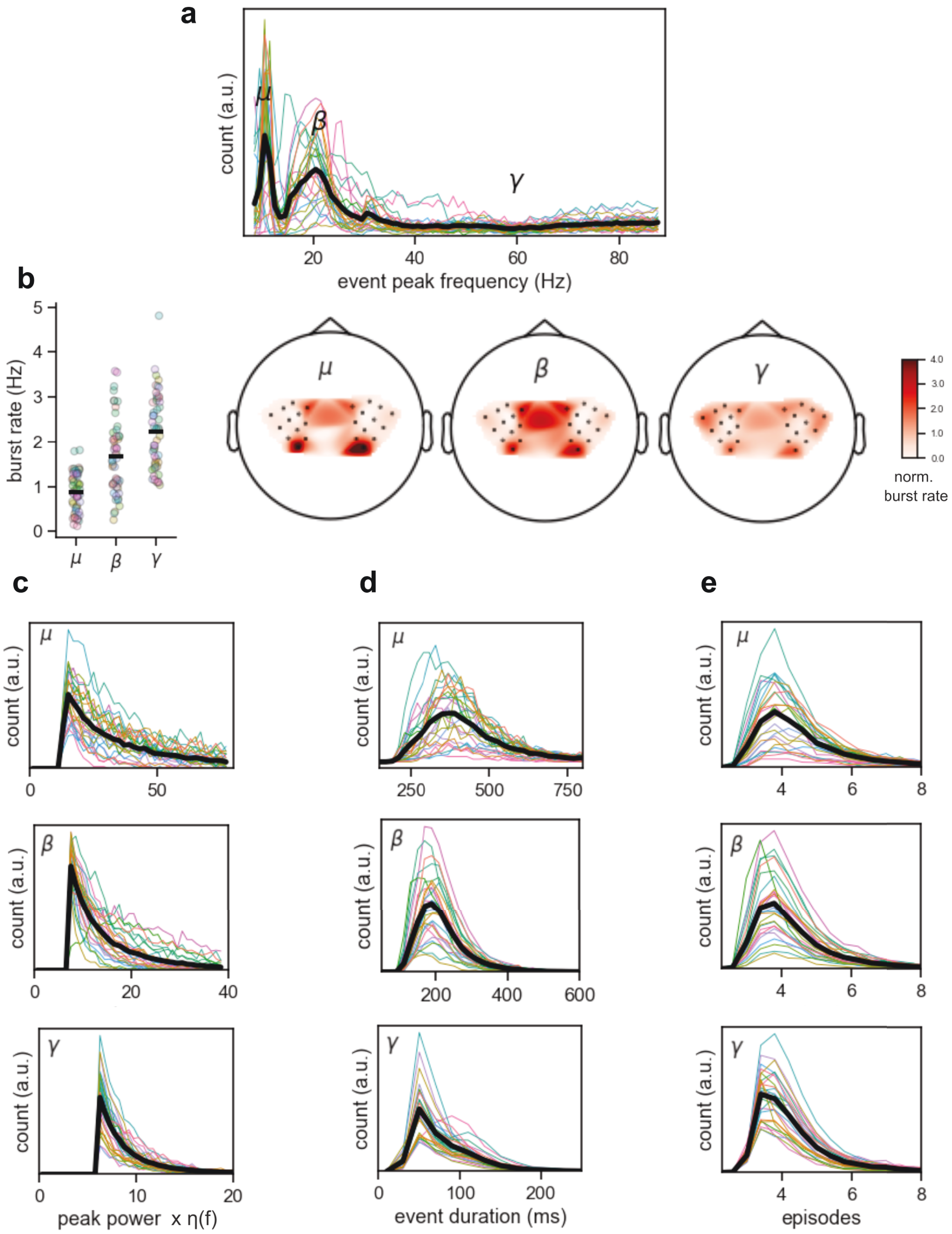

Figure 4.3: (a) event peak frequency distributions depicting distinct mu, beta, and gamma bands. Each colored line represents one participant. The black line is average across participants. (b) burst rate for each event type (one point per participant). Averages across participants indicated by the horizontal line. Topographies show normalized burst rates (to the mean), averaged across all participants. (c) peak power, (d) event duration, and (e) cycles (episodes) per event histograms for each event type. Each colored line represents one participant. The black line is average across participants.

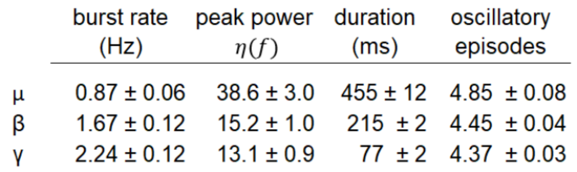

	burst rate (Hz)	peak power $\eta(f)$	duration (ms)	oscillatory episodes
μ	0.87 ± 0.06	38.6 ± 3.0	455 ± 12	4.85 ± 0.08
β	1.67 ± 0.12	15.2 ± 1.0	215 ± 2	4.45 ± 0.04
γ	2.24 ± 0.12	13.1 ± 0.9	77 ± 2	4.37 ± 0.03

Table 4.1: Mean burst characteristics (± standard error of the mean) across participants for each event type.

4.4.2 Transient Burst-Evoked HRF

Figure 4.4 depicts the transient burst-evoked HRFs for mu (top), beta (middle), and gamma (bottom) events for both oxy- (left) and deoxy-hemoglobin (right). Primarily, our data suggest that transient beta events evoked significant non-zero HRFs for both oxy- and deoxy-hemoglobin. In the 8-12 s time window following the occurrence of a beta event, the [HbO] dips to about 1.3 ± 0.4 μM (mean ± SEM) below baseline (0 - 2 s prior to the event) levels. This corresponds to 3.08 SEMs away from 0, which is substantially higher magnitude than all 100 sham curves in the same time window (all $<$ 2.5 SEMs). We found a complimentary increase in [HbR] to about 0.2 ± 0.1 μM above baseline levels in the same 8-12 s time window. This corresponds to 2.06 SEMs away from 0, which is higher than 95 out of the 100 sham curves in the same time window. This comparison of the real HRF against the 100 sham HRFs gives a rough estimate of p-values indicating the significance level of a non-zero burst-evoked HRF. In this case, we found that transient beta events evoked a change in [HbO] at the $p \approx 0.00$ significance level and evoke a change in [HbR] at the $p \approx 0.05$ significance level.

For mu and gamma transient events, a significant HRF was not observed in our data. In an analogous manner to that described above, we found that the real mu and gamma burst-evoked HRFs for both [HbO] and [HbR] do not (significantly) differ from the corresponding distribution of sham HRF magnitudes. The p-value estimates are $p \approx 0.08$ for changes in [HbO] and $p \approx 0.39$ for changes in [HbR] for mu events, and $p \approx 0.44$ for changes in [HbO] and $p \approx 0.37$ for changes in [HbR] for gamma events.

While the statistical analysis for the mu burst evoked HRF reveals no significant changes at the 0.05 significance level, there is a trend towards a significant effect for changes in [HbO]. To ensure this is not simply due to the temporal/spatial coincidence of mu and beta events, Figure 4.5 shows a temporal coincidence matrix indicating the percent of bursts that overlap in time (within ± 0.5 s of the peak time) and space (at the same virtual electrode) across the 3 frequency bands of interest. This matrix shows that 19% of mu events coincide with a beta event, which may help explain some of the decrease in [HbO] following the occurrence of mu events in Figure 4.4, but likely not all of it. Interestingly, 20% of gamma events also coincide with a beta event. Gamma events also show a slight decrease in [HbO] following the event, however this decrease is small compared to mu and beta events, and could reasonably be explained solely by this coincidence with beta events.

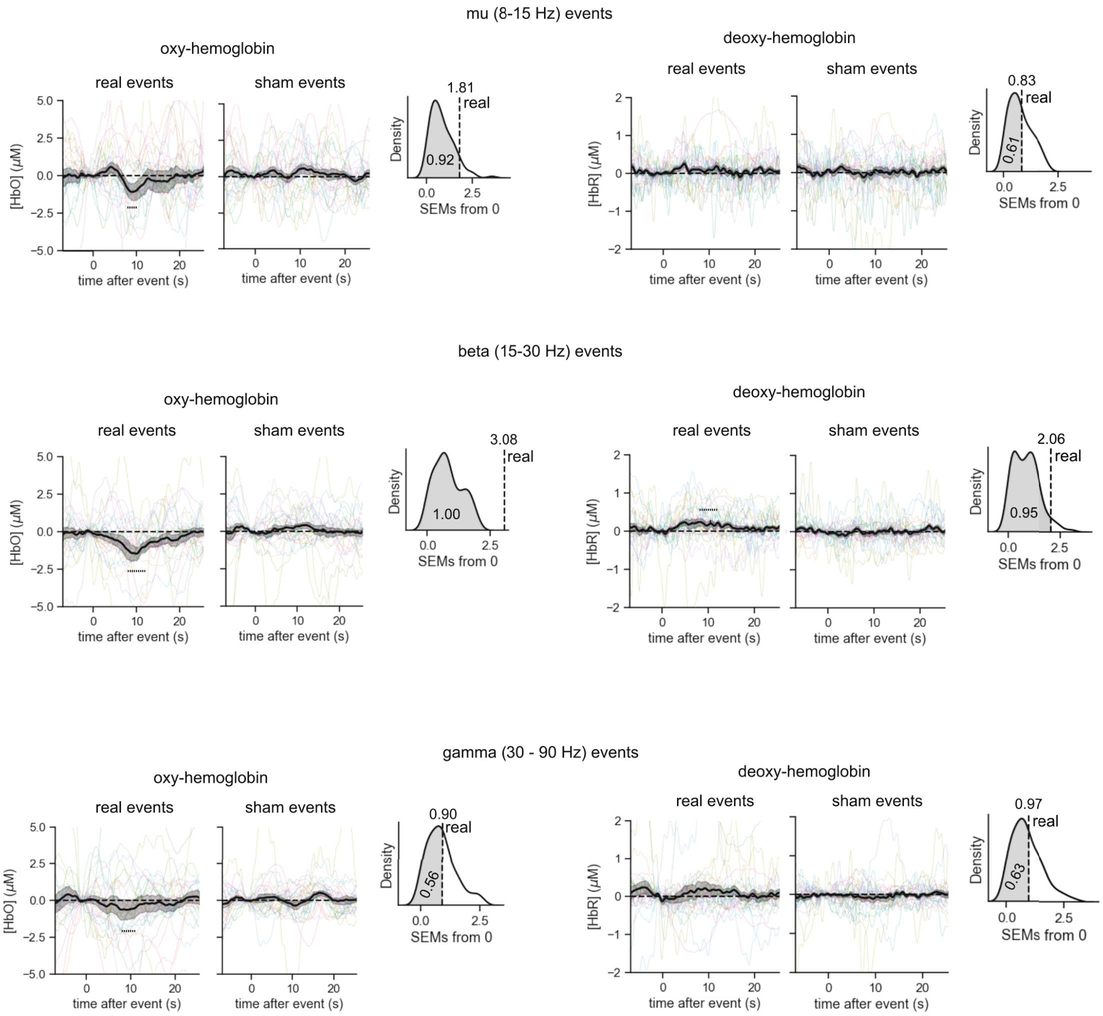

Figure 4.4: Transient burst-evoked HRFs for mu (top), beta (middle), and gamma (bottom) events. Changes in oxy-hemoglobin, [HbO], and changes in deoxy-hemoglobin, [HbR], both shown. Plots labeled as 'real events' were generated from the true sequence of transient events. Dotted lines represent time windows for statistical analysis (10-12 s for mu events, 8-12 s for beta events, 8-11 s for gamma events). Plots labeled as 'sham events' show one randomly selected sham HRF from the set of 100. The probability density plots show the distribution of sham HRF magnitudes (in terms of number of SEMs away from zero) within the time window for statistical analysis. The corresponding real HRF magnitude is shown as a vertical dashed line superimposed on the sham distribution. The fraction of the sham HRF magnitudes that are lower than the real HRF magnitude is represented by the shaded area of the distribution and indicated by the numerical label.

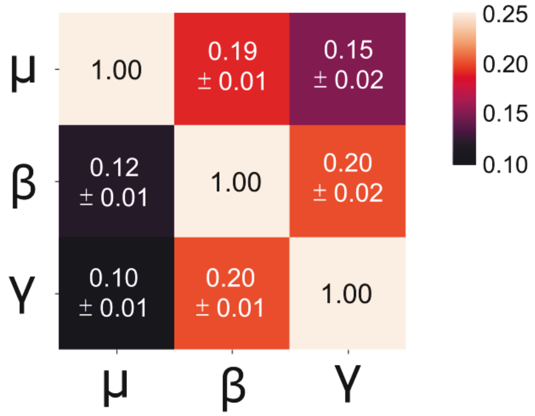

Figure 4.5: Temporal coincidence of transient events across the three frequency bands. The fraction of *y-axis* events that fall within ± 0.5 s of *x-axis* events per virtual electrode, averaged over virtual electrodes and participants. Uncertainties represent the SEM across participants.

4.4.3 Transient Burst-Evoked Neurovascular Changes During the Finger Tapping Task

Figure 4.6 (a) shows the inter-trial average changes in mu, beta, and gamma burst rate. During movement, the mu burst rate decreases by about 0.1-0.2 Hz below baseline levels ($\approx$ 15-20% drop from resting-state) while the beta burst rate decreases by about 0.5 Hz below baseline levels ($\approx$ 30% drop from resting-state). The beta burst rate rebounds to about 0.1-0.2 Hz above baseline levels ($\approx$ 5-10% above resting state) for about 2-3 s following the completion of the movement. The rebound is stronger in the right hemisphere (contralateral to movement). These observed changes in mu and beta burst rate are consistent with our previous work that found burst rate underlies mu and beta ERD and PMBR (Brady et al., 2020). No reliable changes were found in the gamma burst rate throughout the motor task.

Figure 4.6 (b) shows the inter-trial average changes in [HbO] and [HbR]. The movement induces an initial dip in [HbO] which lasts about 1 s and is larger in the right hemisphere (contralateral to movement). Following the initial dip is an overall increase in [HbO] which peaks about 7-10 s after movement onset. The [HbO] remains raised above baseline levels for about 8-10 s after movement offset and returns to baseline with the start of the next movement block. [HbR] shows a nearly opposite trend to [HbO], with approximately 20-25 % of the magnitude of [HbO]. The initial increase in [HbR] lasts substantially longer than the initial dip in [HbO] (about twice as long in the left hemisphere and about 50 % longer in the right hemisphere). There is clear contralateral dominance with larger overall neurovascular changes in the right hemisphere for both [HbO] and [HbR]. The results shown in Figure 4.6 (b) are consistent with a plethora of fNIRS and fMRI literature that shown similar neurovascular changes throughout movement tasks.

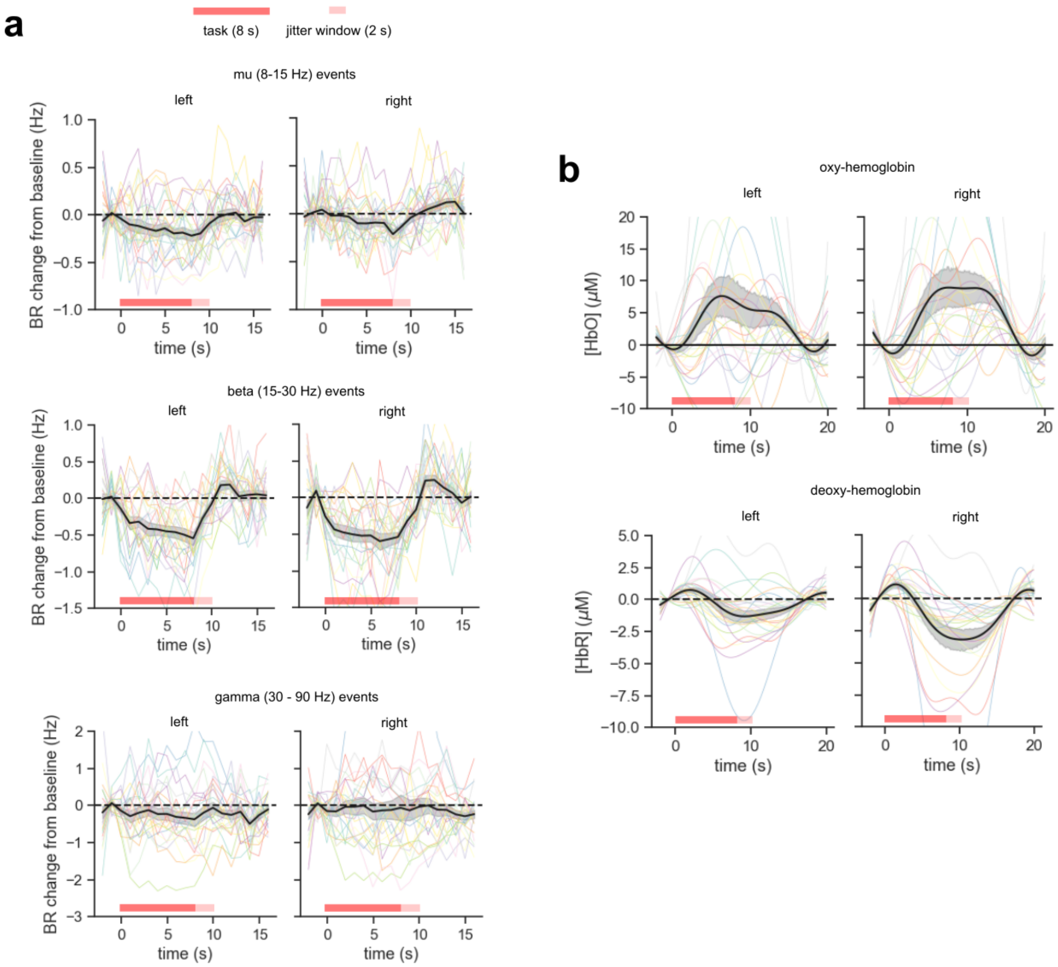

Figure 4.6: (a) Block-average mu, beta, and gamma burst rate change (see section 4.3.7 for methodological details). (b) Block-average changes in [HbO] and [HbR]. The dark red bars represent the task block (i.e., movement) and the lighter red bars represent the jitter window (see section 4.3.7). Each thin colored line is one participant. Thicker black lines represent average across participants. Shaded areas represent one SEM.

Figure 4.7 shows the inter-trial average changes in $[\text{HbO}]_{-E}$ and $[\text{HbR}]_{-E}$ ([HbO] and [HbR] subtract the hemodynamic changes evoked by transient beta events). The measured changes in [HbO] and [HbR], as shown in Figure 4.6 (b), are included for reference. Figure 4.7 shows that [HbO] and $[\text{HbO}]_{-E}$ both increase from baseline levels after movement onset and both peak at around the 6-7 s timepoint. $[\text{HbO}]_{-E}$ is higher than [HbO] during the entire movement window (0-8 s) and the peak change from baseline in $[\text{HbO}]_{-E}$ is about 1/3 higher (corresponding to about 3-4 μM) than that in [HbO]. Interestingly, $[\text{HbO}]_{-E}$ lacks the initial dip seen in [HbO], suggesting that transient beta events may be responsible for the initial dip. After movement ends, $[\text{HbO}]_{-E}$ drops to align with [HbO]. Deoxy-hemoglobin shows the opposite kind of temporal pattern to oxy-hemoglobin. [HbR] and $[\text{HbR}]_{-E}$ both increase above baseline levels for about the first 5 s of movement, after which point they both dip below baseline. [HbR] and $[\text{HbR}]_{-E}$ remain about the same for the entire movement block, however they deviate in the 10-15 s window, where $[\text{HbR}]_{-E}$ tends back towards baseline but [HbR] remains significantly below baseline.

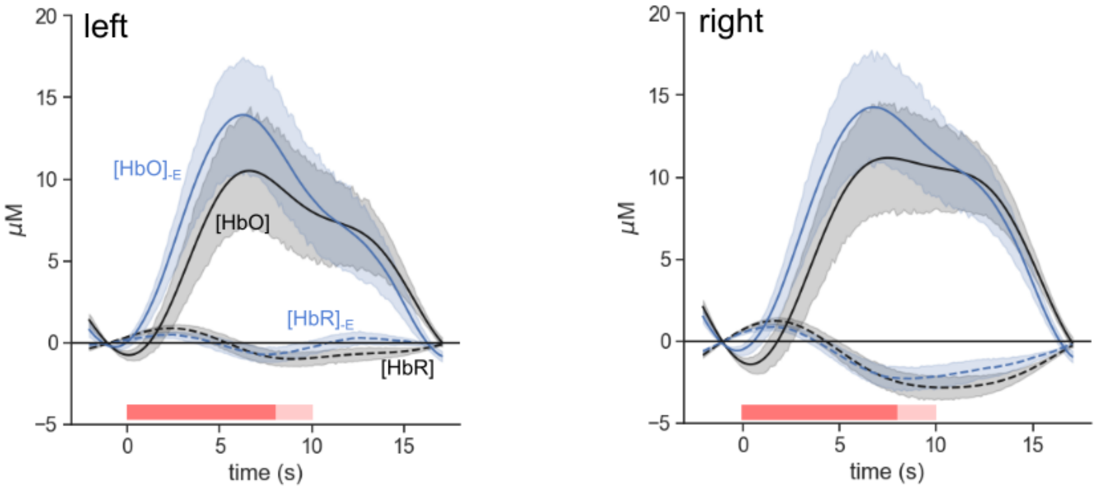

Figure 4.7: Block-average oxy- (solid) and deoxy-hemoglobin (dashed) concentration change. The black curves represent the fNIRS-measured concentrations and the blue curves represent the measured concentrations subtract the contribution of transient beta events (see section 4.3.7) Shaded regions represent one SEM across participants. The dark red bars represent the task block (i.e., movement) and the lighter red bars represent the jitter window.

Paired t-tests reveal significant differences between $[\text{HbO}]_{-E}$ and [HbO] averaged over the 0-8 s movement time widow in each hemisphere ($p = 2 \times 10^{-9}$, both hemispheres) and significant differences between $[HbR]_{-E}$ and [HbR] averaged over the 10-15 s time window in each hemisphere ($p = 2 \times 10^{-10}$, both hemispheres). Our results are thus in support of our hypothesis that neurovascular changes evoked by transient events have a non-zero contribution to the measured hemodynamic response over a unilateral motor task block design experiment. Figure 4.7 suggests that beta events primarily contribute to the overall neurovascular response by decreasing [HbO] back *towards* baseline levels during movement, and by decreasing [HbR] *further* from baseline levels in the post-movement (10-15 s) time.

We find that subtracting the hemodynamic contribution of beta events appears to remove the “initial dip” or “early response” in [HbO] prior to the onset of the compensatory hemodynamic response. Upon further analysis however, we find that this identified contribution of beta events may be misinformed due to insufficient time between task blocks to allow [HbO] and [HbR] to return to baseline levels. As shown in Figure 4.8, we convolved the grand average beta burst evoked HRF (as shown in Figure 4.4) with each participant’s block average burst rate change (Figure 4.6 a, beta). This plot shows that the [HbO] and [HbR] changes evoked from beta events take about 20-30 s after the end of the task block to return to baseline levels. This poses a problem when baselining the signal for the next task block, which starts only 8-10 s after the end of the previous task block. Thus, while we see that beta events may contribute to the ”initial dip” in our measured hemodynamic changes over the motor task, we hesitate to generalize this finding beyond this study.

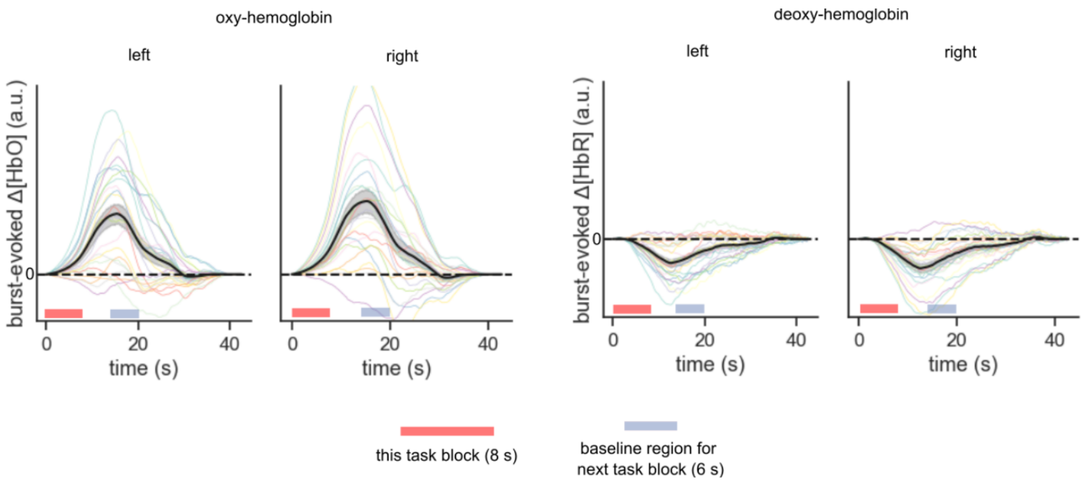

Figure 4.8: [HbO] and [HbR] changes generated by beta burst rate dynamics over one task block. Each thin colored line is the grand average real beta burst evoked HRF (Figure 4.4) convolved with the average beta burst sequence of the task block for each participant (i.e., the colored lines for beta in Figure 4.6 a). Thicker black line represents average across participants. Shaded area represents one standard error of the mean. Note that the baseline region for the next task is any consecutive 2 s segment within the indicated 6 s window (due to the jittering of the block duration).

4.5 Discussion

We report on simultaneous EEG and fNIRS measures in 26 healthy participants to investigate the hemodynamic correlates of transient oscillatory events. Using resting-state data and a conventional averaging approach, we extracted the transient burst-evoked hemodynamic response function for transient events in the mu, beta, and gamma frequency bands. We found that transient beta events evoke a significant decrease in oxy-hemoglobin concentration and increase in deoxy-hemoglobin concentration compared to a pre-event baseline, both peaking about 10 s after the burst event. No significant changes were found for mu or gamma events at the 0.05 level, although we found mu-evoked decrease in oxy-hemoglobin at the 0.1 significance level. We then used data recorded throughout a unilateral finger tapping task to evaluate the contribution of hemodynamic changes evoked by transient beta events to the overall hemodynamic changes associated with the task. While our results may point towards beta events contributing to the "initial dip" of the overall hemodynamic response, we also show that this is likely an artifact of insufficient rest time between task trials, thus pointing to an overall limitation of our experimental design. Although our interpretations are limited, we find that beta events induce dynamics in [HbO] and [HbR] at about 1/3 the magnitude of the overall task-related changes. Our results help to explicitly identify one contributing factor to spontaneous and task related changes in blood oxygenation. This work is an important step towards relating neural activity to hemodynamic signals in the healthy human brain.

4.5.1 Beta Transients Evoke a Negative Hemodynamic Effect

We found that beta events evoke a decrease in [HbO] and smaller increase in [HbR] relative to baseline levels (Figure 4.4). While it may be tempting to associate this result with a simple deoxygenation from an increase in $CMRO_2$ (akin to the initial dip in the positive BOLD response, see Introduction), two factors of the result prevent us from drawing this conclusion. First, the changes in [HbO] and [HbR] are not balanced (i.e., *equal* and opposite), which one would expect from non-compensated oxygen metabolism. Second, the changes in [HbO] and [HbR] peak about 10 s after the occurrence of the beta event. Such a peak delay is much longer than the timescale of oxygen metabolism and moreso on the timescale of the compensatory CBF mechanism in the positive BOLD response (see Introduction).

Instead, the larger decrease in [HbO] compared to the increase in [HbR] following a beta event *is* indicative of a negative BOLD response. A negative BOLD response is a stimulus/task-related decrease in the fMRI BOLD signal below pre-stimulus baseline levels. Negative BOLD responses have been observed in the human occipital (Tootell et al., 1998; Shmuel et al., 2002; Smith et al., 2004) and sensorimotor cortices (Allison et al., 2000; Klingner et al., 2010; Kastrup et al., 2008). The electrophysiological correlates of the negative BOLD response are not as well understood as the electrophysiological corelates of the positive BOLD response (described in the introduction). While several hypotheses exist to explain the origin of the negative BOLD response (ex. the *vascular steal* hypothesis (Harel et al., 2002)), the *neural inhibition* hypothesis, which describes how a reduction in CBF and $CMRO_2$ in response to either decreased excitatory activity or increased inhibitory neural activity, is one of the most supported (Sten et al., 2017; Fracasso et al., 2021; Mullinger et al., 2014) and is of particular relevance for this work. Sten et al. (2017) developed a physiological-based model of fMRI data where both excitatory and inhibitory activity affect feedforward neurovascular signaling. The model describes how the balance between glutamate and GABA release at the time of the stimulus determines the polarity (i.e., positive or negative with respect to baseline) of the BOLD response. In short, the BOLD response is positive when glutamate release is dominant while the BOLD response is negative when GABA release is dominant. Recall also that the beta transients model from Law et al. (2022) suggests that the driver of beta event generation also recruits slow (∼300 ms) inhibitory GABA synaptic currents. These models provide a possible explanation why we observe a negative hemodynamic effect after the occurrence of transient beta events. We suggest that the GABA release over the ∼300 ms timespan following the beta event determines the negative polarity of the hemodynamic response. Following from the computational model from Sten et al. (2017), the GABA recruitment post beta event decreases the inflow of Ca^{2+} to astrocytes which in turn decreases their release of vasoactive substances. The reduction in local vasoactive substances reduces blood flow and thus decreases local blood oxygenation (See Sten et al. (2017) for more details on these biochemical pathways). Thus, in combining the beta event generation model from Law et al. (2022) with the fMRI BOLD model from Sten et al. (2017), we have suggested a neuro-biological pathway that accounts for the beta event evoked oxy-hemoglobin decrease (and deoxy-hemoglobin increase) observed here (Figure 4.4).

4.5.2 No Gamma Event HRF But Maybe a Mu Event HRF

One of the central findings of this work is the frequency specificity of the transient burst evoked hemodynamic response. Namely, we found that transient beta events evoke statistically significant changes in [HbO] and [HbR] whereas no significant effects were found for transient mu or gamma events. The lack of gamma event HRF is particularly surprising given that gamma LFPs tend to correlate the closest with the BOLD signal across species (see introduction) (Logothetis et al., 2001; Mateo et al., 2017; Niessing et al., 2005; Mukamel et al., 2005; Lachaux et al., 2007). Notably, Mateo et al. (2017) found that ultra-slow fluctuations (~ 0.1 Hz) in the gamma-band power envelope entrains fluctuations in arteriole diameter in the mouse cortex, which in turn links to the BOLD signal. These gamma power envelope modulations are substantially slower than the gamma burst rate found in this work (> 2 Hz). The gamma event sequence analyzed here thus likely reflects power dynamics that are too fast to demonstrate an observable fluctuation in the hemodynamic signal in this dataset.

The hemodynamic response ([HbO] change) associated with transient mu events is not significant at the 0.05 significance level but is significant at the 0.1 significance level (Figure 3.4). While the observed mu event HRF may partially be a consequence of some temporal overlap with transient beta events (Figure 3.5), it is important to acknowledge that mu events may couple to measurable hemodynamic effects and our result lacks the SNR to report it with strong statistical power. Interestingly, Yin et al. (2016) found that (HRF-convolved) slow modulations ($\sim$ 0.5-1 Hz) in the mu oscillation amplitude envelope in the sensorimotor cortex correlate negatively with the fMRI BOLD response. Unlike the gamma events discussed above, these slow modulations *are* on the order of the mu transient burst rate found in this work ($\sim$ 0.9 Hz). It thus follows that we do observe evidence of a potential negative hemodynamic response correlated to the occurrence of transient mu events. One potential source of low SNR for the mu event HRF may stem from the mu burst rate topography shown in Figure 4.3 (b). This topography shows that the majority of mu events are detected in the most posterior electrode in each hemisphere. Thus, averaging the mu HRF over all virtual electrodes results in low SNR. As discussed below, this could be avoided using a weighted average across electrodes based on shown in Figure 4.3 (b) when calculating the HRF. This would also likely increase the SNR for beta and gamma events.

4.5.3 Next Steps

See below recommended future directions/changes that could increase the scientific impact of this work. Several of these changes were originally suggested by Dr. Jed Meltzer, the external reviewer of this thesis.

- **Deconvolution approach for looking at Δ[HbO] and Δ[HbR] across the motor task paradigm.** For the motor task paradigm, we found that the [HbO] and [HbR] time courses do not return to baseline before the start of the next task block. This is a common problem in fMRI and can be solved via a basic deconvolution approach. This could be done before and after subtracting the contribution from the beta events (i.e., re-generate Figures 4.6 b and 4.7 using deconvolution instead of conventional averaging). See AFNI's 3dDeconvolve. Deconvolution would also solve the problem with the 'jitter window' in all the trial-averaged plots.

- **Calculate the transient event evoked HRF using a weighted average across virtual electrodes.** Base the weights on the burst rate topographies as shown in Figure 4.3 (b). This may significantly increase the SNR of the mu and beta event HRFs.

- **Re-analyze EEG data using a bipolar montage.** We detected transient events using TFRs generated at 'virtual electrode' locations so that the transient events were detected at approximately the same topographical locations as the effective fNIRS sensors. These TFRs were generated by averaging TFRs of neighboring EEG electrodes. Instead, we could look at the voltage difference between the two electrodes that have the effective fNIRS channel location in between. This would result in a more spatially specific EEG signal as well, with less contribution from more distant sources.

- **Search for times of statistical significance in the burst-evoked HRFs.** In testing the statistical significance in the burst-evoked HRFs (Figure 4.4), we first identified a time-window in which the HRF appears maximal and then used that time window to test its significance via permutation testing. This may give an inflated significance compared to searching the time course in an unbiased way. Instead we could search through the timepoints of the HRF to find which deviate significantly from zero. This could be accomplished using something like the cluster analysis routines in FieldTrip that allow one to search for a significant cluster of values across multiple timepoints, sensors, and/or frequencies.

- **Better relate the burst-evoked HRFs with a more traditional analysis of BOLD signal changes with modulations in rhythm amplitude/power.** As referenced in the introduction, this work is similar to a large number of studies done with simultaneous EEG-fMRI in the 2000's, i.e. (Logothetis et al., 2001). This trend from the 2000's seems to have petered out lately, perhaps because most of the questions that that technique was ideal for have been answered. Our approach differs in two ways: (1) we look at transient events while they look at fluctuations in spectral power, and (2) we look at Δ[HbO] and Δ[HbR] while they look at the BOLD signal. Our work would become more well-rounded if we could more directly compare our results to this earlier work. This would start by expanding the introduction to include more background on why its advantageous to consider [HbO] and [HbR] separately rather than the single BOLD signal (what can [HbO] and [HbR] tell us that BOLD can't?). In terms of methods/results, we could start by cross correlating [HbO] and [HbR] time courses with fluctuations in mu, beta, and gamma rhythm power (in a similar fashion to those EEG-fMRI papers from the early 2000s). What is the time lag of the cross correlation? Does this match time lags for those EEG-fMRI papers? Does that time lag correspond to the peak in burst-evoked HRFs found in Figure 4.4 (around 10s)? In terms of discussion, now that we have a more direct comparison with these previous papers, do we learn anything new by quantifying Δ[HbO] and Δ[HbR] rather than the BOLD signal? Stress the insights that we have gained over those papers from the early 2000s?

- **Use a deconvolution-based method to extract the burst evoked HRFs**. Deconvolution-based approaches are commonly used in the functional MRI literature (Wu et al., 2021) to separate out and extract HRFs that overlap in time due to closely spaced stimuli. In this case, the ”stimuli” are the transient events, though these are more closely spaced in time (i.e., hundreds of milliseconds) compared to conventional stimuli paradigms where deconvolution methods are typically used (i.e., seconds to 10s of seconds). Further, some a priori knowledge of the functional form of the HRF is required for deconvolution methods (i.e., initial fitting parameters), which in this case can come from the HRFs obtained via conventional averaging. Note that this is likely very difficult considering how closely the transient events are in time to one another.

Chapter 5

Discussion

5.1 Summary of This Work

This thesis explores sensorimotor transient beta events in non-invasive human neurophysiological recordings in terms of how they change with movement and with healthy aging, and in terms of their coupling to neurovascular dynamics. This thesis is comprised of 3 projects:

Project 1 investigated beta burst characteristics and their age-related changes using MEG data from the Cam-CAN dataset (n=596, ages 18-88). We found that the beta burst rate is the main influencer of beta rhythm power and the predominant factor related to age-related changes in the amplitude of the induced beta rhythm responses associated with a button press task.

Project 2 presented a novel transient burst detection algorithm called the periodic/aperiodic parametrization of transient oscillations (PAPTO). We showed that PAPTO is more sensitive to neocortical transient beta rhythms compared to more conventional transient event detection algorithms and captures more variance in the resting-state occurrence rate of beta events across participants. Using PAPTO, we found an age-related increase in the sensorimotor resting-state beta burst rate in the Cam-CAN dataset.

Project 3 explored the hemodynamic changes coupled to the occurrence of transient events using simultaneous EEG-fNIRS recordings from healthy participants (n=26). We found that transient beta events evoke a significant ($p<0.05$) decrease in oxy-hemoglobin concentration and increase in deoxy-hemoglobin concentration. We also found that transient beta burst evoked hemodynamic changes contribute a significant portion to the overall measured hemodynamic changes over a motor task.

5.2 Chapter 2 and 3 Findings in the Context of the Status-Quo Hypothesis and the Basal Ganglia-Thalamo-Cortical Network

The status-quo hypothesis suggests that sensorimotor beta rhythms represent an active top-down process that maintains the existing state of the sensorimotor network by inhibiting the processing of incoming information and inhibiting unwanted movements (Engel and Fries, 2010). Changes in the sensorimotor state are driven by endogenous modulations in the sensorimotor beta rhythm power. For example, the sensorimotor beta power decreases below baseline levels to release inhibition and allow the initiation and execution of a motor plan (i.e., beta ERD in a movement state). In the post-movement state, beta rhythm power briefly increases above baseline levels (i.e., PMBR), and there is growing evidence that the PMBR is an indicator of movement outcome processing. The findings in this thesis show that the beta burst rate (number of beta events per second) is the direct influencer of beta power and that changes in the beta burst rate are evident of changes in the sensorimotor/cognitive state. Specifically, as shown in Chapter 2, changes in the beta burst rate underlie beta ERD and the PMBR. In Chapter 3, with improved sensitivity to the cortical activity emerging from the BTC network offered by PAPTO, a strong correlation between resting state beta burst rate and resting beta power is shown. Age-related changes in burst rate found in both Chapters underlie previously reported age-related changes in resting-state beta power and beta ERD/PMBR. This thesis then points to sensorimotor cortical beta bursting as a more direct expression of the active top-down process that maintains the status-quo of the sensorimotor network.

In comparing the main findings of this thesis with a recent report from Law et al. (2022), a possible thalamocortical mechanism in which the rate of cortical beta bursting modulates the state of the sensorimotor network is identified. Law et al. (2022) found that neocortical beta events in S1 may be generated in a top-down manner initiated by excitatory drive originating in nonlemniscal thalamus. They suggest that interneurons are also targeted by this excitatory drive, which recruits slow GABA inhibition and suppresses information relay throughout the cortical microcircuit. It is this inhibition via interneurons that dominates the overall behaviour of the cortical microcircuit. See Figure 1.3 for a depiction of this beta event generative mechanism in the BCT network. This finding from Law et al. (2022) aligns well with the interpretation of beta events in the context of the status-quo hypothesis presented here. At rest, a baseline beta burst rate is evident of top-down thalamic drive to sufficiently inhibit incoming sensory information and unwanted movements as to maintain the status-quo of the BCT network. In a voluntary movement state, the beta burst rate decreases below baseline levels which is evident of reduced excitatory drive to interneurons and reduced inhibition of the cortical microcircuits. This permits sensorimotor processing throughout the BCT network, allowing for activation of the thalamus via Go-pathways in the basal ganglia and ultimately the generation of efferent motor commands.

5.3 Chapter 4 Establishes a Neurophysiological Phenomenon to be Investigated Further

In Chapter 4 of this thesis, we began to investigate the correlations between cortical bursting and changes in blood oxygenation. Unlike Chapters 2 and 3, Chapter 4 describes a research direction in the developmental phase. With that said, we have already found a significant decrease in the concentration of oxy-hemoglobin and an increase in the concentration of deoxy-hemoglobin correlated to the occurrence of transient beta events. As discussed in Chapter 4, this result may suggest that the occurrence of a single transient beta event metabolizes some oxygen but not enough to initiate a compensatory hemodynamic response. An interpretation of this finding in the context of the status-quo hypothesis could be that the beta event evoked HRF is evident of a top-down control of metabolic resources available for sensorimotor processing working on slow (10s of seconds) timescale. At rest, cortical beta bursting could maintain the status-quo not only through the recruitment of GABAergic inhibition (as discussed previously), but also through the continuous suppression of local oxy-hemoglobin concentration. This could serve as an energy conservation effort, making more metabolic resources available to other parts of the brain when they aren't needed in the sensorimotor cortex. The decrease in burst rate prior to and during movement could facilitate sensorimotor processing via lifting the suppression of oxy-hemoglobin concentration, thereby making local metabolic resources available for processing. While this interpretation is purely speculative, it will be useful to keep in mind as the next steps of this research direction (discussed in Chapter 4) are explored.

5.4 Future Directions: Computational Modeling of the Age-Related Changes in Chapters 2 and 3

The results presented in this thesis stem from a direct analysis of neurophysiological signals. While this thesis takes a qualitative reasoning approach to discuss and interpret these results, the true utility of this work can be best recognized by bringing these findings into the space of computational neuroscience and quantitative systems biology, where computational models are used to describe neurophysiological processes. The underlying mechanics of these computational models are informed from experimental data like those analyzed in this thesis. Well-informed neurophysiological computational models can ultimately be used to explore the processes that underlie not only the healthy human brain but also the diseased brain, and thus be used to investigate possible therapeutic approaches before testing on human or animal participants. The proposed future research directions described below detail potential approaches to bring the results presented in this thesis to the space of computational neuroscience.

In Chapters 2 and 3, we observed age-related changes predominantly in the burst rate and peak frequency of transient beta events. In summary:

- Age-related increase in the resting-state beta burst rate (Chapter 3). Note that this is opposite to the age-related decrease in the resting-state beta burst rate observed in Chapter 2. This difference is a good example of the applicability of the PAPTO algorithm to disambiguate changes in the periodic and aperiodic activity.
- Age-related increase in the pre-movement beta burst rate (Chapter 2)
- Age-related decrease in the post-movement beta burst rate (Chapter 2)
- Age-related decrease in the movement beta burst rate (Chapter 2).
- Age-related decrease in the peak frequency of beta events (Chapters 2 & 3)

These age-related changes in sensorimotor beta event characteristics imply age-related changes in the upstream mechanisms involved in beta event generation. As discussed by Law et al. (2022), the occurrence of a somatosensory beta event is thought to be dictated by a strong distal drive to the apical dendrites of neocortical pyramidal neurons generated by a surge of excitatory inputs (i.e., a surge of driving spikes) originating from the thalamus. The surge of driving spikes is thought to last about 50 ms, giving rise to a beta frequency oscillation. An age-related change in beta burst rate may then suggest a corresponding change in the occurrence rate of this thalamic signalling (i.e., more/less frequent surges could result in higher/lower burst rate, respectively). Alternatively, an age-related change in beta burst rate could stem from a change in the fraction of surges that have sufficient amplitude to generate strong distal currents, which may be driven by changes in neural population size and/or pathway conductance. The age-related decrease of the peak frequency of beta events may originate from an increase in the temporal spread thalamic driving spikes within a single surge (i.e., an increase in the standard deviation of the surge in the time domain).

Computational modeling can be used to further investigate the origins of the observed age-related changes in beta burst characteristics. In particular, the Human Neocortical Neurosolver (HNN) (Neymotin et al., 2020) is an available software tool that simulates the electrical activity of the neocortical cells and circuits that generate the primary electrical currents underlying EEG/MEG recordings. A next step following projects 2 and 3 in this thesis could be to reproduce the observed age-related changes in beta event characteristics using the HNN. The modeling parameters used to simulate transient beta events in Law et al. (2022) (see the associated supplementary information) could be used as a starting point for this work. Note that the HNN and Law et al. (2022) came out of the same research group (the Stephanie Jones group at Brown University). Replicating the age-related changes observed in Chapters 2 and 3 would involve changing the modeling parameters of the HNN until the correct change in the current dipole is found. A reasonable approach would be to start with the parameters speculated in the paragraph above. For example, to replicate the decrease in peak frequency, one could manually change the standard deviation (measured in ms) of the distal drive, as this is one of the adjustable model parameters set in Law et al. (2022). The aim of this process would be to change the anatomical and neurophysiological modeling parameters such that the changes are realistic and can simultaneously replicate the age-related changes in all of the investigated burst characteristics (including those that show no age-related changes). If successful, this project could be a valuable addition to the growing list of work published by our group focused on investigating neurophysiological changes with healthy ageing (Bardouille and Bailey, 2019; Brady et al., 2020; Power and Bardouille, 2021; Brady and Bardouille, 2022).

5.5 Limitations of Amplitude-Thresholding Transient Events

In this work, transient events were detected as local maxima in single-trial spectrograms with signal power that exceeded a pre-defined threshold. This approach is generally referred to as an *amplitude threshold* method to define transient events. Shin et al. (2017) used an amplitude threshold calculated as a multiple of the median signal power to detect transient events when they found that the occurrence rate of transient beta events underlies tactile perception. For this reason, we employed the same method (i.e., the med-norm method) to detect transient events in Chapter 2. In Chapter 3, we show that calculating the threshold multiple based on the median power results in a loss of information about the signal which can be recovered by calculating the threshold as a multiple of the modeled aperiodic activity instead (i.e., PAPTO). We used PAPTO to detect transient events in Chapter 4.

While amplitude thresholding to detect transient events has proven fruitful in this thesis as well as in several reports in the literature (Feingold et al., 2015; Lundqvist et al., 2016; Sherman et al., 2016; Shin et al., 2017; Little et al., 2019; Power and Bardouille, 2021), the choice of the amplitude threshold will always be arbitrary and thus amplitude thresholding is a fundamentally arbitrary way to define transient events. From a biological perspective, the amplitude of a transient event reflects the size of the underlying synchronous neural population. An amplitude threshold then says that any cortical activity happening within a neural population size below a certain threshold is unimportant. Sub-threshold transient events likely contain neurophysiologically meaningful information but are ignored by amplitude thresholding methods. The amplitude thresholds used in this thesis were based on a threshold selection method from Shin et al. (2017) (described in section 3.4.7) however, admittedly, this method is somewhat circular in reasoning (i.e., the threshold is selected such that the thresholded data best matches the raw data).

Several algorithms have recently emerged in the literature that detect and characterize *transient states* in neurophysiological data. These algorithms, which include Convolutional Sparse Coding (CSC) (La Tour et al., 2018) and Hidden Markov Modeling (HMM) (Quinn et al., 2019), are generally considered to be "more sophisticated" versions of traditional amplitude thresholding-based methods. These algorithms consider transient states as repeating data segments with a characteristic timecourse (i.e., waveform), spectral composition (i.e., power spectrum), and spatial distribution (i.e., topography). Transient state detection algorithms are data-driven and thus do not rely on an arbitrary pre-specified amplitude threshold and pre-specified frequency bands. Further, these methods simultaneously consider multi-channel data rather than treating each channel independently like amplitude thresholding methods.

Transient states, as detected via detection algorithms like CSC and HMM, undoubtedly provide a more complete description of transient neurophysiological data compared to traditional *transient events* (detected by amplitude thresholding methods). It is important however to highlight that transient states and transient events are neurophysiologically different things that provide different information. A transient event is a bout of frequency-specific high-power oscillation in a particular cortical patch which represents a traditional burst of oscillatory activity. A transient state is a particular waveform, power spectrum, and topography that is found to repeat in the data. In any given analysis, one should consider whether transient events or transient states are best suited to serve that specific purpose. For example, in Chapter 4 of this thesis, where we discuss the coupling between electrophysiology and neurovasculature, it makes more sense to consider transient events because the temporal and spatial localization of transient events is necessary to correlate them to hemodynamic measures. In Chapters 2 and 3, investigating age-related changes in transient event characteristics has provided unique insight into the age-related changes in neurophysiology at the cortical micro-circuit level, however investigating age-related changes in transient states may provide more insights into overall network changes. Overall, transient states represent a new conceptualization of the transient events framework which provides a more complete description of transient neurophysiological data while requiring fewer a priori specifications. For these reasons, I expect to see many publications in the coming months/years correlating transient states and their properties to behaviour, ageing, and disease.

5.6 Limitations of a Cross-Sectional Ageing Study

The age-related changes in beta events characteristics investigated using the cross-sectional Cam-CAN dataset (Chapters 2 and 3 of this thesis) should be considered with the generic limitations of cross-sectional ageing research. Primarily, the scatterplots shown in Figures 2.4 and 3.7 show high variance. This is primarily because there are several sources of variance in these data other than participant age. For example, participant sex, handedness, etc. are all sources that may contribute to the variance seen in these scatterplots. While most of these sources of variance are likely not correlated with age (participant sex is not correlated with age, see Figure 1 in (Bardouille and Bailey, 2019)) and thus introduce only random noise into to the data, some sources of variance may in fact correlate with age. Thus, the age-related trends observed in this work may be part epiphenomenon. For example, consider the possibility that progress/improvement in dental care over the last 50 years could impact neurophysiology in an age-dependent manner. In fact, markers of poor oral health are associated with impaired cognition and higher risk of Alzheimer's disease (Merchant et al., 2022). Thus, the older participants analyzed in this work may have different neurophysiology compared to the younger participants, simply based on the differences and quality of the dental care received throughout their respective lifetimes. Contributions from epiphenomenon like this may falsely enhance or diminish the statistical significance of the age-related changes. Ultimately, due to the high variance observed, these age-related changes have little predictive power (i.e., an average burst characteristic for a participant cannot be used to predict their age). Furthermore, as discussed in more detail at the end of section 3.6.1, there is also a potential non-participation bias in the Cam-CAN dataset. In short, older individuals who are still mobile/active are more likely to participate in the study than those who are less mobile/active. This is particularly important to consider for a study of age-related changes motor-related responses as ageing is known to correlate with a decline of motor performance. It is also important to acknowledge the Cam-CAN dataset is not a representative dataset of the global human population. It was collected in Cambridge in the UK and recruited mostly local participants. The data are thus likely biased towards genetic and environmental factors specific to that part of the world. While the Cam-CAN cross-sectional dataset is an effective substrate for studying age-related changes, considering the discussed nuances of cross-sectional data, care must be taken to not overgeneralize the observed trends.

5.7 Conclusion

This thesis presents 3 projects focused on exploring sensorimotor transient bursts in healthy populations using non-invasive neuroimaging. Projects 1 and 2 show that beta burst rate is the major influencer of sensorimotor beta power and point to sensorimotor cortical beta bursting as a direct expression of an active top-down process that maintains the current state of the sensorimotor network, in line with the *status-quo* hypothesis of sensorimotor processing. This finding helps to consolidate our understanding of the role of beta rhythms in sensorimotor processing. Projects 1 and 2 also investigate age-related changes in sensorimotor beta event characteristics which are evident of age-related changes in the underlying network mechanisms and can be used to inform computational neural models. Furthermore, the PAPTO algorithm has been made open-access and is applicable in a wide variety of research contexts beyond studying age-related changes. Project 3 investigates the relationship between transient burst events and neurovasculature. Preliminary results show that transient beta events evoke a measurable change in oxy- and deoxy-hemoglobin concentration, and that these burst-evoked changes contribute significantly to the overall hemodynamic changes in response to a motor task. This work provides novel insights into the neuro-biological mechanisms surrounding the occurrence of transient events and helps to explicitly identify one contributing factor to spontaneous and task related changes in blood oxygenation. This thesis consists of several important contributions to the scientific literature all towards a better understanding of the healthy human brain.

Bibliography

Allison, J. D., Meador, K. J., Loring, D. W., Figueroa, R. E., and Wright, J. C. (2000). Functional MRI cerebral activation and deactivation during finger movement. *Neurology*, 54(1):135–142.

Asan, A. S., McIntosh, J. R., and Carmel, J. B. (2022). Targeting Sensory and Motor Integration for Recovery of Movement After CNS Injury. *Front. Neurosci.*, 15(January):1–17.

Babiloni, C., Babiloni, F., Carducci, F., Cappa, S. F., Cincotti, F., Del Percio, C., Miniussi, C., Vito Moretti, D., Rossi, S., Sosta, K., and Rossini, P. M. (2004). Human cortical rhythms during visual delayed choice reaction time tasks: A high-resolution EEG study on normal aging. *Behav. Brain Res.*, 153(1):261–271.

Bardouille, T. and Bailey, L. (2019). Evidence for age-related changes in sensorimotor neuromagnetic responses during cued button pressing in a large open-access dataset. *Neuroimage*, 193(March):25–34.

Bardouille, T., Picton, T. W., and Ross, B. (2010). Attention modulates beta oscillations during prolonged tactile stimulation. *Eur. J. Neurosci.*, 31(4):761–769.

Barone, J. and Rossiter, H. E. (2021). Understanding the Role of Sensorimotor Beta Oscillations. *Front. Syst. Neurosci.*, 15(May):1–7.

Boas, D. A., Gaudette, T., Strangman, G., Cheng, X., Marota, J. J., and Mandeville, J. B. (2001). The accuracy of near infrared spectroscopy and imaging during focal changes in cerebral hemodynamics. *Neuroimage*, 13(1):76–90.

Bowden, J. L. and McNulty, P. A. (2013). Age-related changes in cutaneous sensation in the healthy human hand. *Age (Omaha).*, 35(4):1077–1089.

Brady, B. and Bardouille, T. (2022). Periodic/Aperiodic parameterization of transient oscillations (PAPTO)–Implications for healthy ageing. *Neuroimage*, 251(September 2021):118974.

Brady, B., Power, L., and Bardouille, T. (2020). Age-related trends in neuromagnetic transient beta burst characteristics during a sensorimotor task and rest in the Cam-CAN open-access dataset. *Neuroimage*, 222(August):117245.

Briley, P. M., Liddle, E. B., Simmonite, M., Jansen, M., White, T. P., Balain, V., Palaniyappan, L., Bowtell, R., Mullinger, K. J., and Liddle, P. F. (2021). Regional Brain Correlates of Beta Bursts in Health and Psychosis: A Concurrent Electroencephalography and Functional Magnetic Resonance Imaging Study. *Biol. Psychiatry Cogn. Neurosci. Neuroimaging*, 6(12):1145–1156.

Brodoehl, S., Klingner, C., Stieglitz, K., and Witte, O. W. (2013). Age-related changes in the somatosensory processing of tactile stimulation-An fMRI study. *Behav. Brain Res.*, 238(1):259–264.

Brown, P. (2003). Oscillatory nature of human basal ganglia activity: Relationship to the pathophysiology of parkinson's disease. *Mov. Disord.*, 18(4):357–363.

Brown, P. (2007). Abnormal oscillatory synchronisation in the motor system leads to impaired movement. *Curr. Opin. Neurobiol.*, 17(6):656–664.

Brown, P., Mazzone, P., Oliviero, A., Altibrandi, M. G., Pilato, F., Tonali, P. A., and Di Lazzaro, V. (2004). Effects of stimulation of the subthalamic area on oscillatory pallidal activity in Parkinson's disease. *Exp. Neurol.*, 188(2):480–490.

Brown, P., Oliviero, A., Mazzone, P., Insola, A., Tonali, P., and Di Lazzaro, V. (2001). Dopamine dependency of oscillations between subthalamic nucleus and pallidum in Parkinson's disease. *J. Neurosci.*, 21(3):1033–1038.

Cheyne, D., Bakhtazad, L., and Gaetz, W. C. (2006). Spatiotemporal mapping of cortical activity accompanying voluntary movements using an event-related beamforming approach. *Hum. Brain Mapp.*, 27(3):213–229.

Cheyne, D., Bells, S., Ferrari, P., Gaetz, W., and Bostan, A. C. (2008). Self-paced movements induce high-frequency gamma oscillations in primary motor cortex. *Neuroimage*, 42(1):332–342.

Cheyne, D. and Ferrari, P. (2013). MEG studies of motor cortex gamma oscillations: evidence for a gamma "fingerprint" in the brain? *Front. Hum. Neurosci.*, 7:575.

Christov, M. and Dushanova, J. (2016). Functional correlates of brain aging: beta and gamma components of event-related band responses. *Acta Neurobiol. Exp. (Wars).*, 76(1689-0035):98–109.

Cole, S. and Voytek, B. (2019). Cycle-by-cycle analysis of neural oscillations. *J. Neurophysiol.*, 122(2):849–861.

Cole, S. R. and Voytek, B. (2017). Brain Oscillations and the Importance of Waveform Shape. *Trends Cogn. Sci.*, 21(2):137–149.

Crone, N., Miglioretti, D., Gordon, B., Sieracki, J., Wilson, M., Uematsu, S., and Lesser, R. (1999). Functional mapping of human sensorimotor cortex with electrocorticographic spectral analysis. I. Alpha and beta event- related desynchronization. *Brain*, 121:2271–99.

Cui, X., Bray, S., Bryant, D. M., Glover, G. H., and Reiss, A. L. (2011). NeuroImage A quantitative comparison of NIRS and fMRI across multiple cognitive tasks. *Neuroimage*, 54(4):2808–2821.

Dale, A. M., Fischl, B., and Sereno, M. I. (1999). Cortical Surface-Based Analysis: I. Segmentation and Surface Reconstruction. *Neuroimage*, 9(2):179–194.

Dale, A. M., Liu, A. K., Fischl, B. R., Buckner, R. L., Belliveau, J. W., Lewine, J. D., and Halgren, E. (2000). Heinze et ation) (Mazziotta et al., 1983; Fox and Raichle. *Neuron*, 26:55–67.

Dale, A. M. and Sereno, M. I. (1993). Improved localization of cortical activity by combining EEG and MEG with MRI cortical surface reconstruction: A linear approach. *J. Cogn. Neurosci.*, 5(2):162–176.

Dammers, J., Schiek, M., Boers, F., Silex, C., Zvyagintsev, M., Pietrzyk, U., and Mathiak, K. (2008). Integration of amplitude and phase statistics for complete artifact removal in independent components of neuromagnetic recordings. *IEEE Trans. Biomed. Eng.*, 55(10):2353–2362.

Delorme, A., Sejnowski, T., and Makeig, S. (2007). Enhanced detection of artifacts in EEG data using higher-order statistics and independent component analysis. *Neuroimage*, 34(4):1443–1449.

Delpy, D. T., Cope, M., Van Der Zee, P., Arridge, S., Wray, S., and Wyatt, J. (1988). Estimation of optical pathlength through tissue from direct time of flight measurement. *Phys. Med. Biol.*, 33(12):1433–1442.

Desikan, R. S., Ségonne, F., Fischl, B., Quinn, B. T., Dickerson, B. C., Blacker, D., Buckner, R. L., Dale, A. M., Maguire, R. P., Hyman, B. T., Albert, M. S., and Killiany, R. J. (2006). An automated labeling system for subdividing the human cerebral cortex on MRI scans into gyral based regions of interest. *Neuroimage*, 31(3):968–980.

Destrieux, C., Fischl, B., Dale, A., and Halgren, E. (2010). Automatic parcellation of human cortical gyri and sulci using standard anatomical nomenclature. *Neuroimage*, 53(1):1–15.

Donoghue, T., Haller, M., Peterson, E. J., Varma, P., Sebastian, P., Gao, R., Noto, T., Lara, A. H., Wallis, J. D., Knight, R. T., Shestyuk, A., and Voytek, B. (2020). Parameterizing neural power spectra into periodic and aperiodic components. *Nat. Neurosci.*, 23(12):1655–1665.

Engel, A. K. and Fries, P. (2010). Beta-band oscillations — signalling the status quo? *Curr. Opin. Neurobiol.*, 20(2):156–165.

Fabus, M. S., Quinn, A. J., Warnaby, C. E., and Woolrich, M. W. (2021). Automatic decomposition of electrophysiological data into distinct nonsinusoidal oscillatory modes. *J. Neurophysiol.*, 126(5):1670–1684.

Feingold, J., Gibson, D. J., Depasquale, B., and Graybiel, A. M. (2015). Bursts of beta oscillation differentiate postperformance activity in the striatum and motor cortex of monkeys performing movement tasks. *Proc. Natl. Acad. Sci. U. S. A.*, 112(44):13687–13692.

Fischl, B. and Dale, A. M. (2000). Measuring the thickness of the human cerebral cortex from magnetic resonance images. *Proc. Natl. Acad. Sci.*, 97(20):11050–11055.

Fischl, B., Liu, A., and Dale, A. M. (2001). Automated manifold surgery: constructing geometrically accurate and topologically correct models of the human cerebral cortex. *IEEE Trans. Med. Imaging*, 20(1):70–80.

Fischl, B., Salat, D. H., Busa, E., Albert, M., Dieterich, M., Haselgrove, C., van der Kouwe, A., Killiany, R., Kennedy, D., Klaveness, S., Montillo, A., Makris, N., Rosen, B., and Dale, A. M. (2002). Whole Brain Segmentation: Automated Labeling of Neuroanatomical Structures in the Human Brain. *Neuron*, 33(3):341–355.

Fischl, B., Sereno, M. I., and Dale, A. M. (1999a). Cortical Surface-Based Analysis: II: Inflation, Flattening, and a Surface-Based Coordinate System. *Neuroimage*, 9(2):195–207.

Fischl, B., Sereno, M. I., Tootell, R. B., and Dale, A. M. (1999b). High-resolution intersubject averaging and a coordinate system for the cortical surface. *Hum. Brain Mapp.*, 8(4):272–284.

Fischl, B., van der Kouwe, A., Destrieux, C., Halgren, E., Ségonne, F., Salat, D. H., Bus, E., Seidman, L. J., Goldstein, J., Kennedy, D., Caviness, V., Makris, N., Rosen, B., and Dale, A. M. (2004). Automatically Parcellating the Human Cerebral Cortex. *Cereb. Cortex*, 14(1):11–22.

Formaggio, E., Storti, S. F., Avesani, M., Cerini, R., Milanese, F., Gasparini, A., Acler, M., Pozzi Mucelli, R., Fiaschi, A., and Manganotti, P. (2008). EEG and fMRI coregistration to investigate the cortical oscillatory activities during finger movement. *Brain Topogr.*, 21(2):100–111.

Fox, P. T. and Raichle, M. E. (1986). Focal physiological uncoupling of cerebral blood flow and oxidative metabolism during somatosensory stimulation in human subjects. *Proc. Natl. Acad. Sci. U. S. A.*, 83(4):1140–1144.

Fracasso, A., Gaglianese, A., Vansteensel, M. J., Aarnoutse, E. J., Ramsey, N. F., Dumoulin, S. O., and Petridou, N. (2021). FMRI and intra-cranial electrocorticography recordings in the same human subjects reveals negative BOLD signal coupled with silenced neuronal activity. *Brain Struct. Funct.*, (0123456789).

Fransen, A. M., van Ede, F., and Maris, E. (2015). Identifying neuronal oscillations using rhythmicity. *Neuroimage*, 118:256–267.

Freeman, W. J. and Zhai, J. (2009). Simulated power spectral density (PSD) of background electrocorticogram (ECoG). *Cogn. Neurodyn.*, 3(1):97–103.

Gaetz, W. and Cheyne, D. (2006). Localization of sensorimotor cortical rhythms induced by tactile stimulation using spatially filtered MEG. *Neuroimage*, 30(3):899–908.

Gaetz, W., MacDonald, M., Cheyne, D., and Snead, O. C. (2010). Neuromagnetic imaging of movement-related cortical oscillations in children and adults: Age predicts post-movement beta rebound. *Neuroimage*, 51(2):792–807.

Gaetz, W., Rhodes, E., Bloy, L., Blaskey, L., Jackel, C. R., Brodkin, E. S., Waldman, A., Embick, D., Hall, S., and Roberts, T. P. (2020). Evaluating motor cortical oscillations and age-related change in autism spectrum disorder. *Neuroimage*, 207(March 2019):116349.

Gaetz, W. C., Cheyne, D., Rutka, J., Drake, J., Benifla, M., Strantzas, S., Widjaja, E., Holowka, S., Tovar-Spinoza, Z., Otsubo, H., and Pang, E. (2009). Presurgical localization of primary motor cortex in pediatric patients with brain lesions by the use of spatially filtered magnetoencephalography. *Neurosurgery*, 64(3):177–85.

Gao, R., Peterson, E. J., and Voytek, B. (2017). Inferring synaptic excitation/inhibition balance from field potentials. *Neuroimage*, 158(March):70–78.

Gascoyne, L. E., Brookes, M. J., Rathnaiah, M., Katshu, M. Z. U. H., Koelewijn, L., Williams, G., Kumar, J., Walters, J. T., Seedat, Z. A., Palaniyappan, L., Deakin, J. F., Singh, K. D., Liddle, P. F., and Morris, P. G. (2021). Motor-related oscillatory activity in schizophrenia according to phase of illness and clinical symptom severity. *NeuroImage Clin.*, 29(November 2020):102524.

Godde, B., Bruns, P., Wendel, V., and Trautmann, M. (2018). Effects of age and individual experiences on tactile perception over the life span in women. *Acta Psychol. (Amst).*, 190(May):135–141.

Gonçalves, S. I., De Munck, J. C., Pouwels, P. J., Schoonhoven, R., Kuijer, J. P., Maurits, N. M., Hoogduin, J. M., Van Someren, E. J., Heethaar, R. M., and Lopes Da Silva, F. H. (2006). Correlating the alpha rhythm to BOLD using simultaneous EEG/fMRI: Inter-subject variability. *Neuroimage*, 30(1):203–213.

Gramfort, A., Luessi, M., Larson, E., Engemann, D. A., Strohmeier, D., Brodbeck, C., Parkkonen, L., and Hämäläinen, M. S. (2014). MNE software for processing MEG and EEG data. *Neuroimage*, 86:446–460.

Green, E., Bennett, H., Brayne, C., Tyler, L. K., Bullmore, E. T., Calder, A. C., Cusack, R., Dalgleish, T., Duncan, J., Henson, R. N., Marslen-Wilson, W. D., Rowe, J. B., Shafto, M. A., Campbell, K., Cheung, T., Davis, S., Geerligs, L., Kievit, R., McCarrey, A., Mustafa, A., Price, D., Samu, D., Taylor, J. R., Treder, M., Tsvetanov, K., Van Belle, J., Williams, N., Bates, L., Emery, T., Erzinçlioglu, S., Gadie, A., Gerbase, S., Georgieva, S., Hanley, C., Parkin, B., Troy, D., Auer, T., Correia, M., Gao, L., Henriques, R., Allen, J., Amery, G., Amunts, L., Barcroft, A., Castle, A., Dias, C., Dowrick, J., Fair, M., Fisher, H., Goulding, A., Grewal, A., Hale, G., Hilton, A., Johnson, F., Johnston, P., Kavanagh-Williamson, T., Kwasniewska, M., McMinn, A., Norman, K., Penrose, J., Roby, F., Rowland, D., Sargeant, J., Squire, M., Stevens, B., Stoddart, A., Stone, C., Thompson, T., Yazlik, O., Barnes, D., Dixon, M., Hillman, J., Mitchell, J., Villis, L., and Matthews, F. E. (2018). Exploring patterns of response across the lifespan: The Cambridge Centre for Ageing and Neuroscience (Cam-CAN) study. *BMC Public Health*, 18(1):1–7.

Gross, J., Kujala, J., Hämäläinen, M., Timmermann, L., Schnitzler, A., and Salmelin, R. (2001). Dynamic imaging of coherent sources: Studying neural interactions in the human brain. *Proc. Natl. Acad. Sci. U. S. A.*, 98(2):694–699.

Hall, S. D., Barnes, G. R., Furlong, P. L., Seri, S., and Hillebrand, A. (2010). Neuronal network pharmacodynamics of GABAergic modulation in the human cortex determined using pharmaco-magnetoencephalography. *Hum. Brain Mapp.*, 31(4):581–594.

Hall, S. D., Stanford, I. M., Yamawaki, N., McAllister, C. J., Rönnqvist, K. C., Woodhall, G. L., and Furlong, P. L. (2011). The role of GABAergic modulation in motor function related neuronal network activity. *Neuroimage*, 56(3):1506–1510.

Hämäläinen, M., Hari, R., Ilmoniemi, R. J., Knuutila, J., and Lounasmaa, O. V. (1993). Magnetoencephalography theory, instrumentation, and applications to noninvasive studies of the working human brain. *Rev. Mod. Phys.*, 65(2):413–497.

Hämäläinen, M. S. and Ilmoniemi, R. J. (1994). Interpreting magnetic fields of the brain: minimum norm estimates. *Med. Biol. Eng. Comput.*, 32(1):35–42.

Hamalainen, M. S. and Sarvas, J. (1989). Realistic conductivity geometry model of the human head for interpretation of neuromagnetic data. *IEEE Trans. Biomed. Eng.*, 36(2):165–171.

Harel, N., Lee, S. P., Nagaoka, T., Kim, D. S., and Kim, S. G. (2002). Origin of negative blood oxygenation level-dependent fMRI signals. *J. Cereb. Blood Flow Metab.*, 22(8):908–917.

Hari, R., Salmelin, R., Mäkelä, J., Salenius, S., and Helle, M. (1997). Magnetoencephalographic cortical rhythms. *Int. J. Psychophysiol.*, 26(1-3):51–62.

He, B. J., Zempel, J. M., Snyder, A. Z., and Raichle, M. E. (2010). The temporal structures and functional significance of scale-free brain activity. *Neuron*, 66(3):353–369.

He, W., Donoghue, T., Sowman, P. F., Seymour, R. A., Brock, J., Crain, S., Voytek, B., and Hillebrand, A. (2019). Co-increasing neuronal noise and beta power in the developing brain. *bioRxiv*, 61(02):1–49.

Heideman, S. G., Quinn, A. J., Woolrich, M. W., van Ede, F., and Nobre, A. C. (2020). Dissecting beta-state changes during timed movement preparation in Parkinson's disease. *Prog. Neurobiol.*, 184(November 2019):101731.

Heinrichs-Graham, E. and Wilson, T. W. (2016). Is an absolute level of cortical beta suppression required for proper movement? Magnetoencephalographic evidence from healthy aging. *Neuroimage*, 134:514–521.

Hu, X. and Yacoub, E. (2012). The story of the initial dip in fMRI. *Neuroimage*, 62(2):1103–1108.

Hutchinson, S., Kobayashi, M., Horkan, C., Pascual-Leone, A., Alexander, M., and Schlaug, G. (2002). Age-Related Differences in Movement Representation. *Neuroimage*, 17(4):1720–1728.

Hyvärinen, A. (1999). Fast and robust fixed-point algorithms for independent component analysis. *IEEE Trans. Neural Networks*, 10(3):626–634.

Jas, M., La Tour, T. D., Şimşekli, U., and Gramfort, A. (2017). Learning the morphology of brain signals using alpha-stable convolutional sparse coding. *Adv. Neural Inf. Process. Syst.*, 2017-Decem(Nips):1100–1109.

Jasdzewski, G., Strangman, G., Wagner, J., Kwong, K. K., Poldrack, R. A., and Boas, D. A. (2003). Differences in the hemodynamic response to event-related motor and visual paradigms as measured by near-infrared spectroscopy. *Neuroimage*, 20(1):479–488.

Jensen, O., Goel, P., Kopell, N., Pohja, M., Hari, R., and Ermentrout, B. (2005). On the human sensorimotor-cortex beta rhythm: Sources and modeling. *Neuroimage*, 26(2):347–355.

Jones, S. R. (2016). When brain rhythms aren't 'rhythmic': implication for their mechanisms and meaning. *Curr. Opin. Neurobiol.*, 40:72–80.

Jones, S. R., Kerr, C. E., Wan, Q., Pritchett, D. L., Hämäläinen, M., and Moore, C. I. (2010). Cued spatial attention drives functionally relevant modulation of the mu rhythm in primary somatosensory cortex. *J. Neurosci.*, 30(41):13760–13765.

Jurkiewicz, M. T., Gaetz, W. C., Bostan, A. C., and Cheyne, D. (2006). Post-movement beta rebound is generated in motor cortex: Evidence from neuromagnetic recordings. *Neuroimage*, 32(3):1281–1289.

Kalisch, T., Ragert, P., Schwenkreis, P., Dinse, H. R., and Tegenthoff, M. (2009). Impaired tactile acuity in old age is accompanied by enlarged hand representations in somatosensory cortex. *Cereb. Cortex*, 19(7):1530–1538.

Kastrup, A., Baudewig, J., Schnaudigel, S., Huonker, R., Becker, L., Sohns, J. M., Dechent, P., Klingner, C., and Witte, O. W. (2008). Behavioral correlates of negative BOLD signal changes in the primary somatosensory cortex. *Neuroimage*, 41(4):1364–1371.

Klingner, C. M., Hasler, C., Brodoehl, S., and Witte, O. W. (2010). Dependence of the negative BOLD response on somatosensory stimulus intensity. *Neuroimage*, 53(1):189–195.

Kosciessa, J. Q., Grandy, T. H., Garrett, D. D., and Werkle-Bergner, M. (2020). Single-trial characterization of neural rhythms: Potential and challenges. *Neuroimage*, 206(September 2019):116331.

La Tour, T. D., Moreau, T., Jas, M., and Gramfort, A. (2018). Multivariate convolutional sparse coding for electromagnetic brain signals. In *32nd Int. Conf. Neural Inf. Process. Syst.*, pages 3296–3306.

Labyt, E., Szurhaj, W., Bourriez, J.-L., Cassim, F., Defebvre, L., Destée, A., Guieu, J.-D., and Derambure, P. (2003). Changes in oscillatory cortical activity related to a visuomotor task in young and elderly healthy subjects. *Clin. Neurophysiol.*, 114(6):1153–1166.

Lachaux, J. P., Fonlupt, P., Kahane, P., Minotti, L., Hoffmann, D., Bertrand, O., and Baciu, M. (2007). Relationship between task-related gamma oscillations and BOLD Signal: New insights from combined fMRI and intracranial EEG. *Hum. Brain Mapp.*, 28(12):1368–1375.

Lachert, P., Janusek, D., Pulawski, P., Liebert, A., Milej, D., and Blinowska, K. J. (2017). Coupling of Oxy- and Deoxyhemoglobin concentrations with EEG rhythms during motor task. *Sci. Rep.*, 7(1):1–9.

Laufs, H., Kleinschmidt, A., Beyerle, A., Eger, E., Salek-Haddadi, A., Preibisch, C., and Krakow, K. (2003). EEG-correlated fMRI of human alpha activity. *Neuroimage*, 19(4):1463–1476.

Law, R. G., Pugliese, S., Shin, H., Sliva, D. D., Lee, S., Neymotin, S., Moore, C., and Jones, S. R. (2021). Thalamocortical Mechanisms Regulating the Relationship between Transient Beta Events and Human Tactile Perception. *Cereb. Cortex*, pages 1–21.

Law, R. G., Pugliese, S., Shin, H., Sliva, D. D., Lee, S., Neymotin, S., Moore, C., and Jones, S. R. (2022). Thalamocortical Mechanisms Regulating the Relationship between Transient Beta Events and Human Tactile Perception. *Cereb. Cortex*, 32(4):668–688.

Lenz, M., Tegenthoff, M., Kohlhaas, K., Stude, P., Höffken, O., Tossi, M. A., Kalisch, T., and Dinse, H. R. (2012). Increased excitability of somatosensory cortex in aged humans is associated with impaired tactile acuity. *J. Neurosci.*, 32(5):1811–1816.

Lin, F. H., Witzel, T., Ahlfors, S. P., Stufflebeam, S. M., Belliveau, J. W., and Hämäläinen, M. S. (2006). Assessing and improving the spatial accuracy in MEG source localization by depth-weighted minimum-norm estimates. *Neuroimage*, 31(1):160–171.

Little, S., Bonaiuto, J., Barnes, G., and Bestmann, S. (2019). Human motor cortical beta bursts relate to movement planning and response errors. *PLoS Biol.*, 17(10):1–30.

Little, S. and Brown, P. (2014). The functional role of beta oscillations in Parkinson's disease. *Parkinsonism Relat. Disord.*, 20:S44–S48.

Logothetis, N. K., Pauls, J., Augath, M., Trinath, T., and Oeltermann, A. (2001). Neurophysiological investigation of the basis of the fMRI signal. *Nature*, 412(6843):150–157.

Lundqvist, M., Herman, P., Warden, M. R., Brincat, S. L., and Miller, E. K. (2018). Gamma and beta bursts during working memory readout suggest roles in its volitional control. *Nat. Commun.*, 9(1):1–12.

Lundqvist, M., Rose, J., Herman, P., Brincat, S. L., Buschman, T. J., and Miller, E. K. (2016). Gamma and Beta Bursts Underlie Working Memory. *Neuron*, 90(1):152–164.

Manning, J. R., Jacobs, J., Fried, I., and Kahana, M. J. (2009). Broadband shifts in local field potential power spectra are correlated with single-neuron spiking in humans. *J. Neurosci.*, 29(43):13613–13620.

Manual, U. (2014). NIRStar™ 15.2 User Manual.

Mary, A., Bourguignon, M., Wens, V., Op de Beeck, M., Leproult, R., De Tiège, X., and Peigneux, P. (2015). Aging reduces experience-induced sensorimotor plasticity. A magnetoencephalographic study. *Neuroimage*, 104:59–68.

Mateo, C., Knutsen, P. M., Tsai, P. S., Shih, A. Y., and Kleinfeld, D. (2017). Entrainment of Arteriole Vasomotor Fluctuations by Neural Activity Is a Basis of Blood-Oxygenation-Level-Dependent "Resting-State" Connectivity. *Neuron*, 96(4):936–948.e3.

Mello, L. E. and Villares, J. (1997). Neuroanatomy of the basal ganglia. *Psychiatr. Clin. North Am.*, 20(4):691–704.

Merchant, A. T., Yi, F., Vidanapathirana, N. P., Lohman, M., Zhang, J., Newman-Norlund, R. D., and Fridriksson, J. (2022). Antibodies against Periodontal Microorganisms and Cognition in Older Adults. *JDR Clin. Transl. Res.*, XX(X):1–10.

Milikovsky, D. Z., Ofer, J., Senatorov, V. V., Friedman, A. R., Prager, O., Sheintuch, L., Elazari, N., Veksler, R., Zelig, D., Weissberg, I., Bar-Klein, G., Swissa, E., Hanael, E., Ben-Arie, G., Schefenbauer, O., Kamintsky, L., Saar-Ashkenazy, R., Shelef, I., Shamir, M. H., Goldberg, I., Glik, A., Benninger, F., Kaufer, D., and Friedman, A. (2019). Paroxysmal slow cortical activity in Alzheimer's disease and epilepsy is associated with blood-brain barrier dysfunction. *Sci. Transl. Med.*, 11(521):1–12.

Miller, K. J., Schalk, G., Fetz, E. E., Den Nijs, M., Ojemann, J. G., and Rao, R. P. (2010). Cortical activity during motor execution, motor imagery, and imagery-based online feedback. *Proc. Natl. Acad. Sci. U. S. A.*, 107(9):4430–4435.

Moosmann, M., Ritter, P., Krastel, I., Brink, A., Thees, S., Blankenburg, F., Taskin, B., Obrig, H., and Villringer, A. (2003). Correlates of alpha rhythm in functional magnetic resonance imaging and near infrared spectroscopy. *Neuroimage*, 20(1):145–158.

Mukamel, R., Gelbard, H., Arieli, A., Hasson, U., Fried, I., and Malach, R. (2005). Neuroscience: Coupling between neuronal firing, field potentials, and fMRI in human auditory cortex. *Science (80-.).*, 309(5736):951–954.

Mullinger, K. J., Cherukara, M. T., Buxton, R. B., Francis, S. T., and Mayhew, S. D. (2017). Post-stimulus fMRI and EEG responses: Evidence for a neuronal origin hypothesised to be inhibitory. *Neuroimage*, 157(June):388–399.

Mullinger, K. J., Mayhew, S. D., Bagshaw, A. P., Bowtell, R., and Francis, S. T. (2013). Poststimulus undershoots in cerebral blood flow and BOLD fMRI responses are modulated by poststimulus neuronal activity. *Proc. Natl. Acad. Sci. U. S. A.*, 110(33):13636–13641.

Mullinger, K. J., Mayhew, S. D., Bagshaw, A. P., Bowtell, R., and Francis, S. T. (2014). Evidence that the negative BOLD response is neuronal in origin: A simultaneous EEG-BOLD-CBF study in humans. *Neuroimage*, 94:263–274.

Münchau, A., Colzato, L. S., AghajaniAfjedi, A., and Beste, C. (2021). A neural noise account of Gilles de la Tourette syndrome. *NeuroImage Clin.*, 30:102654.

Murthy, V. N. and Fetz, E. E. (1992). Coherent 25- to 35-Hz oscillations in the sensorimotor cortex of awake behaving monkeys. *Proc. Natl. Acad. Sci.*, 89(12):5670–5674.

Muthukumaraswamy, S. D. (2010). Functional properties of human primary motor cortex gamma oscillations. *J. Neurophysiol.*, 104(5):2873–2885.

Muthukumaraswamy, S. D. (2011). Temporal dynamics of primary motor cortex gamma oscillation amplitude and piper corticomuscular coherence changes during motor control. *Exp. Brain Res.*, 212(4):623–633.

Muthukumaraswamy, S. D., Myers, J. F., Wilson, S. J., Nutt, D. J., Lingford-Hughes, A., Singh, K. D., and Hamandi, K. (2013). The effects of elevated endogenous GABA levels on movement-related network oscillations. *Neuroimage*, 66:36–41.

Neymotin, S. A., Daniels, D. S., Caldwell, B., McDougal, R. A., Carnevale, N. T., Jas, M., Moore, C. I., Hines, M. L., Hämäläinen, M., and Jones, S. R. (2020). Human neocortical neurosolver (HNN), a new software tool for interpreting the cellular and network origin of human MEG/EEG data. *Elife*, 9:1–39.

Niessing, J., Ebisch, B., Schmidt, K. E., Niessing, M., Singer, W., and Galuske, R. A. (2005). Neuroscience: Hemodynamic signals correlate tightly with synchronized gamma oscillations. *Science (80-.).*, 309(5736):948–951.

Ogawa, S., Lee, T. M., and Kay, A. R. (1990). Brain magnetic resonance imaging with contrast dependent on blood oxygenation. 87(December):9868–9872.

Ostlund, B. D., Alperin, B. R., Drew, T., and Karalunas, S. L. (2021). Behavioral and cognitive correlates of the aperiodic (1/f-like) exponent of the EEG power spectrum in adolescents with and without ADHD. *Dev. Cogn. Neurosci.*, 48:100931.

Ouyang, G., Hildebrandt, A., Schmitz, F., and Herrmann, C. S. (2020). Decomposing alpha and 1/f brain activities reveals their differential associations with cognitive processing speed. *Neuroimage*, 205(October 2019):116304.

Parkkonen, E., Laaksonen, K., Piitulainen, H., Parkkonen, L., and Forss, N. (2015). Modulation of the ˜20-Hz motor-cortex rhythm to passive movement and tactile stimulation. *Brain Behav.*, 5(5):1–11.

Patil, A. V., Safaie, J., Moghaddam, H. A., Wallois, F., and Grebe, R. (2011). Experimental investigation of NIRS spatial sensitivity. *Biomed. Opt. Express*, 2(6):1478.

Pfurtscheller, G. and Aranibar, A. (1977). Event-related cortical desynchronization detected by power measurements of scalp EEG. *Electroencephalogr. Clin. Neurophysiol.*, 42(6):817–826.

Pfurtscheller, G., Flotzinger, D., and Neuper, C. (1994). Differentiation between finger, toe and tongue movement in man based on 40 Hz EEG. *Electroencephalogr. Clin. Neurophysiol.*, 90(6):456–460.

Pfurtscheller, G. and Lopes da Silva, F. (1999). Event-related EEG/MEG synchronization and desynchronization: basic principles. *Clin. Neurophysiol.*, 110(11):1842–1857.

Pfurtscheller, G., Neuper, C., Andrew, C., and Edlinger, G. (1997). Foot and hand area mu rhythms. *Int. J. Psychophysiol.*, 26(1-3):121–135.

Pfurtscheller, G., Stancák, A., and Neuper, C. (1996). Post-movement beta synchronization. A correlate of an idling motor area? *Electroencephalogr. Clin. Neurophysiol.*, 98(4):281–293.

Pleger, B., Wilimzig, C., Nicolas, V., Kalisch, T., Ragert, P., Tegenthoff, M., and Dinse, H. R. (2016). A complementary role of intracortical inhibition in age-related tactile degradation and its remodelling in humans. *Sci. Rep.*, 6(June):1–15.

Podvalny, E., Noy, N., Harel, M., Bickel, S., Chechik, G., Schroeder, C. E., Mehta, A. D., Tsodyks, M., and Malach, R. (2015). A unifying principle underlying the extracellular field potential spectral responses in the human cortex. *J. Neurophysiol.*, 114(1):505–519.

Pollonini, L., Olds, C., Abaya, H., Bortfeld, H., Beauchamp, M. S., and Oghalai, J. S. (2014). Auditory cortex activation to natural speech and simulated cochlear implant speech measured with functional near-infrared spectroscopy. *Hear. Res.*, 309:84–93.

Power, L. and Bardouille, T. (2021). Age-related trends in the cortical sources of transient beta bursts during a sensorimotor task and rest. *Neuroimage*, 245(October):118670.

Quaresima, V. and Ferrari, M. (2019). Functional Near-Infrared Spectroscopy (fNIRS) for Assessing Cerebral Cortex Function During Human Behavior in Natural/Social Situations: A Concise Review. *Organ. Res. Methods*, 22(1):46–68.

Quinn, A. J., van Ede, F., Brookes, M. J., Heideman, S. G., Nowak, M., Seedat, Z. A., Vidaurre, D., Zich, C., Nobre, A. C., and Woolrich, M. W. (2019). Unpacking Transient Event Dynamics in Electrophysiological Power Spectra. *Brain Topogr.*, 32(6):1020–1034.

R. Goldman, J. Stern, J. Engel, M. C. (2002). Simultaneous EEG and fMRI of the alpha rhythm. *Neuroreport*, 13(18):2487–2492.

Racz, F. S., Farkas, K., Stylianou, O., Kaposzta, Z., Czoch, A., Mukli, P., Csukly, G., and Eke, A. (2021). Separating scale-free and oscillatory components of neural activity in schizophrenia. *Brain Behav.*, 11(5):1–15.

Ritter, P., Moosmann, M., and Villringer, A. (2009). Rolandic alpha and beta EEG rhythms' strengths are inversely related to fMRI-BOLD signal in primary somatosensory and motor cortex. *Hum. Brain Mapp.*, 30(4):1168–1187.

Robertson, M. M., Furlong, S., Voytek, B., Donoghue, T., Boettiger, C. A., and Sheridan, M. A. (2019). EEG power spectral slope differs by ADHD status and stimulant medication exposure in early childhood. *J. Neurophysiol.*, 122(6):2427–2437.

Rossini, P. M., Rossi, S., Babiloni, C., and Polich, J. (2007). Clinical neurophysiology of aging brain: From normal aging to neurodegeneration. *Prog. Neurobiol.*, 83(6):375–400.

Rossiter, H., Boudrias, M., and Ward, N. (2014a). Do movement-related beta oscillations change after stroke? *J. Neurophysiol.*, 112(9):2053–2058.

Rossiter, H. E., Davis, E. M., Clark, E. V., Boudrias, M.-H., and Ward, N. S. (2014b). Beta oscillations reflect changes in motor cortex inhibition in healthy ageing. *Neuroimage*, 91:360–365.

Sabbagh, D., Ablin, P., Varoquaux, G., Gramfort, A., and Engemann, D. A. (2019). Manifold-regression to predict from MEG/EEG brain signals without source modeling. *Adv. Neural Inf. Process. Syst.*, 32(NeurIPS).

Sallard, E., Tallet, J., Thut, G., Deiber, M.-P., and Barral, J. (2016). Age-related changes in post-movement beta synchronization during a selective inhibition task. *Exp. Brain Res.*, 234.

Salman, H., Grover, J., and Shankar, T. (2018). Hierarchical Reinforcement Learning for Sequencing Behaviors. 2733(March):2709–2733.

Schmiedt-Fehr, C., Mathes, B., Kedilaya, S., Krauss, J., and Basar-Eroglu, C. (2016). Aging differentially affects alpha and beta sensorimotor rhythms in a go/nogo task. *Clin. Neurophysiol.*, 127(10):3234–3242.

Scholkmann, F., Kleiser, S., Metz, A. J., Zimmermann, R., Mata Pavia, J., Wolf, U., and Wolf, M. (2014). A review on continuous wave functional near-infrared spectroscopy and imaging instrumentation and methodology. *Neuroimage*, 85:6–27.

Schroeter, M. L., Kupka, T., Mildner, T., Uludağ, K., and Von Cramon, D. Y. (2006). Investigating the post-stimulus undershoot of the BOLD signal - A simultaneous fMRI and fNIRS study. *Neuroimage*, 30(2):349–358.

Seedat, Z. A., Quinn, A. J., Vidaurre, D., Liuzzi, L., Gascoyne, L. E., Hunt, B. A., O'Neill, G. C., Pakenham, D. O., Mullinger, K. J., Morris, P. G., Woolrich, M. W., and Brookes, M. J. (2020). The role of transient spectral 'bursts' in functional connectivity: A magnetoencephalography study. *Neuroimage*, 209(December 2019):116537.

Sekihara, K. and Nagarajan, S. (2008). *Adaptive Spatial Filters for Electromagnetic Brain Imaging.* Springer US.

Shafto, M., Tyler, L., Dixon, M., Taylor, J., Rowe, J., Cusack, R., Calder, A., Marslen-Wilson, W., Duncan, J., Dalgleish, T., Henson, R., Brayne, C., and Matthews, F. (2014). The Cambridge Centre for Ageing and Neuroscience (Cam-CAN) study protocol: a cross-sectional, lifespan, multidisciplinary examination of healthy cognitive ageing. *BMC Neurol.*, 14(204).

Sherman, M. A., Lee, S., Law, R., Haegens, S., Thorn, C. A., Hämäläinen, M. S., Moore, C. I., and Jones, S. R. (2016). Neural mechanisms of transient neocortical beta rhythms: Converging evidence from humans, computational modeling, monkeys, and mice. *Proc. Natl. Acad. Sci. U. S. A.*, 113(33):E4885–E4894.

Shin, H., Law, R., Tsutsui, S., Moore, C. I., and Jones, S. R. (2017). The rate of transient beta frequency events predicts behavior across tasks and species. *Elife*, 6.

Shmuel, A., Yacoub, E., Pfeuffer, J., Van de Moortele, P. F., Adriany, G., Hu, X., and Ugurbil, K. (2002). Sustained negative BOLD, blood flow and oxygen consumption response and its coupling to the positive response in the human brain. *Neuron*, 36(6):1195–1210.

Siegel, M., Donner, T. H., Oostenveld, R., Fries, P., and Engel, A. K. (2008). Neuronal Synchronization along the Dorsal Visual Pathway Reflects the Focus of Spatial Attention. *Neuron*, 60(4):709–719.

Smith, A. T., Williams, A. L., and Singh, K. D. (2004). Negative BOLD in the Visual Cortex: Evidence Against Blood Stealing. *Hum. Brain Mapp.*, 21(4):213–220.

Soares, J. M., Magalhães, R., Moreira, P. S., Sousa, A., Ganz, E., Sampaio, A., Alves, V., Marques, P., and Sousa, N. (2016). A Hitchhiker's guide to functional magnetic resonance imaging. *Front. Neurosci.*, 10(November):1–35.

Sten, S., Lundengård, K., Witt, S. T., Cedersund, G., Elinder, F., and Engström, M. (2017). Neural inhibition can explain negative BOLD responses: A mechanistic modelling and fMRI study. *Neuroimage*, 158(April):219–231.

Stevenson, C. M., Brookes, M. J., and Morris, P. G. (2011). β-Band correlates of the fMRI BOLD response. *Hum. Brain Mapp.*, 32(2):182–197.

Strangman, G., Franceschini, M. A., and Boas, D. A. (2003). Factors affecting the accuracy of near-infrared spectroscopy concentration calculations for focal changes in oxygenation parameters. *Neuroimage*, 18(4):865–879.

Tallon-Baudry, C., Bertrand, O., Delpuech, C., and Pernier, J. (1997). Oscillatory γ-band (30-70 Hz) activity induced by a visual search task in humans. *J. Neurosci.*, 17(2):722–734.

Taulu, S. and Simola, J. (2006). Spatiotemporal signal space separation method for rejecting nearby interference in MEG measurements. *Phys. Med. Biol.*, 51(7):1759–1768.

Taylor, J. R., Williams, N., Cusack, R., Auer, T., Shafto, M. A., Dixon, M., Tyler, L. K., Cam-CAN, and Henson, R. N. (2017). The Cambridge Centre for Ageing and Neuroscience (Cam-CAN) data repository: Structural and functional MRI, MEG, and cognitive data from a cross-sectional adult lifespan sample. *Neuroimage*, 144:262–269.

Thibaut, A., Simis, M., Battistella, L. R., Fanciullacci, C., Bertolucci, F., Huerta-Gutierrez, R., Chisari, C., and Fregni, F. (2017). Using brain oscillations and corticospinal excitability to understand and predict post-stroke motor function. *Front. Neurol.*, 8(MAY):1–8.

Thuwal, K., Banerjee, A., and Roy, D. (2021). Aperiodic and Periodic Components of Ongoing Oscillatory Brain Dynamics Link Distinct Functional Aspects of Cognition across Adult Lifespan. *eNeuro*, 8(5).

Tinkhauser, G., Pogosyan, A., Little, S., Beudel, M., Herz, D. M., Tan, H., and Brown, P. (2017). The modulatory effect of adaptive deep brain stimulation on beta bursts in Parkinson's disease. *Brain*, 140(4):1053–1067.

Toledo, D. R., Barela, J. A., Manzano, G. M., and Kohn, A. F. (2016). Age-related differences in EEG beta activity during an assessment of ankle proprioception. *Neurosci. Lett.*, 622:1–5.

Tootell, R. B., Mendola, J. D., Hadjikhani, N. K., Liu, A. K., and Dale, A. M. (1998). The representation of the ipsilateral visual field in human cerebral cortex. *Proc. Natl. Acad. Sci. U. S. A.*, 95(3):818–824.

Tsuchimoto, S., Shibusawa, S., Mizuguchi, N., Kato, K., Ebata, H., Liu, M., Hanakawa, T., and Ushiba, J. (2017). Resting-state fluctuations of EEG sensorimotor rhythm reflect BOLD activities in the pericentral areas: A simultaneous EEG-fMRI study. *Front. Hum. Neurosci.*, 11(July):1–10.

van Ede, F., Quinn, A. J., Woolrich, M. W., and Nobre, A. C. (2018). Neural Oscillations: Sustained Rhythms or Transient Burst-Events? *Trends Neurosci.*, 41(7):415–417.

Van Veen, B. D., Van Drongelen, W., Yuchtman, M., and Suzuki, A. (1997). Localization of brain electrical activity via linearly constrained minimum variance spatial filtering. *IEEE Trans. Biomed. Eng.*, 44(9):867–880.

van Zijl, P. C., Hua, J., and Lu, H. (2012). The BOLD post-stimulus undershoot, one of the most debated issues in fMRI. *Neuroimage*, 62(2):1092–1102.

Voytek, B., Kramer, M. A., Case, J., Lepage, K. Q., Tempesta, Z. R., Knight, R. T., and Gazzaley, A. (2015). Age-related changes in 1/f neural electrophysiological noise. *J. Neurosci.*, 35(38):13257–13265.

Watrous, A. J., Miller, J., Qasim, S. E., Fried, I., and Jacobs, J. (2018). Phase-tuned neuronal firing encodes human contextual representations for navigational goals. *Elife*, 7:1–16.

Whitten, T. A., Hughes, A. M., Dickson, C. T., and Caplan, J. B. (2011). A better oscillation detection method robustly extracts EEG rhythms across brain state changes: The human alpha rhythm as a test case. *Neuroimage*, 54(2):860–874.

Wickremaratchi, M. M. and Llewelyn, J. G. (2006). Effects of ageing on touch. *Postgrad. Med. J.*, 82(967):301–304.

Wilson, T. W., Slason, E., Asherin, R., Kronberg, E., Reite, M. L., Teale, P. D., and Rojas, D. C. (2010). An extended motor network generates beta and gamma oscillatory perturbations during development. *Brain Cogn.*, 73(2):75–84.

Wu, G. R., Colenbier, N., Van Den Bossche, S., Clauw, K., Johri, A., Tandon, M., and Marinazzo, D. (2021). rsHRF: A toolbox for resting-state HRF estimation and deconvolution. *Neuroimage*, 244(September):118591.

Wyatt, J. S., Delpy, D. T., Cope, M., Wray, S., and Reynolds, E. O. (1986). Quantification of Cerebral Oxygenation and Haemodynamics in Sick Newborn Infants By Near Infrared Spectrophotometry. *Lancet*, 328(8515):1063–1066.

Yin, S., Liu, Y., and Ding, M. (2016). Amplitude of Sensorimotor Mu Rhythm Is Correlated with BOLD from Multiple Brain Regions: A Simultaneous EEG-fMRI Study. *Front. Hum. Neurosci.*, 10(July):1–12.

Yuan, H., Liu, T., Szarkowski, R., Rios, C., Ashe, J., and He, B. (2010). Negative covariation between task-related responses in alpha/beta-band activity and BOLD in human sensorimotor cortex: An EEG and fMRI study of motor imagery and movements. *Neuroimage*, 49(3):2596–2606.

Appendices

Appendix A: Chapter 2 Supplementary Information

Figure A.1 shows age-related changes in beta burst characteristics for each phase of the button press response and for the resting state for the sensor ROI analysis method. Table A.1 shows the model statistics for all plots in Figure A.1. Figure A.2 shows age-related changes in beta burst characteristics for each phase of the button press response and for the resting state for the source analysis method. Table A.2 shows the model statistics for all plots in Figure A.2.

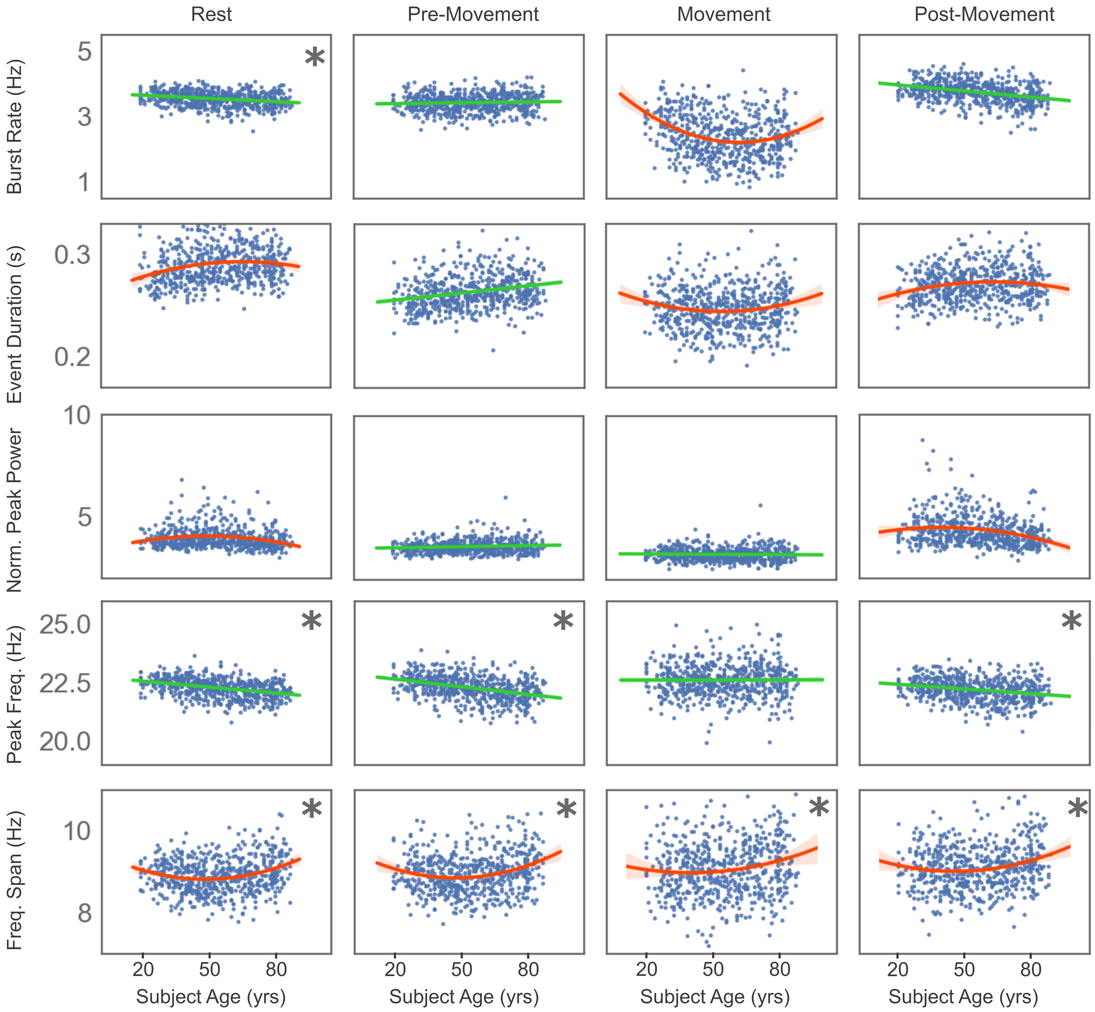

Figure A.1: Age-related changes in transient burst characteristics for all burst characteristics for each interval of the button press response and for the resting state. Only sensor ROI results are shown. Each plot is fit with the model, either linear (green) or quadratic (orange), that was deemed most appropriate via chi-square comparison. Stars indicate statistically relevant age-related trends. The shaded region around the line of best fit represents the 95% confidence interval.

Burst Rate

		Linear Fit	y(x) = a + bx			Quadratic Fit		y(x) = a + bx +cx^2			
Phase	F-stat	a [Hz]	b [10^{-3} Hz/y]	p-value	χ^2_{min}	a [Hz]	b [10^{-3} Hz/y]	c [10^{-5} Hz/y^2]	b p-value	c p-value	χ^2_{min}
Rest	0.68	**3.71**	**-3.16**	**1.20E-09**	**2.58**	3.84	-8.58	5.03	5.49E-01	6.97E-01	2.56
Pre-Move.	2.75	3.38	0.81	1.83E-01	4.15	3.52	-5.24	5.62	7.11E-01	6.67E-01	3.99
Move.	23.75	2.79	-7.30	8.85E-07	75.65	4.06	-60.33	49.26	5.00E-05	1.00E-04	56.07
Post Move.	4.08	4.07	-6.08	7.78E-18	4.02	3.86	2.88	-8.33	8.42E-01	5.22E-01	3.79

Event Duration

		Linear Fit	y(x) = a + bx			Quadratic Fit		y(x) = a + bx +cx^2			
Phase	F-stat	a [10^{-1} s]	b [10^{-5} s/y]	p-value	χ^2_{min}	a [10^{-1} s]	b [10^{-5} s/y]	c [10^{-7} s/y^2]	b p-value	c p-value	χ^2_{min}
Rest	6.81	2.81	15.98	1.99E-04	171.26	2.63	93.03	-71.57	9.44E-01	9.60E-01	155.68
Pre-Move.	-0.02	2.51	22.81	4.68E-10	402.78	2.42	60.15	-34.69	9.68E-01	9.76E-01	402.90
Move.	10.62	2.46	0.79	8.65E-01	942.29	2.67	-87.19	81.73	9.52E-01	9.52E-01	814.97
Post Move.	11.44	2.65	9.92	7.15E-03	204.24	2.50	74.66	-60.14	9.60E-01	9.60E-01	174.83

Normalized Peak Power

		Linear Fit	y(x) = a + bx			Quadratic Fit		y(x) = a + bx +cx^2			
Phase	F-stat	a	b [10^{-4} y^{-1}]	p-value	χ^2_{min}	a	b [10^{-2} y^{-1}]	c [10^{-5} y^{-2}]	b p-value	c p-value	χ^2_{min}
Rest	20.00	4.11	-29.36	9.35E-03	4.69	3.40	2.68	-27.61	2.00E-01	3.40E-02	3.62
Pre-Move.	2.09	3.52	17.11	1.71E-02	4.36	3.35	0.89	-6.63	5.35E-01	6.10E-01	4.23
Move.	-0.60	3.26	-5.09	4.75E-01	10.97	3.32	-0.31	2.43	8.26E-01	8.49E-01	11.07
Post Move.	9.90	4.80	-90.99	2.06E-08	6.53	4.07	2.17	-28.60	2.00E-01	2.85E-02	5.70

Peak Frequency

		Linear Fit	y(x) = a + bx			Quadratic Fit		y(x) = a + bx +cx^2			
Phase	F-stat	a [Hz]	b [10^{-3} Hz/y]	p-value	χ^2_{min}	a [Hz]	b [10^{-3} Hz/y]	c [10^{-5} Hz/y^2]	b p-value	c p-value	χ^2_{min}
Rest	1.87	**22.73**	**-8.33**	**1.38E-20**	**0.18**	22.91	-15.95	7.08	2.76E-01	5.89E-01	0.17
Pre-Move.	1.88	**22.86**	**-10.58**	**1.37E-21**	**0.26**	23.11	-21.27	9.93	2.00E-01	4.47E-01	0.25
Move.	-0.21	22.62	0.15	9.20E-01	0.57	22.58	1.64	-1.38	9.05E-01	9.12E-01	0.57
Post Move.	3.33	**22.55**	**-6.50**	**2.19E-09**	**0.35**	22.87	-19.98	12.52	2.00E-01	3.37E-01	0.34

Frequency Span

		Linear Fit	y(x) = a + bx			Quadratic Fit		y(x) = a + bx +cx^2			
Phase	F-stat	a [Hz]	b [10^{-4} Hz/y]	p-value	χ^2_{min}	a [Hz]	b [10^{-3} Hz/y]	c [10^{-5} Hz/y^2]	b p-value	c p-value	χ^2_{min}
Rest	42.02	8.75	29.48	1.88E-03	0.23	**9.42**	**-24.95**	**25.91**	**2.00E-01**	**2.00E-01**	**0.14**
Pre-Move.	33.59	8.75	37.50	4.59E-04	0.30	**9.46**	**-25.90**	**27.54**	**2.00E-01**	**3.49E-02**	**0.20**
Move.	4.48	8.78	53.52	8.38E-04	0.89	**9.24**	**-13.77**	**17.77**	**3.32E-01**	**2.76E-01**	**0.84**
Post Move.	10.69	8.88	41.76	4.94E-04	0.40	**9.42**	**-18.79**	**21.34**	**2.76E-01**	**2.00E-01**	**0.35**

Table A.1: Modeling parameters of sensor ROI calculated burst characteristics with age. Parameters are given for the linear and quadratic models. Bolded rows indicate statistical significance.

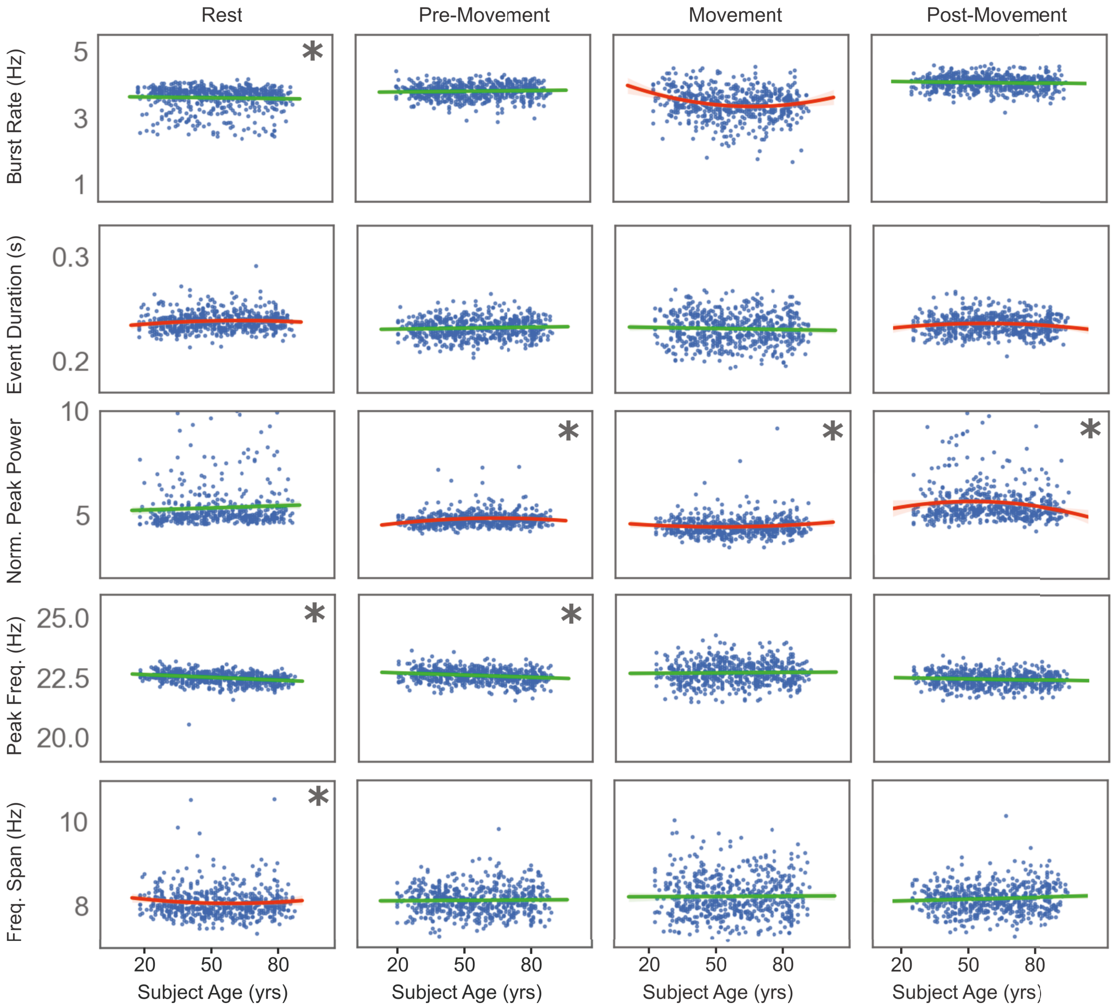

Figure A.2: Age-related changes in transient burst characteristics for all burst characteristics for each interval of the button press response and for the resting state. Only source-level results are shown. Each plot is fit with the model, either linear (green) or quadratic (orange), that was deemed most appropriate via chi-square comparison. Stars indicate statistically relevant age-related trends. The shaded region around the line of best fit represents the 95% confidence interval.

Burst Rate

Phase	F-stat	Linear Fit $y(x) = a + bx$				Quadratic Fit $y(x) = a + bx + cx^2$					
		a [Hz]	b [10^{-3} Hz/y]	p-value	χ^2_{min}	a [Hz]	b [10^{-3} Hz/y]	c [10^{-5} Hz/y^2]	b p-value	c p-value	χ^2_{min}
Rest	1.32	**3.85**	**-1.72**	**1.13E-04**	**0.74**	3.80	0.57	-2.14	9.76E-01	8.89E-01	0.73
Pre-Move.	-0.14	3.78	0.65	1.97E-01	1.96	3.85	-2.19	2.65	8.81E-01	8.42E-01	1.96
Move.	10.94	3.63	-3.57	4.58E-04	12.06	4.13	-24.68	19.66	2.00E-01	2.76E-01	10.39
Post Move.	2.15	4.11	-0.85	8.05E-02	1.57	3.94	6.20	-6.58	6.75E-01	6.31E-01	1.53

Event Duration

Phase	F-stat	Linear Fit $y(x) = a + bx$				Quadratic Fit $y(x) = a + bx + cx^2$					
		a [10^{-1} s]	b [10^{-5} s/y]	p-value	χ^2_{min}	a [10^{-1} s]	b [10^{-5} s/y]	c [10^{-7} s/y^2]	b p-value	c p-value	χ^2_{min}
Rest	6.30	2.34	5.26	9.14E-03	69.28	2.29	29.06	-22.18	9.84E-01	9.92E-01	63.41
Pre-Move.	0.63	2.31	2.94	1.72E-01	162.38	2.29	7.78	-4.51	9.92E-01	1.00E+00	160.89
Move.	0.80	2.33	-3.33	3.20E-01	274.86	2.35	-10.86	7.02	9.92E-01	9.92E-01	271.65
Post Move.	4.91	2.36	-1.74	4.11E-01	133.33	2.30	25.99	-25.85	9.84E-01	9.84E-01	124.36

Normalized Peak Power

Phase	F-stat	Linear Fit $y(x) = a + bx$				Quadratic Fit $y(x) = a + bx + cx^2$					
		a	b [10^{-4} y^{-1}]	p-value	χ^2_{min}	a	b [10^{-2} y^{-1}]	c [10^{-5} y^{-2}]	b p-value	c p-value	χ^2_{min}
Rest	1.25	5.19	33.26	1.80E-01	2.28	4.85	1.79	-13.59	2.94E-01	3.84E-01	2.24
Pre-Move.	4.31	4.70	22.04	5.57E-03	1.23	**4.39**	**1.52**	**-12.08**	**3.03E-01**	**3.74E-01**	**1.16**
Move.	7.01	4.43	10.87	2.86E-01	2.89	**4.65**	**-0.83**	**8.75**	**5.69E-01**	**5.16E-01**	**2.62**
Post Move.	7.93	5.82	-48.11	1.14E-02	1.96	**5.14**	**2.35**	**-26.43**	**2.00E-01**	**2.00E-01**	**1.76**

Peak Frequency

Phase	F-stat	Linear Fit $y(x) = a + bx$				Quadratic Fit $y(x) = a + bx + cx^2$					
		a [Hz]	b [10^{-3} Hz/y]	p-value	χ^2_{min}	a [Hz]	b [10^{-3} Hz/y]	c [10^{-5} Hz/y^2]	b p-value	c p-value	χ^2_{min}
Rest	-0.26	**22.78**	**-4.77**	**6.92E-16**	**0.04**	22.82	-6.52	1.63	7.04E-01	9.20E-01	0.04
Pre-Move.	0.22	**22.78**	**-3.04**	**4.65E-06**	**0.10**	22.72	-0.66	-2.22	9.68E-01	8.73E-01	0.10
Move.	2.97	22.70	0.57	5.95E-01	0.38	22.45	11.03	-9.74	4.53E-01	4.72E-01	0.37
Post Move.	3.20	22.53	-1.55	2.64E-02	0.10	22.71	-9.11	7.05	5.35E-01	6.03E-01	0.10

Frequency Span

Phase	F-stat	Linear Fit $y(x) = a + bx$				Quadratic Fit $y(x) = a + bx + cx^2$					
		a [Hz]	b [10^{-4} Hz/y]	p-value	χ^2_{min}	a [Hz]	b [10^{-3} Hz/y]	c [10^{-5} Hz/y^2]	b p-value	c p-value	χ^2_{min}
Rest	4.88	8.06	-5.37	4.80E-01	0.16	**8.22**	**-7.06**	**6.08**	**6.75E-01**	**6.97E-01**	**0.15**
Pre-Move.	1.54	8.12	2.98	6.89E-01	0.19	8.22	-3.84	3.85	7.95E-01	7.80E-01	0.18
Move.	0.48	8.22	2.18	8.45E-01	0.38	8.40	-7.29	7.00	6.17E-01	6.03E-01	0.38
Post Move.	3.28	8.11	13.58	6.98E-02	0.17	8.32	-7.52	8.27	6.10E-01	5.42E-01	0.17

Table A.2: Modeling parameters of source calculated burst characteristics with age. Parameters are given for the linear and quadratic models. Bolded rows indicate statistical significance.

Appendix B: Chapter 3 Supplementary Information

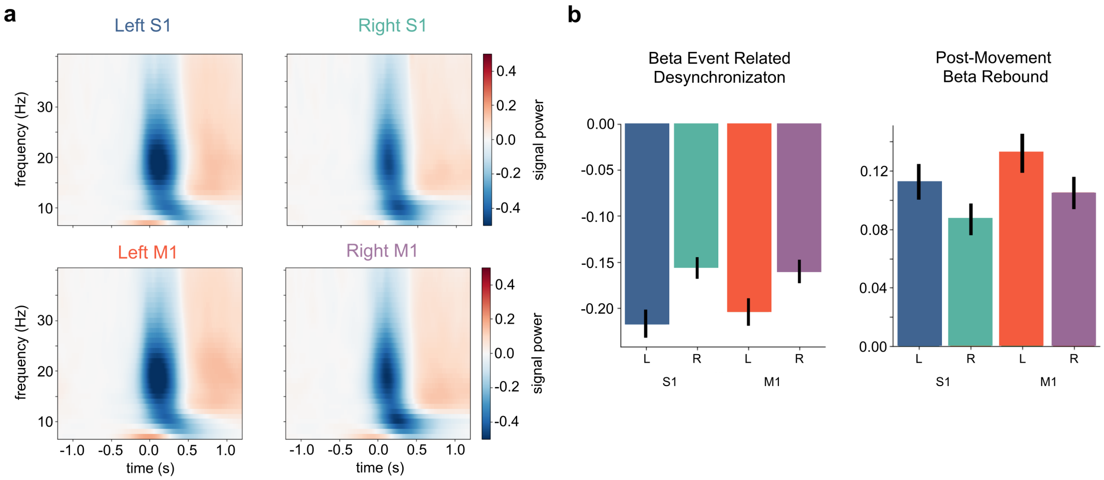

Figure B.1: Analyzing motor task data to validate resting state timecourses localized to four sensorimotor ROIs. (a) grand-average task-phase time frequency response plots centered on the button press at t = 0 s showing beta event related desynchronization (ERD) and post-movement beta rebound (PMBR) for each anatomical ROI. Signal power is shown as the log ratio relative to the baseline interval (-1.0 to -0.5 s). (b) bar plots showing average the value of the beta ERD and PMBR for each ROI. Error bars show 95% C.I. across participants. Both responses are left lateralized.

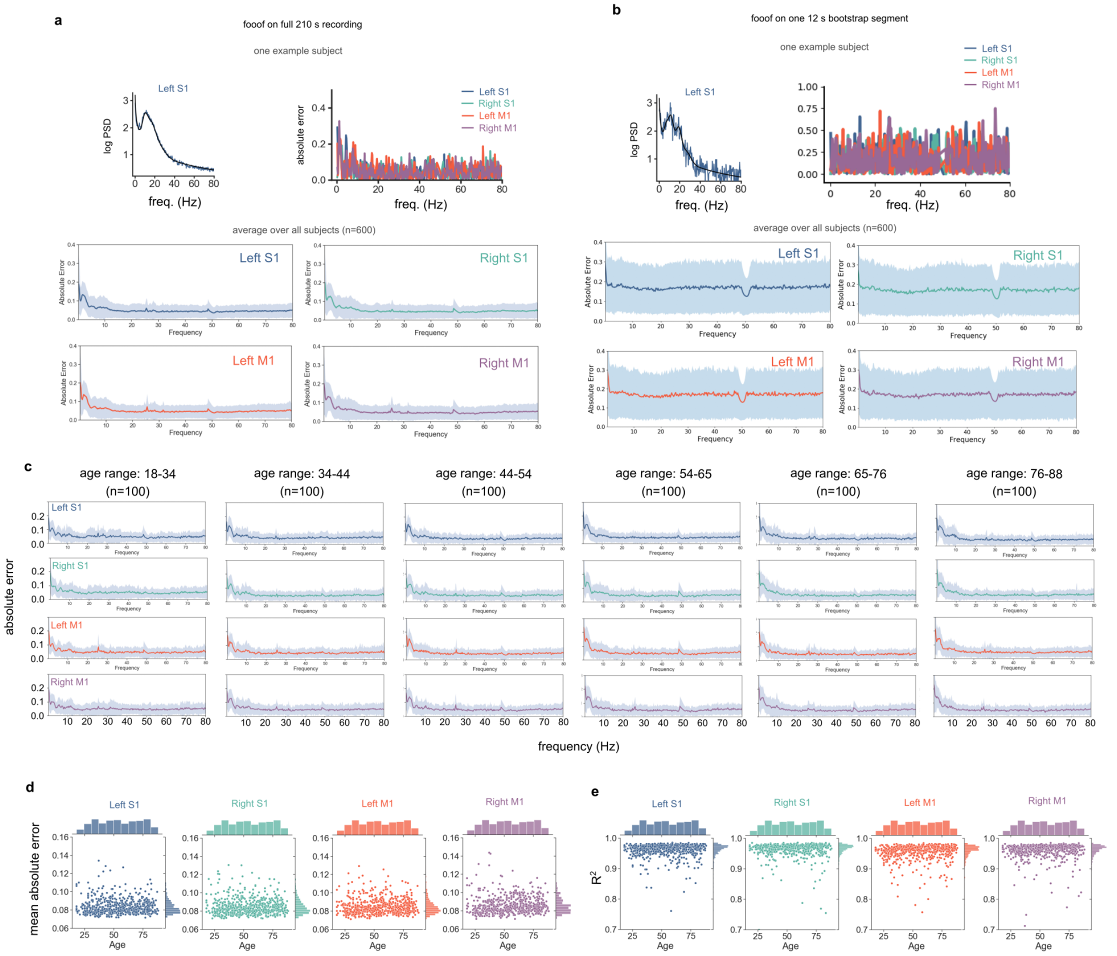

Figure B.2: Goodness of fit analysis for fooof modeling on Cam-CAN data. (a) An example PSD (generated from entire left S1 210 s resting-state timecourse) with fitted fooof model (top left) for one participant. The absolute error of the fooof model for each sensorimotor ROI (top right) for the same example participant. The average absolute error across all Cam-CAN participants (shaded areas represent 95% C.I.) for each sensorimotor ROI (bottom four panels). (b) same as a but PSD generated from one 12 s bootstrap segment instead of full 210 s resting state timecourse. (c) the absolute error of the fooof model (PSD generated from entire 210 s timecourse) average across subsets of the Cam-CAN cohort (each subset n = 100) according to participant age reveals no age-related effect. (d) mean absolute error for each Cam-CAN participant (PSD generated from full 210 s timecourse) assessed according to participant age. (e) R^2 for each Cam-CAN participant (PSD generated from full 210 s timecourse) assessed according to participant age.

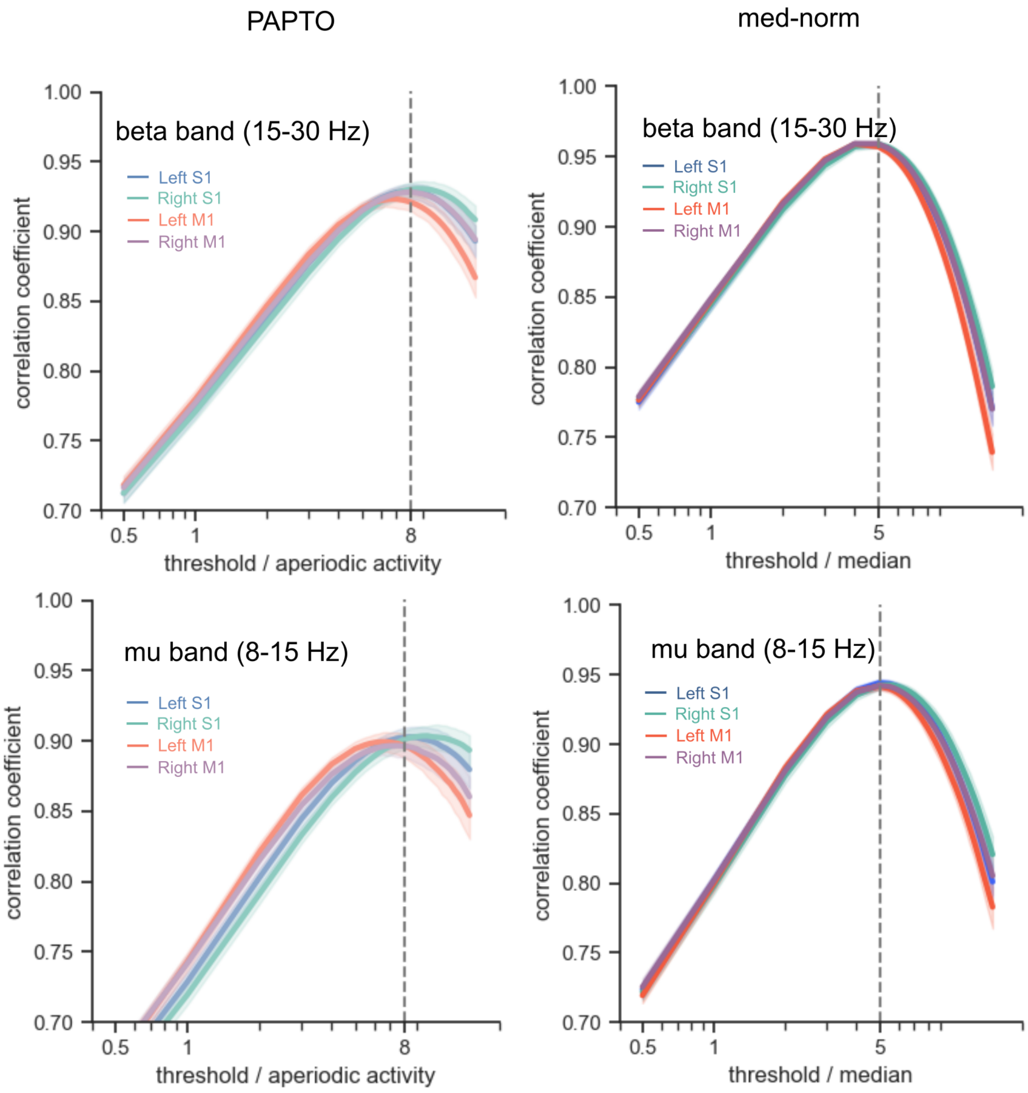

Figure B.3: Defining amplitude thresholds for med-norm and PAPTO transient events. Correlation coefficient between average resting state beta power and percent of spectrogram pixels with power above cutoff value, as a function of cutoff value. Each curve shown is the average across all Cam-CAN participants. Shaded areas represent 95% C.I. Peaks in correlation occur around $8X$ the aperiodic activity for PAPTO events in each anatomical ROI (beta and mu). Peaks in correlation occur around $5X$ the median power for med-norm events in each anatomical ROI (beta and mu).

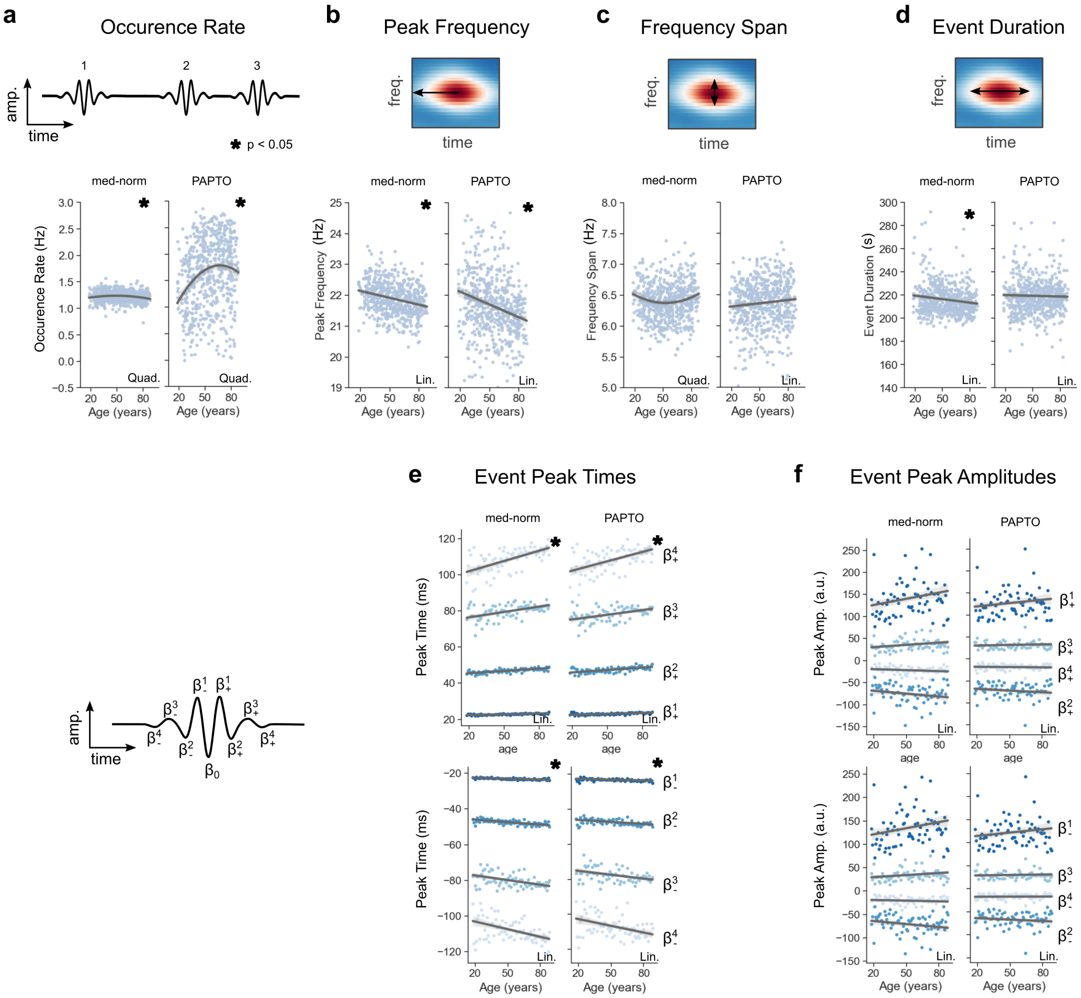

Figure B.4: Right hemisphere S1: Resting-state sensorimotor transient beta events show significant age-related changes. Each individual parameter of transient beta events evaluated for age-related changes. (a)-(f) scatterplots showing participant-average beta event parameters (occurrence rate, peak frequency, frequency span, event duration, event peak times, and event peak amplitudes, respectively) as a function of participant age (one point represents one participant) with linear or quadratic fitted ageing models. Stars indicate statistically significant ($p<0.05$, Bonferroni corrected for multiple comparisons) non-zero age related changes.

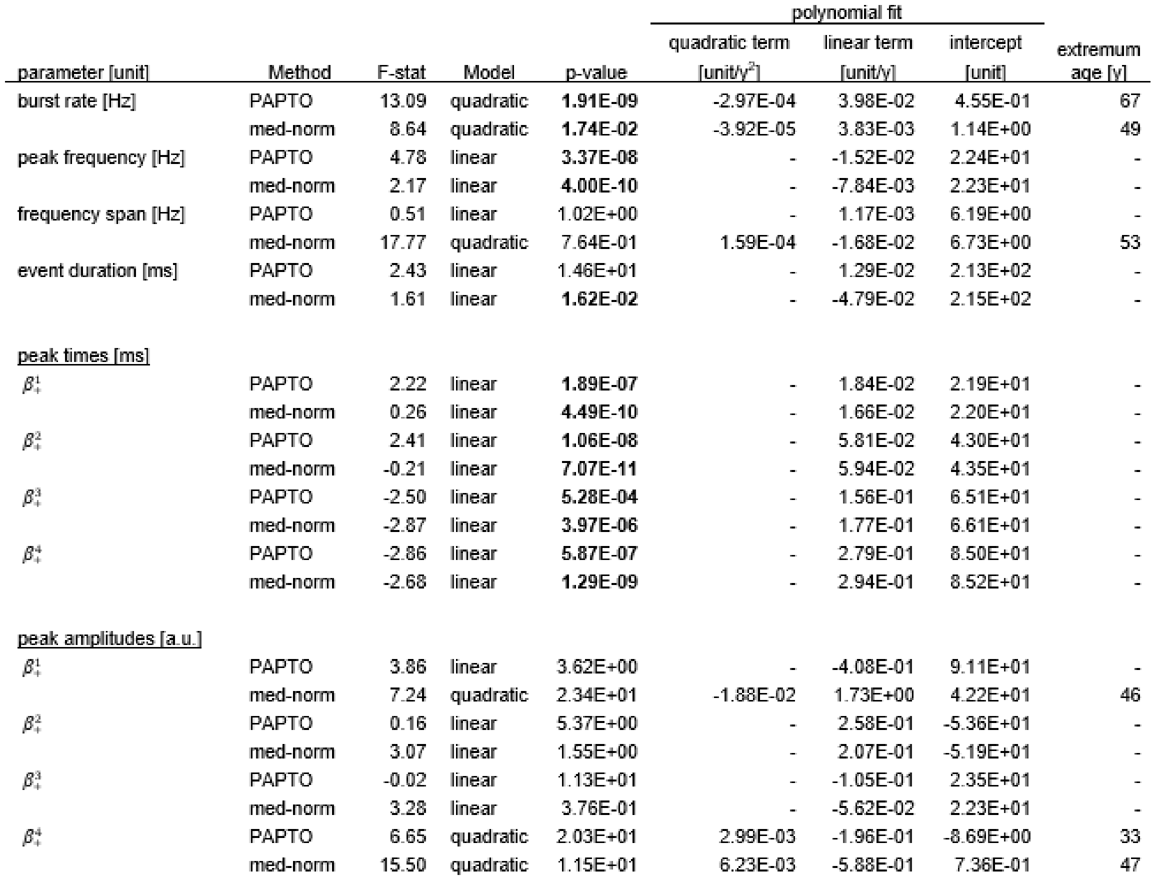

					polynomial fit			
parameter [unit]	Method	F-stat	Model	p-value	quadratic term [unit/y^2]	linear term [unit/y]	intercept [unit]	extremum age [y]
burst rate [Hz]	PAPTO	13.09	quadratic	**1.91E-09**	-2.97E-04	3.98E-02	4.55E-01	67
	med-norm	8.64	quadratic	**1.74E-02**	-3.92E-05	3.83E-03	1.14E+00	49
peak frequency [Hz]	PAPTO	4.78	linear	**3.37E-08**	-	-1.52E-02	2.24E+01	-
	med-norm	2.17	linear	**4.00E-10**	-	-7.84E-03	2.23E+01	-
frequency span [Hz]	PAPTO	0.51	linear	1.02E+00	-	1.17E-03	6.19E+00	-
	med-norm	17.77	quadratic	7.64E-01	1.59E-04	-1.68E-02	6.73E+00	53
event duration [ms]	PAPTO	2.43	linear	1.46E+01	-	1.29E-02	2.13E+02	-
	med-norm	1.61	linear	**1.62E-02**	-	-4.79E-02	2.15E+02	-
peak times [ms]								
β_+^1	PAPTO	2.22	linear	**1.89E-07**	-	1.84E-02	2.19E+01	-
	med-norm	0.26	linear	**4.49E-10**	-	1.66E-02	2.20E+01	-
β_+^2	PAPTO	2.41	linear	**1.06E-08**	-	5.81E-02	4.30E+01	-
	med-norm	-0.21	linear	**7.07E-11**	-	5.94E-02	4.35E+01	-
β_+^3	PAPTO	-2.50	linear	**5.28E-04**	-	1.56E-01	6.51E+01	-
	med-norm	-2.87	linear	**3.97E-06**	-	1.77E-01	6.61E+01	-
β_+^4	PAPTO	-2.86	linear	**5.87E-07**	-	2.79E-01	8.50E+01	-
	med-norm	-2.68	linear	**1.29E-09**	-	2.94E-01	8.52E+01	-
peak amplitudes [a.u.]								
β_+^1	PAPTO	3.86	linear	3.62E+00	-	-4.08E-01	9.11E+01	-
	med-norm	7.24	quadratic	2.34E+01	-1.88E-02	1.73E+00	4.22E+01	46
β_+^2	PAPTO	0.16	linear	5.37E+00	-	2.58E-01	-5.36E+01	-
	med-norm	3.07	linear	1.55E+00	-	2.07E-01	-5.19E+01	-
β_+^3	PAPTO	-0.02	linear	1.13E+01	-	-1.05E-01	2.35E+01	-
	med-norm	3.28	linear	3.76E-01	-	-5.62E-02	2.23E+01	-
β_+^4	PAPTO	6.65	quadratic	2.03E+01	2.99E-03	-1.96E-01	-8.69E+00	33
	med-norm	15.50	quadratic	1.15E+01	6.23E-03	-5.88E-01	7.36E-01	47

Table B.1: Right hemisphere S1: Modeling age-related changes of resting-state sensorimotor transient beta events. Ageing model fit parameters for each event characteristics. Model selection (linear vs quadratic) based on an F-test for each characteristic. Bolded rows indicate statistically significant ($p<0.05$, Bonferroni corrected for multiple comparisons) non-zero age related changes.

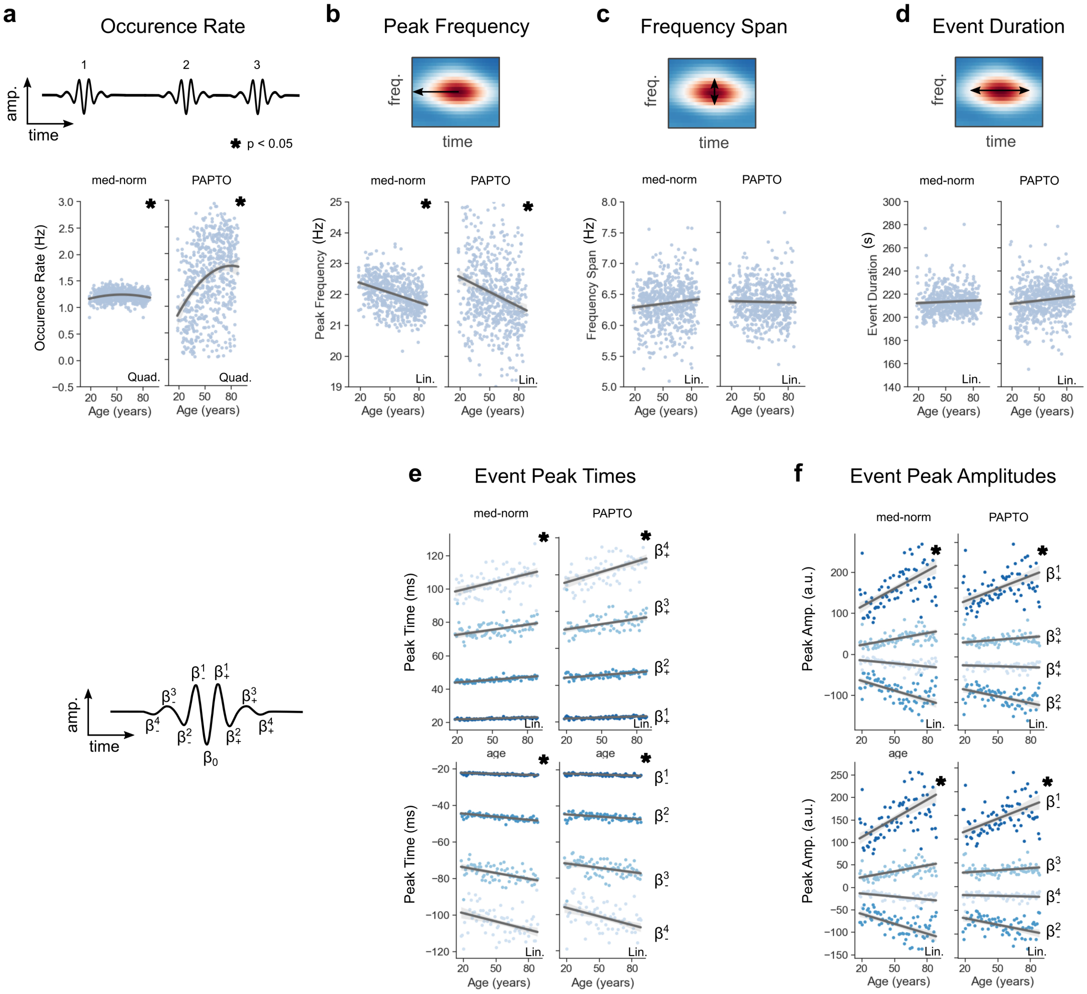

Figure B.5: Left hemisphere M1: Resting-state sensorimotor transient beta events show significant age-related changes. Each individual parameter of transient beta events evaluated for age-related changes. (a)-(f) scatterplots showing participant-average beta event parameters (occurrence rate, peak frequency, frequency span, event duration, event peak times, and event peak amplitudes, respectively) as a function of participant age (one point represents one participant) with linear or quadratic fitted ageing models. Stars indicate statistically significant ($p<0.05$, Bonferroni corrected for multiple comparisons) non-zero age related changes.

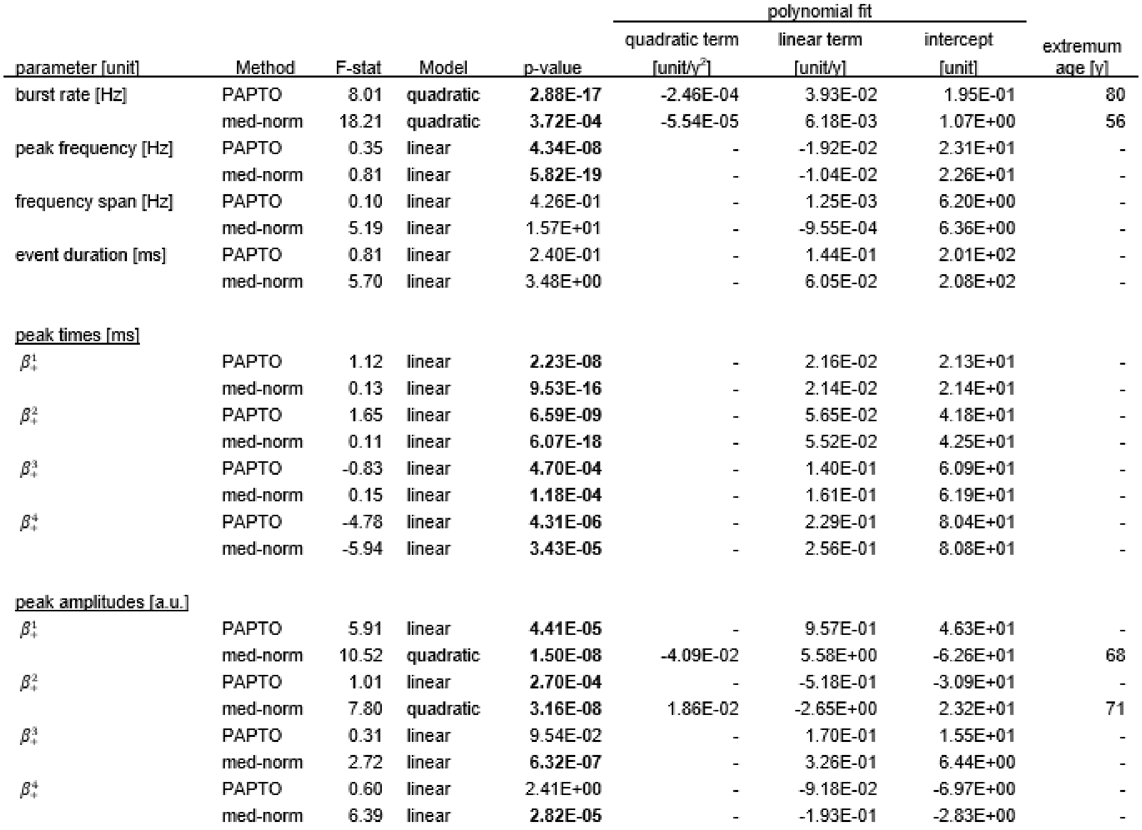

					polynomial fit			
parameter [unit]	Method	F-stat	Model	p-value	quadratic term [unit/y^2]	linear term [unit/y]	intercept [unit]	extremum age [y]
burst rate [Hz]	PAPTO	8.01	quadratic	**2.88E-17**	-2.46E-04	3.93E-02	1.95E-01	80
	med-norm	18.21	quadratic	**3.72E-04**	-5.54E-05	6.18E-03	1.07E+00	56
peak frequency [Hz]	PAPTO	0.35	linear	**4.34E-08**	-	-1.92E-02	2.31E+01	-
	med-norm	0.81	linear	**5.82E-19**	-	-1.04E-02	2.26E+01	-
frequency span [Hz]	PAPTO	0.10	linear	4.26E-01	-	1.25E-03	6.20E+00	-
	med-norm	5.19	linear	1.57E+01	-	-9.55E-04	6.36E+00	-
event duration [ms]	PAPTO	0.81	linear	2.40E-01	-	1.44E-01	2.01E+02	-
	med-norm	5.70	linear	3.48E+00	-	6.05E-02	2.08E+02	-
peak times [ms]								
β^1_+	PAPTO	1.12	linear	**2.23E-08**	-	2.16E-02	2.13E+01	-
	med-norm	0.13	linear	**9.53E-16**	-	2.14E-02	2.14E+01	-
β^2_+	PAPTO	1.65	linear	**6.59E-09**	-	5.65E-02	4.18E+01	-
	med-norm	0.11	linear	**6.07E-18**	-	5.52E-02	4.25E+01	-
β^3_+	PAPTO	-0.83	linear	**4.70E-04**	-	1.40E-01	6.09E+01	-
	med-norm	0.15	linear	**1.18E-04**	-	1.61E-01	6.19E+01	-
β^4_+	PAPTO	-4.78	linear	**4.31E-06**	-	2.29E-01	8.04E+01	-
	med-norm	-5.94	linear	**3.43E-05**	-	2.56E-01	8.08E+01	-
peak amplitudes [a.u.]								
β^1_+	PAPTO	5.91	linear	**4.41E-05**	-	9.57E-01	4.63E+01	-
	med-norm	10.52	quadratic	**1.50E-08**	-4.09E-02	5.58E+00	-6.26E+01	68
β^2_+	PAPTO	1.01	linear	**2.70E-04**	-	-5.18E-01	-3.09E+01	-
	med-norm	7.80	quadratic	**3.16E-08**	1.86E-02	-2.65E+00	2.32E+01	71
β^3_+	PAPTO	0.31	linear	9.54E-02	-	1.70E-01	1.55E+01	-
	med-norm	2.72	linear	**6.32E-07**	-	3.26E-01	6.44E+00	-
β^4_+	PAPTO	0.60	linear	2.41E+00	-	-9.18E-02	-6.97E+00	-
	med-norm	6.39	linear	**2.82E-05**	-	-1.93E-01	-2.83E+00	-

Figure B.6: Left hemisphere M1: Modeling age-related changes of resting-state sensorimotor transient beta events. Ageing model fit parameters for each event characteristics. Model selection (linear vs quadratic) based on an F-test for each characteristic. Bolded rows indicate statistically significant ($p<0.05$, Bonferroni corrected for multiple comparisons) non-zero age related changes.

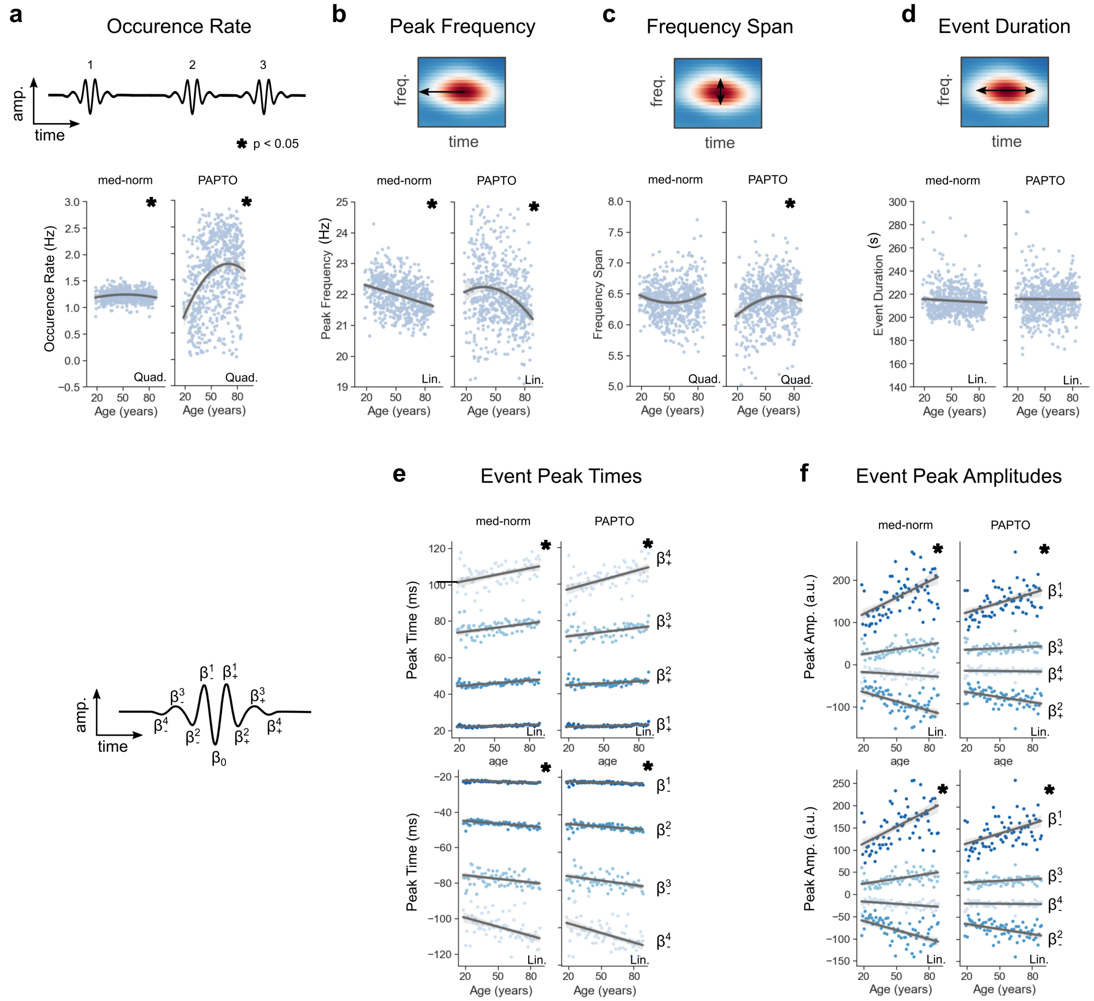

Figure B.7: Right hemisphere M1: Resting-state sensorimotor transient beta events show significant age-related changes. Each individual parameter of transient beta events evaluated for age-related changes. (a)-(f) scatterplots showing participant-average beta event parameters (occurrence rate, peak frequency, frequency span, event duration, event peak times, and event peak amplitudes, respectively) as a function of participant age (one point represents one participant) with linear or quadratic fitted ageing models. Stars indicate statistically significant ($p<0.05$, Bonferroni corrected for multiple comparisons) non-zero age related changes.

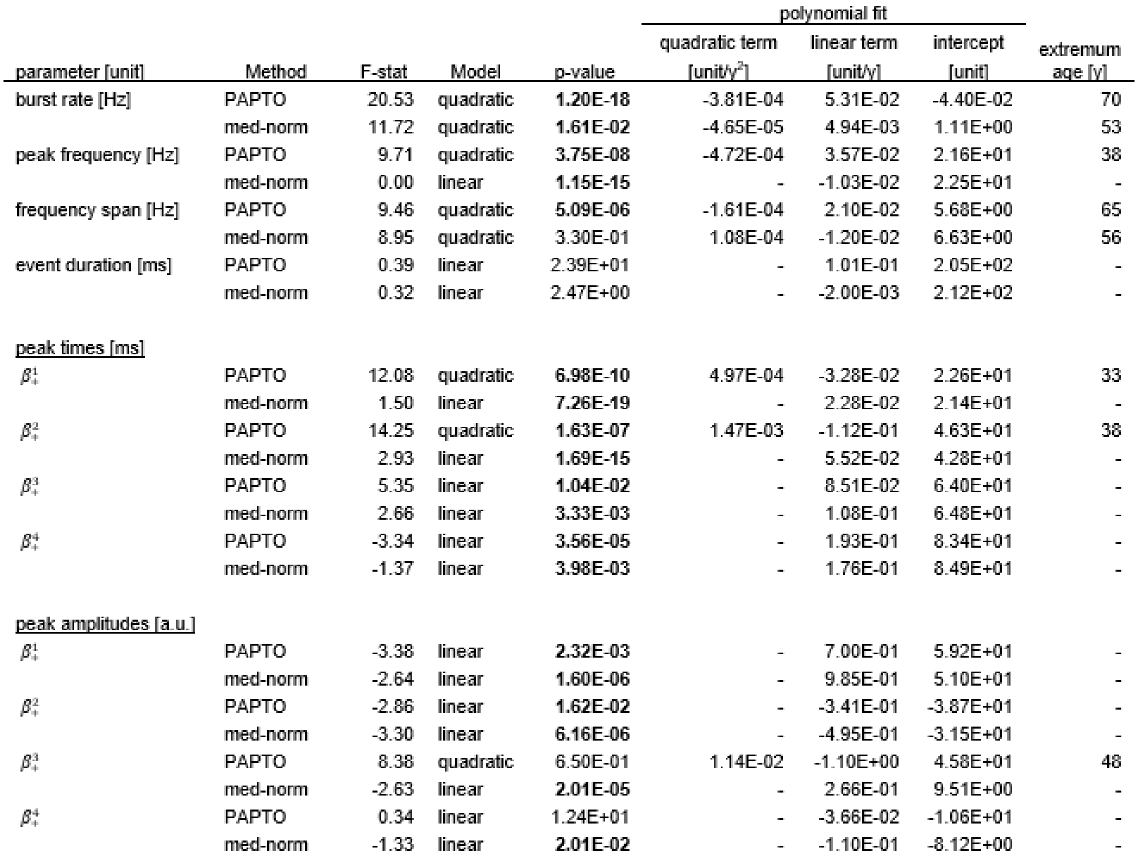

					polynomial fit			
parameter [unit]	Method	F-stat	Model	p-value	quadratic term [unit/y^2]	linear term [unit/y]	intercept [unit]	extremum age [y]
burst rate [Hz]	PAPTO	20.53	quadratic	**1.20E-18**	-3.81E-04	5.31E-02	-4.40E-02	70
	med-norm	11.72	quadratic	**1.61E-02**	-4.65E-05	4.94E-03	1.11E+00	53
peak frequency [Hz]	PAPTO	9.71	quadratic	**3.75E-08**	-4.72E-04	3.57E-02	2.16E+01	38
	med-norm	0.00	linear	**1.15E-15**	-	-1.03E-02	2.25E+01	-
frequency span [Hz]	PAPTO	9.46	quadratic	**5.09E-06**	-1.61E-04	2.10E-02	5.68E+00	65
	med-norm	8.95	quadratic	3.30E-01	1.08E-04	-1.20E-02	6.63E+00	56
event duration [ms]	PAPTO	0.39	linear	2.39E+01	-	1.01E-01	2.05E+02	-
	med-norm	0.32	linear	2.47E+00	-	-2.00E-03	2.12E+02	-
peak times [ms]								
β_+^1	PAPTO	12.08	quadratic	**6.98E-10**	4.97E-04	-3.28E-02	2.26E+01	33
	med-norm	1.50	linear	**7.26E-19**	-	2.28E-02	2.14E+01	-
β_+^2	PAPTO	14.25	quadratic	**1.63E-07**	1.47E-03	-1.12E-01	4.63E+01	38
	med-norm	2.93	linear	**1.69E-15**	-	5.52E-02	4.28E+01	-
β_+^3	PAPTO	5.35	linear	**1.04E-02**	-	8.51E-02	6.40E+01	-
	med-norm	2.66	linear	**3.33E-03**	-	1.08E-01	6.48E+01	-
β_+^4	PAPTO	-3.34	linear	**3.56E-05**	-	1.93E-01	8.34E+01	-
	med-norm	-1.37	linear	**3.98E-03**	-	1.76E-01	8.49E+01	-
peak amplitudes [a.u.]								
β_+^1	PAPTO	-3.38	linear	**2.32E-03**	-	7.00E-01	5.92E+01	-
	med-norm	-2.64	linear	**1.60E-06**	-	9.85E-01	5.10E+01	-
β_+^2	PAPTO	-2.86	linear	**1.62E-02**	-	-3.41E-01	-3.87E+01	-
	med-norm	-3.30	linear	**6.16E-06**	-	-4.95E-01	-3.15E+01	-
β_+^3	PAPTO	8.38	quadratic	6.50E-01	1.14E-02	-1.10E+00	4.58E+01	48
	med-norm	-2.63	linear	**2.01E-05**	-	2.66E-01	9.51E+00	-
β_+^4	PAPTO	0.34	linear	1.24E+01	-	-3.66E-02	-1.06E+01	-
	med-norm	-1.33	linear	**2.01E-02**	-	-1.10E-01	-8.12E+00	-

Figure B.8: Right hemisphere M1: Modeling age-related changes of resting-state sensorimotor transient beta events. Ageing model fit parameters for each event characteristics. Model selection (linear vs quadratic) based on an F-test for each characteristic. Bolded rows indicate statistically significant ($p<0.05$, Bonferroni corrected for multiple comparisons) non-zero age related changes.

Appendix C: Copyright Permissions

Chapters 2 and 3 of this thesis were each published through *Elsevier* in the journal *NeuroImage*. As the author of these articles, I have the right to include them in my thesis. Letters of permissions are not required. For more information, see
https://www.elsevier.com/about/policies/copyright#Author-rights